# Thermal and Mechanical Design of a High-Speed Power Dense Radial Flux Surface Mounted PM Motor

# THERMAL AND MECHANICAL DESIGN OF A HIGH-SPEED POWER DENSE RADIAL FLUX SURFACE MOUNTED PM MOTOR

BY

KENNETH NORONHA, B.Eng.

A THESIS

SUBMITTED TO THE DEPARTMENT OF MECHANICAL ENGINEERING

AND THE SCHOOL OF GRADUATE STUDIES

OF MCMASTER UNIVERSITY

IN PARTIAL FULFILLMENT OF THE REQUIREMENTS

FOR THE DEGREE OF

MASTER OF APPLIED SCIENCE

Master of Applied Science (2024) McMaster University
(Mechanical Engineering) Hamilton, Ontario, Canada

| | |
|---|---|
| TITLE: | Thermal and Mechanical Design of a High-Speed Power Dense Radial Flux Surface Mounted PM Motor |
| AUTHOR: | Kenneth Noronha<br>B.Eng., Mechanical Engineering<br>McMaster University, Hamilton, Canada |
| SUPERVISOR: | Dr. Ali Emadi |
| NUMBER OF PAGES: | xxvi, 171 |

# Abstract

With the growing need to meet aggressive emissions targets in the aerospace industry in the coming decades, the electrification of propulsion systems has become an area of great research and commercial interest. In order to achieve full electrification of larger commercial aircraft, it is critical to improve power and energy densities of components within the propulsion system. The power densities of electric motors are steadily rising to meet this requirement. Among the various motor designs available, the high-speed radial flux permanent magnet motor is presented as an architecture capable of achieving high efficiencies and power densities. Increasing power densities, however, poses challenges for the thermal management system as higher losses need to be dissipated from a relatively small machine package. One of the failure modes specific to permanent magnet motors is the demagnetization of the magnets in the rotor at higher temperatures which leads to a loss in performance. Therefore it is critical that the thermal management system of the rotor must effectively dissipate the losses generated in the magnets and other components within the rotor.

This thesis discusses the mechanical and thermal design of a 150 kW high-speed radial flux surface mounted permanent magnet motor for aerospace propulsion applications. The thesis first introduces the current landscape of aerospace electrification, focusing specifically on electric and hybrid propulsion architectures, currently available electric motors for aerospace propulsion, and ongoing aircraft electrification projects. A review is then provided of the current state-of-the-art in rotor cooling designs for high-speed speed radial flux motors for traction applications before introducing the design of the motor proposed in this thesis. The discussion of the mechanical design provides a high level overview of the design, manufacturing, and assembly of the stator and rotating assemblies while the thermal design provides a brief overview of the stator cooling design and a deep dive on the rotor cooling design. Computational Fluid Dynamics (CFD) is used along with the Taguchi method for robust design to optimize the rotor cooling design for minimizing the magnet temperatures. Analysis for the optimized rotor cooling discussed is provided before providing recommendations for future work.

# Acknowledgements

I would first like to thank my supervisor Dr. Ali Emadi for the opportunities and support throughout my years at McMaster. You provided me with the opportunities to learn and grow, including my involvement in the EcoCar3 team, research projects during my undergraduate studies, and of course my master's research. I will forever be grateful for your support and guidance that has led me to gain industry-relevant skills, knowledge, and experience.

I would also like to thank my colleagues on the Eaton projects. Thank you Dr. Giorgio Pietrini, Dr. Mohamed Abdelmagid, Dr. Alan Callegaro, and Dr. John Reimers for your exceptional leadership and contribution throughout my time at the McMaster Automotive Resource Centre. Thank you to all of my fellow team members on worked on the motor projects. It has been truly remarkable to witness the progress we have made over the years and the knowledge I have gained from working along side you all.

Thank you to the Eaton Corporation and Mitacs for funding this research and to the individuals at Eaton Aerospace and Eaton Research Labs for you technical support.

It has been a pleasure to collaborate with you over the multiple motor projects I have been a part of.

Thank you to Federico "Walter Berry" Duperly for mentoring me throughout my years at McMaster since my first year in my undergraduate studies on the EcoCar3 team even up to now. You have helped me learn much throughout the years, both in engineering-related topics and elsewhere. I am also grateful for the help and support throughout my thesis, taking time out of your days to help keep me on track with completing this work.

Lastly, I would like to thank my friends and family for their unwavering support throughout my thesis. Your constant encouragement has been a source of motivation for me throughout my masters, I could not have done this without you. Thank you mom for being my biggest supporter and to Kevin and Victoria for your support and encouragement over the years. I would like to honour the memory of my late father who served as a role model for me in my formative years and through my undergraduate studies. His encouragement led me to pursue my master's degree, and I regret that he could be here to see me complete it.

# Nomenclature

## Abbreviations

| | |
|---|---|
| **AEA** | All Electric Aircraft |
| **AF** | Axial Flux |
| **AM** | Additive Manufacturing |
| **ATF** | Automatic Transmission Fluid |
| **CFD** | Computational Fluid Dynamics |
| **CHT** | Conjugate Heat Transfer |
| **CTE** | Coefficient of Thermal Expansion |
| **DES** | Detached Eddy Simulation |
| **DFA** | Design for Assembly |

| | |
|---|---|
| **DFM** | Design for Manufacturing |
| **DGBB** | Deep Groove Ball Bearing |
| **DNS** | Direct Numerical Simulation |
| **DOE** | Design of Experiments |
| **EPU** | Electric Propulsion Unit |
| **FEA** | Finite Element Analysis |
| **GA** | General Aviation |
| **HIP** | Hot Isostatic Pressing |
| **HTC** | Heat Transfer Coefficient |
| **ICAO** | International Civil Aviation Organization |
| **ID** | Inner Diameter |
| **LES** | Large Eddy Simulation |
| **LMC** | Minimal Material Condition |
| **LOT** | Minimum Operating Temperature |
| **L-PBF** | Laser Powder Bed Fusion |
| **MEA** | More Electric Aircraft |

**MMC** Maximum Material Condition

**MOT** Maximum Operating Temperature

**MRF** Multiple Reference Frame

**OD** Outer Diameter

**PEEK** Polyether Ether Ketone

**PMSM** Permanent Magnet Synchronous Motor

**RANS** Reynolds Averaged Navier Stokes

**RF** Radial Flux

**RSM** Reynolds Stress Model

**S/N** Signal to Noise

**SAF** Safe Aviation Fuel

**SRM** Switched Reluctance Motor

**UAV** Unmanned Aerial Vehicle

**WEG** Water Ethylene Glycol

# Symbols

$P_{DC}$ Winding DC resistance loss

| | |
|---|---|
| $R$ | DC electrical resistance |
| $i$ | Current |
| $V$ | Voltage |
| $\rho_{cop}$ | Copper electrical resistivity |
| $l_{cop}$ | Copper wire length |
| $A_{wire}$ | Winding conductor cross sectional area |
| $P_w$ | Windage loss |
| $C_f$ | Skin friction coefficient |
| $\rho$ | Density |
| $r_1$ | Rotor outer diameter |
| $l_{gap}$ | Airgap length |
| $\mu$ | Dynamic viscosity |
| $M$ | Bearing total friction loss |
| $M_1$ | Bearing friction loss due to applied load |
| $M_2$ | Bearing friction loss due to viscous effects |
| $d_m$ | Bearing mean diameter |

| | |
|---|---|
| $F_s$ | Static equivalent bearing load |
| $C_s$ | Basic static load rating |
| $F_a$ | Axial load |
| $F_r$ | Radial load |
| $\nu_{lub}$ | Bearing oil kinematic viscosity |
| $G$ | Bearing total heat generation |
| $n_g$ | Bearing loss correction factor |
| $Re_{gap}$ | Airgap Reynolds number |
| $Re_a$ | Axial Reynolds number |
| $Re_r$ | Radial Reynolds number |
| $Pr$ | Prandtl number |
| $Nu$ | Nusselt number |
| $D_h$ | Hydraulic diameter |
| $\lambda$ | Thermal conductivity |
| $c_P$ | Specific heat capacity |
| $V_a$ | Axial velocity |

| | |
|---|---|
| $V_r$ | Radial velocity |
| $h$ | Heat transfer coefficient |
| $DN$ | Speed factor |
| $D$ | Bearing outer diameter |
| $d$ | Bearing inner diameter |
| $\omega$ | Rotation speed (rad/s) |
| $n$ | Rotation speed (RPM) |
| $\omega_{cr}$ | Critical speed (rad/s) |
| $n_{cr}$ | Critical speed (RPM) |
| $E_i$ | Inner cylinder Young's modulus |
| $E_o$ | Outer cylinder Young's modulus |
| $\nu_i$ | Inner cylinder Poisson's ratio |
| $\nu_o$ | Outer cylinder Poisson's ratio |
| $\alpha_i$ | Inner cylinder coefficient of thermal expansion |
| $\alpha_o$ | Outer cylinder coefficient of thermal expansion |
| $T_{app}$ | Applied torque |

| | |
|---|---|
| $T_{min}$ | Minimum operating temperature |
| $T_{max}$ | Maximum operating temperature |
| $\mu_f$ | Coefficient of friction |
| $L_{int}$ | Interface length |
| $R_{int}$ | Interface Radius |
| $R_{int,i/o}$ | Unpressed interface radii of the inner/outer cylinders |
| $r_i$ | Inner cylinder inner diameter |
| $r_o$ | Outer cylinder outer diameter |
| $p_{int}$ | Interface pressure |
| $\delta_{int}$ | Radial interference |
| $\sigma_{t,i}$ | Inner cylinder tangential stress |
| $\sigma_{t,o}$ | Outer cylinder tangential stress |
| $\sigma_o$ | Effective (Von Mises) stress of the outer cylinder |
| $U$ | Velocity flow field |
| $p$ | Pressure field |
| $\tau$ | Shear stress |

| | |
|---|---|
| $S_M$ | Momentum source term |
| $S_E$ | Energy source term |
| $S_{M,rot}$ | Momentum source term from rotational motion |
| $S_{Cor}$ | Momentum aource term from the Coriolis force |
| $S_{cfg}$ | Momentum source term from centrifugal forces |
| $S_{M,\omega}$ | Momentum source term from angular acceleration |
| $I$ | Rothalpy |
| $k$ | Turbulent kinetic energy |

# Contents

# List of Tables

# List of Figures

# Chapter 1

# Introduction

## 1.1 Background and Motivations

The transportation sector has recently seen a significant shift towards electrification to counteract pollution from fossil fuel dominated technologies. The aviation sector is among the largest polluters today, accounting for 11.6% of total emissions [1] and is expected to increase to 20% of emissions by 2050 [2]. The International Civil Aviation Organization (ICAO) predicts that air traffic will double by 2035 [3]. Large aircraft account for approximately 75% of total emissions output by the aviation sector, which is further increased if military, space, and scientific related aviation activities are included [4]. The goal in the coming decades is to reduce $NO_X$, $CO$ and $CO_2$ emissions with governing bodies such as the International Air Transport Association committing to reduce emissions by 50%, and the European Commission setting an aggressive target to cut $CO_2$ and $NO_X$ emissions by 50% and 90% respectively by 2050 [2].

Current initiatives to help reduce emissions in the aviation industry include exploring cleaner alternative fuels, lighter structural materials, and electrification of major systems [1]. Sustainable Aviation Fuels (SAFs) have been recently proposed as an alternative fuel derived from biomass such as plants, animals, and other natural wastes. The first flight using a blend of jet fuel and SAFs took place in 2008. Since then, 150,000 flights have used SAFs. The largest barrier to its widespread adoption is the additional costs over conventional jet fuel, which is problematic given that that fuel costs are the single largest overhead for airlines. Over time, increasing investments in SAF technologies will help reduce costs and improve its feasibility for widespread use [5].

Lightweight structural materials are continually being developed and improved, especially in the aerospace industry where higher costs of new, high performance technologies are an acceptable tradeoff. An example of recent innovations in lightweight aircraft materials is the extensive use of composites in the wings and fuselage of newer aircraft, most notably in the Boeing 787 and Airbus A350, and in the fan blades of next generation turbofan engines, such as GE's GE90 and GENx engines [6]. Additive manufacturing has also taken off in the past decade as a viable technology for production in the aerospace industry, favouring higher performance and lower weight due to more design freedom. This allows for reduced part count and more complex geometries that cannot be machined through conventional processes. A large variety of metals can now be additively manufactured, including aluminum alloys, case hardening steels, pure copper, nickel alloys, titanium, and more [7], which further the expands the range of components that can be made for aerospace via additive manufacturing.

More Electric Aircraft (MEA) is a recent initiative introduced in the past 20 years which has driven aircraft manufacturers to replace conventionally powered systems for auxiliary components, such as cabin pressurization, hydraulic pump actuation, etc. with electric motor alternatives to help reduce aircraft emissions. Most recently, this has been implemented in the Boeing 787 and Airbus A350 [8]. However, the shift to MEA, along with the other initiatives and technological advantages, are not nearly sufficient to meet the aggressive emissions targets set by the aforementioned governing bodies. Therefore, more substantial electrification solutions need to be explored to reduce overall emissions.

The next step is to electrify the propulsion systems of aircraft. Aircraft propulsion electrification is a very recent undertaking. From 2006 to 2009, only one paper concerning electric and hybrid aircraft appeared per year, with the amount of research only increasing since then [9]. The research is still in its infancy as most electrification projects have not moved past the experimentation phase.

The main goal with aircraft electrification is to move towards hybridization and eventually full electrification of the propulsion systems. To achieve this goal, propulsion units and energy storage systems must target higher power and energy densities, respectively.

High-speed Permanent Magnet Synchronous Motors (PMSMs) are notable for their ability to achieve high efficiencies and power densities. The main disadvantage of high-speed machines for aircraft propulsion is the requirement of a gearbox to reduce the output speed to drive a fan or propeller at their optimal operating speeds. This reduces the efficiency of the system due to transmission losses from the gearbox.

Increasing the power density inherently increases the load on the thermal management system of a motor. In most cases, the thermal management system is the limiting factor for motor performance. In an inner rotor radial flux motor, active cooling of the stator can be implemented relatively easily as a primary means to cool the machine. In some applications, this can be supplemented by passive heat dissipation through forced or natural convection on the outer surface of the motor housing. Examples of active stator cooling techniques include flood cooling, spray cooling, and cooling through channels with the stator slots and backiron. Rotor cooling can be more challenging in high-speed machines due to additional losses generated by the interaction between the cooling fluid (air or liquid) and the rotor. Depending on the rotor cooling design, mechanical complexity and losses from seals or other mechanical components may also be disadvantages. In Permanent Magnet (PM) motors, the PMs are the main loss generating components in the rotor. There is a risk of demagnetization at high temperatures as a result of the rotor losses.

This thesis explores the current landscape for aerospace electrification, specific challenges related to power dense radial flux machines, and the mechanical and thermal design of a power dense high-speed radial flux surface mounted PM motor proposed for this thesis. The main focus of the thermal design of the proposed motor is on the rotating assembly whereas the mechanical design discussion provides a high level overview on the cooling design for the stator assembly, and the manufacturing, tooling, and assembly of the stator and rotating assemblies. The proposed machine is an initial design meant to undergo further analysis, specifically mechanical and electromagnetic analysis, to further improve the power density and ensure that the components within the motor can ensure the high stresses from vibrations and centrifugal loading.

## 1.2 Research Contributions

The aim of this research is to design a power dense high-speed power dense radial flux surface mounted PM motor for aerospace applications. The motor proposed in this thesis has a maximum continuous power of 150 kW and a maximum speed of 20 kRPM. To safely operate at this peak operating condition for a power dense PM machine, the weight of the components within the motor should be minimized in the stator and rotating assemblies, while providing adequate cooling for the stator and rotor. The thesis attempts to tackle the following objectives:

- Present the current landscape of electric motors for aerospace propulsion applications along with current and near-future aircraft electrification projects. The motors and projects presented provide useful context and points of comparison between the current state-of-the-art for aerospace propulsion and the motor proposed within this thesis. Hybrid electric propulsion architectures are also discussed to show the first steps that aircraft electrification propulsion must take before achieving fully electric propulsion.

- Discuss the design, manufacturing, and assembly of the stator and rotating assemblies of the proposed motor to provide a high level overview of the mechanical design without delving into structural analysis. Initial designs proposed in this thesis are Design For Manufacturing (DFM) and Design For Assembly (DFA) studies from a mechanical perspective that require further structural analysis to finalize the designs. Contributions from fellow researchers on components within the proposed motor are further covered in Chapter 4.

- Provide an in-depth study on the rotor cooling design optimization using Computational Fluid Dynamics (CFD) to minimize magnet temperatures within the proposed motor. The optimization of the rotor cooling design provides a view of the capabilities of the rotor cooling system to dissipate higher losses in future revisions of the design that increase the power output.

## 1.3 Thesis Outline

**Chapter 1: Introduction**

A brief discussion on the motivation for power dense electric motors for aerospace propulsion applications.

**Chapter 2: Electric Machines for Aerospace Propulsion Applications**

A survey on electric motors currently available for aerospace propulsion applications along with current promising electrified aircraft projects. Challenges in aircraft electrification are discussed and hybrid electric propulsion architectures are presented as alternatives to fully electric propulsion systems that may be more feasible in the near future for larger commercial aircraft.

**Chapter 3: Rotor Design in High-Speed Radial Flux PM Machines**

An exploration into the thermal and mechanical design of high-speed rotors in electric motors for traction applications in the literature. This section aims to provide insight into the current state-of-the-art in high-speed rotor cooling along with benefits and challenges faced by these designs.

**Chapter 4: Proposed High-Speed Power Dense Radial Flux Surface-Mounted PM Motor Design**

An introduction to the motor proposed for this thesis. A view of the stator assembly's design and manufacturing process is provided from the design and manufacturing of the structural components to the potting of the stator windings with the associated tooling. The rotor mechanical design is presented with an overview of the bearing selection, bearing lubrication and cooling, rotor cooling loop with provisions for integration with the stator cooling, and rotor hub and shaft design. Justifications are provided for the overarching layout and design choices for the rotor and stator assemblies.

**Chapter 5: Rotor Thermal Modeling, Analysis, and Optimization**

A deep dive into the thermal analysis and optimization of the rotor cooling design using the Taguchi method to minimize the maximum magnet temperatures. The rotor losses, simplified geometry, simulation setup, and meshing are discussed before using the Taguchi method for robust design to optimize the rotor cooling design. Analysis for the optimized design is discussed.

**Chapter 6: Conclusion**

A summary of the of the work done, outcomes of this research, and future work to further improve the designs presented in this thesis.

# Chapter 2

# Electric Machines for Aerospace Propulsion Applications

This chapter begins with a discussion on the challenges in aviation electrification, emphasizing the two biggest concerns related to larger commercial aircraft: electric motor power densities and energy densities of current energy storage technologies. These challenges lead to an overview of aircraft hybridization, which is a useful stepping stone from current turbine and internal combustion engine propulsion to fully electric aircraft. This section describes a number of hybrid architectures along with benefits and drawbacks of each type of architecture. The chapter concludes with a look at electric motors for aerospace propulsion applications along with current aircraft electrification projects. Since this thesis focuses on the design of a high-speed power dense electric motor, the motor specifications covered in this chapter offer points of comparison between the state-of-the-art and the motor proposed for this thesis. As aircraft electrification is a relatively new field in the aerospace industry, the number of motors and aircraft intended for commercial applications is slim, however the field has seen considerable progress in power densities and number of aviation electrification projects in recent years, most of which are still very early within their design phases. Note that the final section only cover projects that have moved past the very early design phase and provide some targeted or tested performance figures.

## 2.1 Challenges for Electrification

All Electric Aircraft (AEA) architectures have been proposed as a solution to achieve future emissions targets. However, AEA technology is still in its infancy and cannot be scaled to large passenger and cargo aircraft due to the high power density, and by extension, low weight requirements for fully electric propulsion systems in such aircraft. Fully electrified propulsion systems are feasible for Unmanned Aerial Vehicles (UAVs) and small General Aviation (GA) aircraft because they are lightweight and have much shorter flight ranges whereas the power and energy storage requirements are far larger for narrowbody and widebody passenger aircraft [1]. As electrification technologies improve and power densities increase, single aisle aircraft with fully electrified propulsion may be realized. The ATR-72 is an example of a single aisle regional aircraft that uses two PW127D turboprop engines each producing 2.1 MW of power achieving a power density of 4.26 kW/kg [10]. However, the power output and power density requirements for commercial aircraft like the Airbus A350 are far higher. Two Trent XWB-97 Turbofan engines are capable of outputting 93.7 MW each and have a power density of 12.41 kW/kg [11], figures that are far more difficult to achieve without significant advancements in electrification technologies.

There are two approaches to electric motors for aircraft electric propulsion: high-speed, and high-torque density machines. High-speed machines can offer higher power densities compared to lower speed machines as the motor speed is directly coupled with the power density [1].

High speed machines require a gearbox to achieve the required power, torque, and speed at the propeller/fan as propellers exceeding 1m in length typically require rotation speeds of less than 3 kRPM to avoid excess losses from sonic flows at the blade tips [12], whereas low speed machines can be directly coupled to a propeller/fan. The addition of a gearbox is a disadvantage in AEA due to additional losses generated in the gearbox and the addition of a failure point in the propulsion system. Magnetically geared drivetrains have been proposed as a solution to the gearbox problem for high speed machines [2]. Lastly, superconducting motor designs are a newer technology being considered to achieve very high powertrain efficiencies, although most do not account for the auxiliary cooling systems required to maintain the required temperatures [2]. These systems significantly increase weight, subsequently decreasing power density.

The greatest factor affecting the electrification of larger aircraft is energy storage. While there are a number of motors that exceed the 4.26 kW/kg power density figure from the PW127D mentioned above, energy storage technologies lag behind conventional aircraft fuels in use today. A conventional Lithium-Ion (Li-Ion) battery is only capable of achieving an energy density of 200 Wh/kg whereas Jet-A1 kerosene has an energy density of 11.95 kWh/kg, an almost 60-fold increase over the current conventional battery technology [12]. Interest in metal-air batteries has increased recently due to the theoretical power densities as outlined in [13], which shows that battery technologies such as lithium-air and iron-air can meet and exceed the energy densities of Jet-A1 with theoretical energy densities of 11.7 kWh/kg and 14.7 kWh/kg respectively. The largest downside is the single-use nature of metal-air batteries since they work on the principles of reduction and oxidation, therefore they cannot be recharged with input current [13].

## 2.2 Hybrid Architectures

Due to the difficulty in achieving the required power densities and energy densities in motors and batteries with current technologies, hybridization is required as a first step towards AEA for larger aircraft applications. Aircraft electrification can be broken down into three categories: full electric, series hybrid and parallel hybrid. Between the hybrid architectures, there are variations that result in a number of similar hybrid configurations. The main hybrid architectures found in the literature are shown in Fig. 2.1. Turboshafts, which primarily are used to generate power for motors and batteries, and turbofans, which generate thrust and can be used to generate power, are the primary fuel consuming units shown in Fig. 2.1. However, these components can be replaced more generally with "thermal engines" to include piston driven engines, which can also be used to generate power and thrust.

Series architectures use electric motors as the sole thrust generating units used to drive the propulsors (i.e. propeller or fan) as shown in Fig. 2.1b). A thermal engine, in conjunction with a generator, provides charge to an onboard battery or directly to the drive motors. The main advantages with series architectures are [14]:

- Ability to operate thermal engines at the point of highest efficiency.
- Mechanical decoupling of the thermal engine and generator from the motors which provides freedom to position the power generating unit(s) separately from the propulsion motor(s).
- Smaller permissible thermal engines since batteries can provide the missing power during peak power operating conditions.

The main disadvantages of a series architecture are:

- Additional weight from a generator.
- Losses from energy conversion and transmission between components.

A turbo electric architecture is similar to a series architecture in that a gas turbine and generator supplies power to the electric drive motors, however, there is no onboard battery and the energy used to drive the electric motors comes solely from the gas turbine and generator units as seen in Fig. 2.1c). A partial turbo electric architecture, shown in Fig. 2.1d), replaces the turboshaft in a turbo electric architecture with a turbofan to provide electrical power and thrust. This makes the partial turbo electric

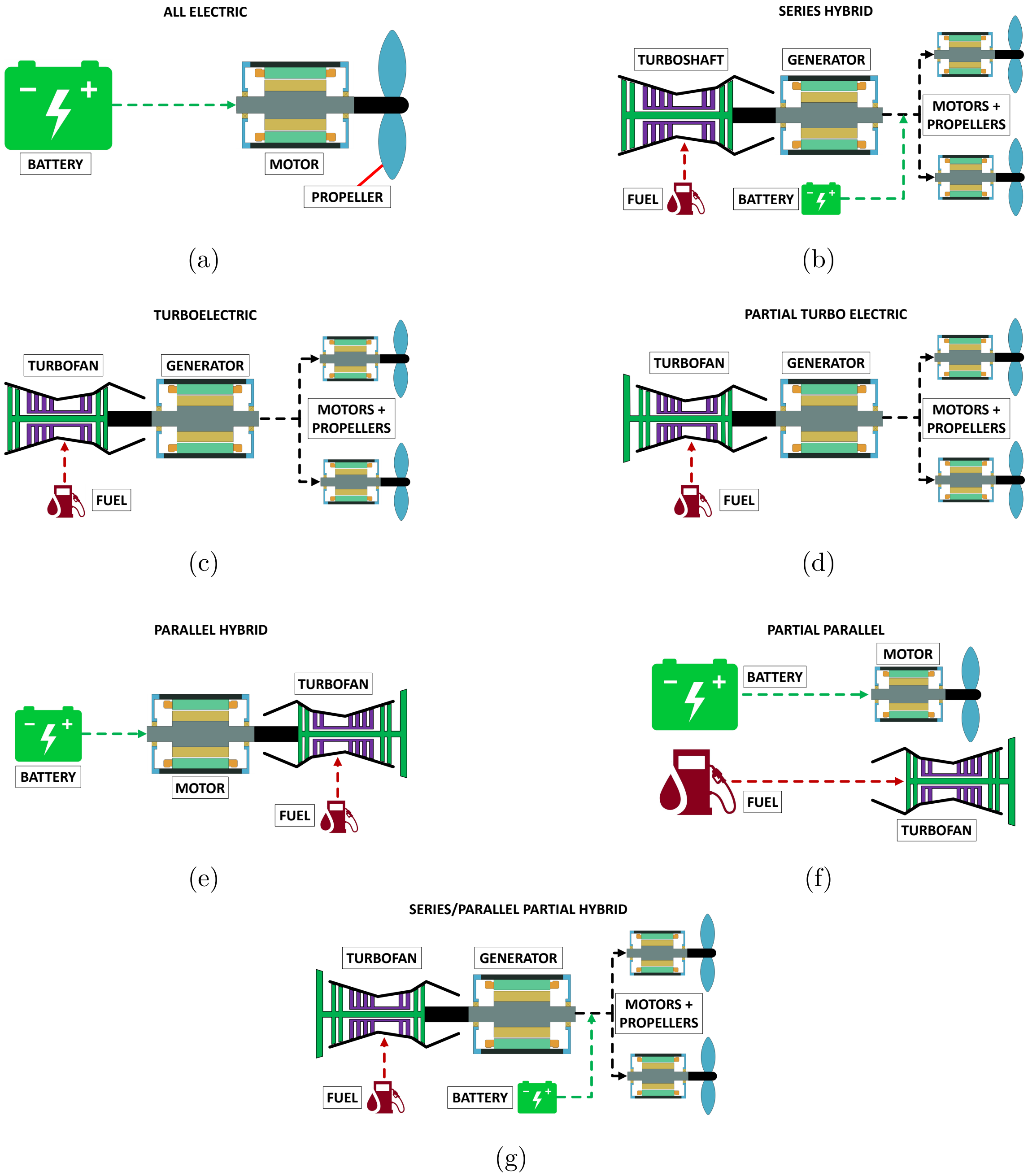


Figure 2.1: Aircraft electrification architectures [1], [14]; (a) Fully electric, (b) Series hybrid, (c) Turbo electric, (d) Partial turbo electric, (e) Parallel hybrid, (f) Partial parallel, (g) Series/parallel partial hybrid.

architecture resemble a parallel architecture without the presence of a battery.

Parallel architectures use the thermal engine to provide thrust along with the drive motors as opposed to solely charging the batteries or providing electrical power to the drive motors. The use of turbofans, or thermal engines with propulsors, and the lack of generators, as shown in 2.1e, separates the parallel architecture from the series architecture. The main advantages of a parallel architecture are [14]:

- Increased reliability due to the use of separate machines that provide propulsion.
- Smaller permissible electric drive motors due to the presence of the thermal engines which can provide continuous/intermittent boosts in thrust.
- Lower weight compared to the series architecture since a dedicated generator is eliminated for the propulsion system, electing to use the drive motor as a generator when necessary.

The disadvantages of the parallel architecture are:

- Close proximity of the thermal engine(s) to the electric motor(s) since the components are mechanically coupled.
- Potentially more complex mechanical connections since various clutches and gearbox connections may be used to decouple the thermal engine and electric motor.

One variation of the parallel architecture is the partial parallel architecture as shown in Fig. 2.1f) [14]. This should not be confused with the series/parallel partial hybrid architecture shown in Fig. 2.1g) which uses the thermal engine to charge the batteries or directly power the motors through the generator while also providing thrust. The partial parallel architecture in Fig. 2.1f) completely segregates the thermal engine system and the electric drive motor system. A battery directly powers the drive motors which generates thrust using the attached propulsors while a separate turbofan or thermal engine with an attached propulsor provides thrust without any direct connection between the electric and fuel powered systems. It should be noted that this architecture does not require the thermal engine and motor(s) to be in close proximity since the components are not mechanically coupled.

Hybridization improves the feasibility of aircraft electrification over fully electric architectures, especially for larger, long range aircraft. Energy storage and electric motors can be downsized to improve overall power and energy densities of the entire propulsion system to reduce the gap between conventional technologies. Out of the presented hybrid architectures, [15] identified the turbo electric architecture to be the most feasible hybrid architectures that is likely to enter into service within the next three decades.

## 2.3 Electric Machines Today

Power densities of electric motors have been steadily increasing over time and are now reaching levels that are adequate to be used in the hybridization and full electrification of turboprop single-aisle aircraft. With the steady increase in power densities, more companies have begun to develop electric motors specifically for aircraft propulsion.

A summary of electric motors available on the market today is shown in Table 2.1. The power, torque, and power density figures listed in the table are limited to their respective continuous operating condition. This is because the peak operating condition of an electric motor is generally thermally limited to short durations and is therefore reserved for takeoff and/or emergency situations. Maximum continuous operating conditions offer a more realistic view of the performance and power density of the machine as it serves as the performance ceiling for a majority of the flight profile. Additionally, the continuous operating condition serves as a point of comparison between the motors shown and the motor proposed in this thesis. It should be noted that MagniX, Safran, Emrax, Rotax, and Helix have a relatively large range of motors, but for brevity many models were excluded. Instead, some motors were chosen from the available range, including motors towards the low and high ends of the power range and power densities from the list of available motors. A number of recent and ongoing aircraft electrification projects are summarized in Table 2.2, some of which use the motors referenced in Table 2.1.

Most of the motors developed for aerospace propulsion applications on the market today are motors with rotation speeds far lower than 10 kRPM indicating that they are intended for direct drive propulsion. The Safran GENeUS300 and H3X HPDM-250 are two notable high speed motors that are intended for generator and propulsion applications, however a gearbox is required for propulsion due to the high output shaft speeds. Helix also offers high-speed motors, however it is not explicitly stated whether the intended use for their motors includes propulsion applications, unlike Safran and H3X, and generally show that their motors are also intended for a variety of other application, such as automotive and marine [16]–[19].

The power densities of the motors displayed in Table 2.1 have a considerable range, with a number of motors having power densities under 5.0 kW/kg, which are better suited for GA aircraft. Emrax, YASA, Rotex, Kite Magnetics, and Evolito offer motors that are well suited for this application. Siemens developed the SP70D, and later the SP260D, for fully electrified 1-2 seater demonstration aircraft, however their motors have seen minimal use outside of aircraft developed or converted by Siemens themselves for demonstration purposes with aircraft such as the Siemens Extra 330LE using the Siemens SP260D motor [20]. Some Emrax motors have been used for small aerospace electrification projects such as the Pipistrel Taurus Electro and Sunseeker duo, two electric glider projects that both used the Emrax 228 motor [21]. YASA is a leader in axial flux motor technology in the automotive industry, however their motors are also viable for aerospace propulsion. This was illustrated by the use of three YASA P400 motors in the Rolls Royce Spirit of Innovation demonstrator aircraft, achieving the fastest climb rate to 3000 meters and highest top speed over 3 kilometers and 15 kilometers of any fully electric aircraft [22]. Evolito was established in 2021 as a spin-off from YASA to commercialize their axial flux motor technology for the aerospace industry. The D500 and D1500 from Evolito are both suitable for GA aircraft, however the D500 provides an exceptional power density of 8.2 kW/kg and the relatively small axial footprint of 123 mm allows for stacking multiple power units without occupying a large amount of space. This offers aircraft design flexibility and improves its viability for larger aircraft that require larger power outputs. MAGicALL and Rotex also make electric motors for aerospace applications.

The MAGicALL MAGiDRIVE motors were selected for the CityAirbus NextGen eVTOL demonstrator aircraft, currently in its design phase [23], [24]; however, no other well known applications of the MAGiDRIVE motor currently exist.

For commercial aviation, MagniX is the current leading provider of Electric Propulsion Units (EPUs), which combines the motor and inverter into a single package, as demonstrated by multiple commercial aircraft electrification projects utilizing MagniX EPUs shown in Table 2.2. MagniX does not openly disclose the weights of the motors within their EPUs so the motor power density cannot be directly compared with other motors on the market. Their use in recent projects can be attributed to the production of EPUs targeted towards commercial aviation projects as early as 2019 when the Magni250 was initially offered for the Eviation Alice and was later replaced by the Magni650 [25]. In March of 2023 Safran released the ENGINeUS XL line of motors targeted for commercial aviation [26], [27]. H3X is currently developing the HPDM-1500 and HPDM-3000 motors which are also targeted for commercial aviation, however motor performance metrics are largely based on simulations and dynamometer data from the HPDM-250 [28]. The HPDM-250 is an EPU, similar to the units offered by MagniX, but in a much more compact package where the inverter is integrated with the motor into a single casing, whereas the motor and inverter are separate units connected with HV cables in EPUs offered by MagniX. The HPDM-250 achieves an impressive 15.4 kW/kg with the EPU alone or 12.0 kW/kg with the optional integrated 4:1 or 6.7:1 gearbox which is critical to reduce the output speeds for a direct drive propulsion application from the output shaft of the EPU. One way H3X achieves these power densities is with the use of an additively manufactured cooling jacket used to cool the stator and inverter [28]. As previously mentioned, H3X is currently developing the HPDM-1500 and HPDM-3000, two megawatt level EPUs that rely on the core technology from the HPDM-250 to drive larger aircraft. However, unlike the HPDM-250, the output speeds of the megawatt-level motors are less than 3000 RPM, making them suitable for direct drive propulsion. Additionally, the small axial footprint of the machines allow for stacking of 8 and 6 units axially for the HPDM-1500 and HPDM-3000, respectively [29], [30].

Aircraft electrification projects began with a number of small GA aircraft like the Rolls Royce Spirit of Innovation and Siemens 330LE, which were fully electrified conversions of piston engine aircraft. The Diamond DA-36, the predecessor to the newer eDA40 shown in Table 2.2, and eGenius HPH are two other examples of small GA aircraft that have been successfully designed and tested from the ground up in the last 10 years. Newer small GA aircraft are currently under development for demonstration and commercial purposes like the Airbus Ecopulse, Diamond eDA40, NASA X-57, Volta Volaré, and Voltaero Cassio330, however aircraft manufacturers have recently been pushing to develop larger electrified commercial aircraft. Most electrified commercial aircraft projects are still at an early stage in their conceptualization meaning no reliable information is available on aircraft design and performance, and the realization of such projects relies on advancements in battery and/or motor technology. The Bauhaus Ce-Liner is an example of an early concept of a fully electric single row narrowbody aircraft that relies on advancements in battery technology, requiring a target battery energy density of 2000 Wh/kg for the design to be realized [31]. Current electrified commercial aviation projects aim to replace short-duration regional turboprop aircraft with alternatives such as the Maeve M80, APUS i-5, Ampaire Eco Caravan and Eco Otter SX, Faradair BEHA-M1H, and Universal Hydrogen Dash 8. These projects can be divided into two categories: conversions and novel designs. Conversions take existing commercial turboprop aircraft and retrofit them with a hybrid or fully electric propulsion and energy storage system. The Ampaire Eco Caravan, Ampaire Eco Otter SX, and Universal Hydrogen Dash 8 are all conversions of the Cessna 208B Grand Caravan, De Havilland DHC-6 Twin Otter, and De Havilland Dash 8 respectively. The remaining commercial aircraft mentioned, the Maeve M80, APUS i-5, and Faradair BEHA-M1H, are novel designs that are early in their design phases.

Table 2.1: Summary of commercially available electric motors for aerospace propulsion. The performance metrics shown are for continuous operation.

| Company | Model | Continuous Power (kW) | Speed (kRPM) | Torque (Nm) | Motor Type | Weight (kg) | Power Density (kW/kg) | Cooling Method |
|---|---|---|---|---|---|---|---|---|
| MagniX* [25] | magni350 EPU | 350 | 2.3 | 1608 | RF PMSM | 128 (w/ inverter) | - | Oil cooled motor |
| | magni500 EPU | 560 | 1.9 | 2814 | RF PMSM | 185 (w/ inverter) | - | Oil cooled motor |
| | magni650 EPU | 700 | 2.3 | 3216 | RF PMSM | 206 (w/ inverter) | - | Oil cooled motor |
| Safran* [26], [27], [32] | GENeUS 300 | 300 (Peak) | 42.0 (Peak) | - | - | 30 | 10.0 | Liquid cooled |
| | ENGINeUS | 70 | 2.5 | - | - | - | 2.5 | Liquid cooled |
| | ENGINeUS XL | 1000 | 1.9 | - | - | - | 3.5 | Oil cooled |
| Siemens [20], [33], [34] | SP70D | 70 | 2.6 | 260 | RF Outrunner SRM | 26 | 2.7 | External air cooled |
| | SP260D | 260 | 2.5 | 977 | RF Outrunner SRM | 50 | 5.2 | External air cooled |
| Emrax* [35], [36] | 208 | 41 | 4.9 | 80 | AF PMSM | 9.3 | 4.4 | Air cooled rotor, air + liquid cooled stator |
| | 348 | 210 | 9.5 | 500 | AF PMSM | 41.5 | 5.1 | Air cooled rotor, air + liquid cooled stator |
| Yasa [37], [38] | 750R | 70 | 3.0 | 400 | AF PMSM | 37 | 1.9 | Air cooled rotor, liquid cooled stator |
| | P400 | 60 | 4.2 | 200 | AF PMSM | 28.2 | 2.1 | Air cooled rotor, liquid cooled stator |
| Rotex* [39] | REB30 | 30 | 4.0 | 36 | RF PMSM | 8.2 | 3.7 | - |
| | REB90 | 80 | 2.2 | 300 | RF PMSM | 20 | 4.0 | - |
| H3X Motors [28]–[30] | HPDM-250 | 200 | 20.0 | 120 | RF PMSM | 13.0/16.6 | 15.4/12.0 | Liquid cooled |
| | HPDM-1500 | 1400 | 2.5 | 6111 | PMSM | 130 | 10.8 | WEG cooled |
| | HPDM-3000 | 2800 | 1.7 | 16000 | PMSM | 220 | 12.7 | Liquid cooled |
| Helix [16]–[19] | CTSM242-HP | 249 | 15.0 | 31.3 | RF | 31.3 | 8.0 | WEG integrated stator + rotor cooling |
| | SPM242-85 | 287 | 17.0 | 281 | RF | 25.8 | 11.1 | - |
| | SPC330-94 | 366 | 6.0 | 728 | RF | 46 | 8.0 | - |
| | SPX417 | 562 | 2.3 | 2384 | RF | 90.3 | 6.2 | - |
| | SPM177-165 | 618 | 25.0 | 264 | RF | 25.7 | 24 | - |
| Kite Magnetics [40] | KM120 | 100 | 2.5 | 382 | RF PMSM | 34 | 2.9 | Air cooled |
| Evolito [41], [42] | D1500 | 100 | 2.5 | 1200 | AF | 35 | 2.9 | Liquid cooled |
| | D500 | 230 | 8.0 | 280 | AF | 28 | 8.2 | Liquid cooled |
| MAGicALL [43] | MAGiDRIVE 500 | 400 | 3.2 | 950-5000 | RF | 50-100 | 4.0-8.0 | Air cooled |
| | MAGiDRIVE 20 | 16 | 6.2 | 20-100 | RF | 3-6 | 5.3-2.7 | Air cooled |

* Some models are excluded for brevity. Models shown in the table from noted companies include the low and high end of power output and/or power densities from the range of available models.
AF = Axial Flux
RF = Radial Flux
SRM = Switched Reluctance Motor

Table 2.2: Summary of current aerospace electrification projects.

| Company | Model | Operating Speed (KTAS) | Max Payload (lbs) | Range (NM) | Topology | EM Used | EM Peak Power (kW) |
|---|---|---|---|---|---|---|---|
| Airbus [23], [24], [44]–[46] | EcoPulse | - | - | - | Partial parallel, 6 EMs + turboprop | Safran ENGINeUS | 50 |
| | CityAirbus NextGen | 65 | - | 43 | Full electric, 16 EMs | MAGicALL, unspecified | - |
| Ampaire [47], [48] | Eco Caravan | - | 2500 | 1100 | Parallel, unspecified | AMP-H570 | - |
| | Eco Otter SX | - | 3000 | 200 | - | - | 600 |
| APUS [49], [50] | i-2 | 160 | 880 | 500 | Full electric, 2 EMs | - | - |
| | i-5 | 160 | 3900 | 800 | Unspecified hybrid, 4 drive EMs | - | 150 |
| Diamond [51] | eDA40 | - | 397 | 117 | Full electric, 1 EM | Safran ENGINeUS 100 | 125 |
| eGenius [52] | HPH | 108 | 220 | 540 | Full electric, 1 EM | Sineton | 100 |
| Eviation [53] | Alice | 260 | 2500 | 250 | Full electric, 2 EMs | MagniX Magni650 | 700 |
| Faradair [54], [55] | BEHA-M1H | 200 | - | - | Turbo electric, 2 EMs | MagniX Magni500 | 560 |
| Maeve [56] | M80 | 400 | - | 800 | Unspecified hybrid | - | - |
| NASA [57] | X-57 | 150 | 3000 | - | Full electric, 14 EMs | Self-developed | 10.5/60 |
| Rolls Royce [22], [58] | Spirit of Innovation | 336 | - | - | Full electric, 1 EM | YASA P400 | 400 |
| Siemens [33], [34] | Extra 330LE | 182 | - | - | Full electric, 1 EM | Siemens SP260D | 260 |
| Universal Hydrogen [59] | Dash 8 (Conversion) | 170 | - | 500 | Full electric, 2 EMs | MagniX Magni650 | 700 |
| VoltAero [60], [61] | Cassio 330 | 200 | - | 108-648 | Parallel, 3 EMs + ICE | Proprietary | 60 |

## 2.4 Chapter Summary

This chapter provides a broad overview of the current landscape of aircraft electrification for GA and commercial aviation. Current electrification efforts must be accelerated to meet the aggressive emissions targets set by large governing bodies; however, this is challenging due to limitations in current technologies. While electric motors continue to steadily increase in power density, a figure critical to the scaling of aircraft electrification, energy densities of current energy storage systems, namely Li-Ion batteries, seem to be the primary limitation for larger commercial aviation projects. With significant challenges in energy storage, hybrid aircraft propulsion architectures were presented in this chapter as a stepping stone from today's conventional turboprop and turbine aircraft to full electrification. Since this thesis focuses on the design of a power dense electric motor, a number of available motors with their continuous power, torque, speed, and power densities were presented. Safran and MagniX are two notable leaders currently in the space of electric powertrains for aircraft propulsion, however newer companies like H3X have shown impressive performance and power density figures that will help lead the future of aviation electrification. A number of current GA and early commercial aviation electrification projects were introduced, many of which used the motors presented in Table 2.1. A majority of the current electrification projects, including commercial aviation, have jumped to fully electric architectures. It is the author's opinion that more effort should be placed into hybridization. It is possible that manufacturers seek fully electric architectures due to their simplicity, but hybridization may improve the feasibility of low emission aircraft in terms of range and cargo capacity compared to a fully electric aircraft, allowing for scalability of the technology to larger aircraft. With the focus on power dense machines, this thesis continues to explore the thermal management of high speed traction motors to effectively dissipate the inherently higher amounts heat per volume generated by these motors.

# Chapter 3

# Rotor Design in High-Speed Radial Flux PM Machines

As electric machines move to higher speeds to achieve higher power densities, the thermal and mechanical aspects of the rotor design need to be carefully designed to avoid demagnetization in PMSMs and mechanical failure of the rotor. This chapter provides an overview of the thermal design and mechanical considerations for rotors within high-speed radial flux electric motors. First, the sources of losses within the motor are identified, separating mechanical and electromagnetic losses and their locations within the stator and rotor. The next section presents a number of air and liquid rotor cooling designs for high-speed radial flux EMs in literature. Bearing lubrication and cooling, which is of especially high importance in high-speed machines, is also discussed to identify and compare common and reliable lubrication and cooling solutions. Finally, general mechanical considerations are highlighted to provide a mechanical perspective on the rotor design, which may affect the design of the thermal management system for high-speed rotors. The rotor cooling designs highlighted in this chapter are limited to motors used for traction applications that exceed 10 kRPM and 10 kW to more closely resemble the proposed motor. This is because low-speed and/or low power motors may use cooling designs that may be unsuitable for high-speed or relatively high loss magnitudes that are generated in larger, high-speed traction motors. Literature covering bearing lubrication and cooling designs are not subject to the same limitations as the rotor cooling designs since the topic is more universally applicable to applications outside of high-speed traction motors.

## 3.1 Loss Distribution in Radial Flux PM Electric Machines

Losses in an electric motor can be separated into electromagnetic losses and mechanical losses. The subsequent sections discuss the breakdown of the electromagnetic and mechanical losses, introducing equations to describe the losses with the understanding supplier data and/or complex analysis is required to accurately determine most of the presented losses. Instead, the equations provide an understanding on the factors that affect each loss term.

### 3.1.1 Electromagnetic Losses

Electromagnetic losses consist of winding resistance loss, eddy-current loss, and hysteresis loss. Winding resistance loss occurs in the stator windings as a result of the resistance in the wires whereas eddy-current and hysteresis losses occur in all electrically conductive components within the motor. Winding resistance losses in AC motors consist of AC and DC losses. DC losses are calculated using the following equations [62]:

$$P_{DC} = i^2 R = \frac{V^2}{R} \tag{3.1}$$

$$R = \frac{\rho_{cop} \cdot l_{cop}}{A_{wire}} \tag{3.2}$$

where $P_{DC}$ is the DC resistance loss, $i$ is the current, $V$ is the voltage, $R$ is the DC resistance, $\rho_{cop}$ is the electrical resistivity of copper, $l_{cop}$ is the length of wire, and $A_{wire}$ is the cross-sectional area of the conductor. AC losses can be attributed to the skin effect and proximity effect. The skin effect refers to the tendency of AC currents to crowd towards the surface of the conductor and the proximity effect refers to eddy currents created as a result of the electric fields generated by nearby conductors [62]. The total AC losses in the windings of PMSMs is not easily calculated and requires electromagnetic Finite Element Analysis (FEA) to establish the total generated losses. Wire position within the slots, machine operating frequency, airgap flux density, wire geometry/type, and the presence of slot wedges all affect the AC losses. Eddy-current and hysteresis losses occur in the stator and rotor. These losses are both accurately determined with electromagnetic FEA. Electromagnetic losses generated within the rotor hub, shaft, housing, and end plates are generally minimal and are commonly ignored in analysis [62].

### 3.1.2 Mechanical Losses

Mechanical losses are categorized as windage losses and bearing losses. Seal losses and fluid friction losses may also be generated in the rotor depending on the sealing requirements and rotor cooling design. Windage losses occur as a result of viscous shear stresses that generate heat from the high surface speeds at the outer surfaces of the rotor. The flow within the airgap is the greatest contributor to the windage losses of the rotor. The windage loss within the airgap in cases where no axial flow is present can be calculated using the following equation [63]:

$$P_w = C_f \pi \rho \omega^3 r_1^4 l_{gap} \tag{3.3}$$

where $P_w$ is the windage loss, $C_f$ is the skin friction coefficient, $\rho$ is the air density, $\omega$ is the rotation speed, $r_1$ is the outer radius of the rotor, and $l_{gap}$ is the thickness of the airgap. At high speeds, windage losses significantly contribute to the overall rotor losses due to the cubic relationship between the rotor speed and generated loss. The airgap Reynolds number, $Re_{gap}$, can be used to describe the skin friction coefficient to be used in the equation above and is defined as:

$$Re_{gap} = \frac{\rho \omega r_1 l_{gap}}{\mu} \tag{3.4}$$

where $\mu$ is the dynamic viscosity of air. The skin friction coefficient is given by the following equations with the associated ranges for the airgap Reynolds number [63], [64]:

$$C_f = 0.515\frac{(l_{gap}/r_1)^{0.3}}{Re_{gap}^{0.5}},\ 500 < Re_{gap} < 10^4 \tag{3.5}$$

$$C_f = 0.0325\frac{(l_{gap}/r_1)^{0.3}}{Re_{gap}^{0.2}},\ Re_{gap} > 10^4 \tag{3.6}$$

Bearing losses are mainly caused by oil churning and drag. These loss values are a function of operating speed, loading conditions, lubricant type and feed method, lubricant flow rate (in the case of recirculating lubrication), cage design, and seal design. Palmgren [65], [66] developed empirical formulae for determining bearing losses using friction torque and bearing speed. The total friction torque, $M$, generated in a bearing is as follows:

$$M = M_1 + M_2 \tag{3.7}$$

where $M_1$ and $M_2$ are friction torques due to applied load and viscous effects, respectively. The following equations describe the torque due to the applied load:

$$M_1 = f_1 F_\beta d_m \tag{3.8}$$

$$f_1 = z\left(\frac{F_s}{C_s}\right)^y \tag{3.9}$$

$$F_\beta = 0.9F_a cot\alpha - 0.1F_r \text{ or } F_\beta = F_r \tag{3.10}$$

where $d_m$ is the mean diameter, $F_s$ and $C_s$ are the static equivalent load and basic static load rating, respectively, $y$ and $z$ are values that depend on bearing type, $\alpha$ is the contact angle, and $F_a$ and $F_r$ are the applied axial and radial loads. The larger of the two values is chosen for $F_\beta$. The torque due to viscous effects is as follows:

$$M_2 = 10^{-7} f_o (\nu_{lub} n)^{2/3} d_m^3,\ \nu_o n \geq 2000 \tag{3.11}$$

$$M_2 = 160 \times 10^{-7} f_o d_m^3,\ \nu_o n < 2000 \tag{3.12}$$

where $\nu_{lub}$ is the lubricant viscosity in centistokes, $n$ is the speed in RPM, and $f_o$ is a factor that depends on the type of bearing and method of lubrication. It is clear from the equations that $M_1$ is mainly dependent on the axial and radial loading, which includes bearing preload, and $M_2$ depends mainly on the lubricant viscosity and speed while the bearing size, represented by $d_m$ contributes to both torque components. Bearing size has a much larger effect on $M_2$ due to the cubic relationship between the mean diameter and torque.

The overall heat generation of the bearing, $G$, is given by the following equation [67]:

$$G = \pi M n \cdot 30 \times 10^3 \tag{3.13}$$

Palmgren's empirical formulae are valid for low to medium-speed machines [65], [68]. High speed operation requires more complex analysis as centrifugal forces and gyroscopic moments become significant [65]. Wang *et al.* [68] empirically developed a correction factor $n_g$ for high-speed, high-loaded Deep Groove Ball Bearings (DGBB):

$$n_g = -1.65 \times 10^{-12} n^3 + 2.65 + 2.65 \times 10^{-8} n^2 - 1.49 \times 10^{-4} n + 0.3695 \tag{3.14}$$

The corrected total loss generation then becomes:

$$G_{new} = n_g \times \pi M n \cdot 30 \times 10^3 \tag{3.15}$$

Another model developed by SKF considers factors not accounted for by Palmgren's model, resulting in better accuracy at higher speeds for a wide array of bearing types and lower calculated bearing temperatures [68]. A detailed description of this model is outside the scope of this thesis. For more information see [69], [70].

Churning losses generated by lubricants are also affected by cage geometry. Yan *et al.* [71] studied the interaction of different cage designs with oil-air flow within the bearing cavity of an angular contact bearing at speeds up to 60 kRPM. Different cage pocket designs, pocket clearances, guiding surfaces, and guiding clearances were tested to determine the effects of these parameters on the thermal performance of the oil-air lubricated bearings. It was found that each of the named factors of the cage pocket design had various effects on the oil-air flow structures within the bearing cavity, affecting the generated losses and effectiveness of the lubrication system.

Fluid friction losses from liquid cooled rotors and contact shaft seal losses are the final losses generated within electric motors. Fluid friction losses apply to both air and liquid rotor cooling designs. These losses are highly dependent on the geometries within the cooling design, therefore they generally requiring CFD to accurately determine the losses. Depending on the sealing requirements, electric motors may not require contact seals and will opt for non-contact seals or labyrinth seals, resulting in no seal losses. For the best sealing performance, contact seals are required. Contact shaft seals come in many different materials, shapes, and sizes depending on the sealing fluid pressure, operating speed, contamination level, etc. Due to the number of factors present in contact seal design, the generated losses are provided by the seal supplier over a range of surface speeds at the sealing surface. High rotation speeds result in high surface speeds, which can result in excess loss generation, high temperatures, and shaft wear over time leading to increased leakage through the seal and eventual failure.

## 3.2 Rotor Cooling of High-Speed Radial Flux Rotors

Rotor cooling of high-speed power dense PMSMs is becoming increasingly challenging with the need to dissipate higher specific losses with inherently smaller packages. Passive cooling is therefore not a common option for these machines as demagnetization would occur, resulting in performance loss. High speeds introduce challenges for thermal management due to higher windage losses and bearing losses. A series of air and liquid rotor cooling designs for high-speed ($\geq$10 kRPM) radial flux motors for traction applications ($\geq$10 kW) found in the literature are shown in this section. A summary of these rotor cooling strategies can be seen in Table 3.1.

Table 3.1: Summary of recent high-speed radial flux motors in the literature with their associated rotor cooling design.

| Author/Year | Power (kW) | Speed (kRPM) | Rotor Cooling Method |
|---|---|---|---|
| La Rocca *et al.* 2014 [72] | - | - | Passive indirect cooling through stator |
| Connor *et al.* 2019 [73] | - | - | Parallel air cooling paths through the hollow shaft and airgap |
| Josefsson *et al.* 2022 [74] | 385 | 14 | Hybrid cooling using rotor fan and hollow shaft oil cooling |
| Yi *et al.* 2018 [75] | - | 15 | Air self pumped by rotor mounted centrifugal fan through internal heat sink |
| Dong *et al.* 2014 [76] | 140 | 24 | Air cooled by shaft mounted axial fan |
| Kim, Lee, and Yook 2016 [77] | 100 | 27 | Air cooled motor with external air supply and supplementary shaft-mounted airgap fan |
| Boxberg *et al.* 2018 [78] | 100 | 29 | Combined rotor and stator cooled by passing compressed air through radial and axial cooling ducts connected to the airgap |
| Zhu *et al.* 2019 [79] | 15 | 30 | Hybrid ventilation structure with both radial and axial vents in stator and rotor |
| Huang, and Fang 2016 [80] | 100 | 32 | Pressurized air through the airgap |
| Anderson *et al.* 2015 [81] | - | 100 | Cold through-flow air feed through an annular opening to the rotor |
| McCluskey *et al.* 2019 [82] | - | - | Cooling channels in rotor lamination stack |
| Ludois *et al.* 2017 [83] | 55 | 12 | Spray cooling on axial faces of the rotor |
| Audi AG 2018 [84] | 90/125/140 | 15 | Hollow shaft cooling integrated with water jacket cooling |
| Lee *et al.* 2016 [85] | 16.7 | 11 | Hollow shaft cooling integrated with water jacket cooling |
| Gai *et al.* 2017, 2020 [64], [86], [87] | 1,100 | 30 | Hollow shaft cooling |
| Wang *et al.* 2021 [88] | 40 | 14 | Cooling channels integrated in rotor hub, spraying onto end windings |
| Bourhis *et al.* 2022 [89] | 130 | 15 | Spray cooling on axial faces of the rotor |
| El-Refaie *et al.* 2013 [90] | 55 | 14 | Recirculating hollow shaft cooling, inlet and outlet on the same side |
| Assaad *et al.* 2018 [91] | 43 | 10 | Hollow shaft, spraying end windings through radial holes in the shaft |
| Park and Kim 2019[92], Lim and Kim 2014[93], Saleem *et al.* 2022 [94] | 140 | 24 | Cooling channels integrated in rotor shaft and hub, spraying onto the end windings |

### 3.2.1 Air Cooling

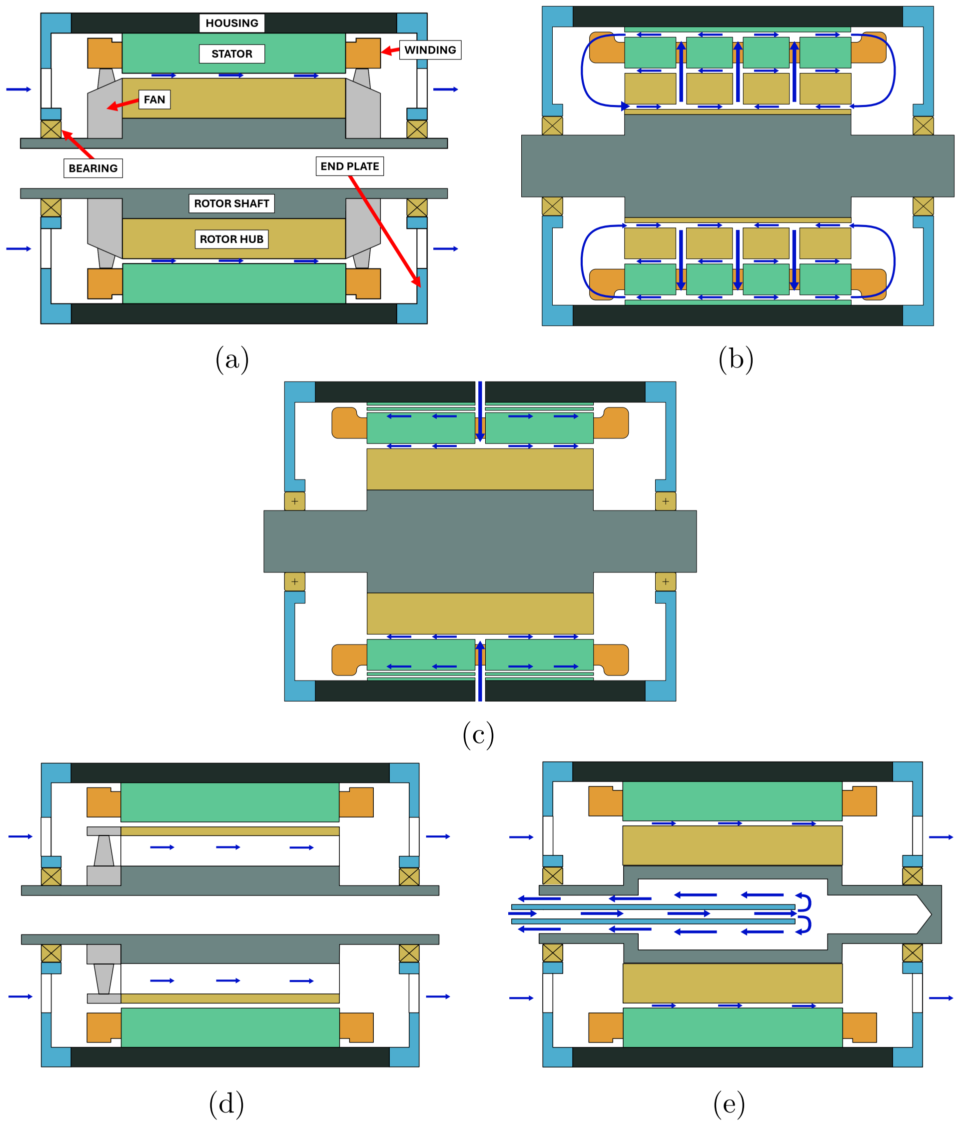


Figure 3.1: Rotor air cooling methods seen in the literature; (a) Internal circulating air through radial and axial channels in the rotor and stator [79], (b) Forced ventilation through stator slots and into the airgap [78], (c) Airgap fan [63], [74], [77], [95], (d) Self ventilated rotor hub fan [63], [75], [79], [96], (e) Air hollow shaft cooling [96]. Blue arrows indicate the path of the air in each cooling design. Blue arrows indicate the path of cooling air flow through the motor.

Air cooling is a popular method seen in the literature and in industry for rotor cooling in high-speed machines. It is classified into three categories: self ventilated, forced ventilated, and enclosed systems. Self ventilated designs utilize a shaft-mounted fan to pump external air through the airgap or through holes within the rotor hub. Forced ventilated systems use external pump to force air through the motor cavity to cool the rotor. Finally, enclosed systems fully seal off the motor cavity to external air, electing to dissipate heat from the rotor to the air within the motor cavity and through the housing using convection. The fully enclosed system is the most passive cooling type out of the three categories.

To maximize the effectiveness of the fully enclosed system, motors may use an integrated fan, also known as a wafter, on each side of the rotor to agitate the surrounding air and improve the forced convective heat transfer on the rotor surfaces exposed to the air within the motor cavity. This heat is evacuated to the ambient air outside the motor through the housing which may use external fins to further improve the heat transfer. Mizuno *et al.* [63], [97] showed a fully enclosed induction motor for traction applications that used wafter fans for a motor with a maximum rotating speed of 6 kRPM. The benefit of such a design is the lack of disassembly and maintenance required for an equivalent self ventilated design. This design is not common for high-speed power dense machines due to the high windage losses generated from the wafter and limited cooling capacity of the internal air. Additionally, the design seen in [63], [97] shows that the power densities of similar fully enclosed designs is limited due to the additional equipment required to release heat to the surrounding air through a heat exchanger mounted to the housing.

Airgap fans like the one shown in Fig 3.1a) have been used in high-speed machines to provide air flow through the airgap and cool the rotor [63], [74], [77], [95]. Introducing axial air flow within the airgap must be controlled such that the additional windage losses generated from the higher relative flow velocity does not outweigh the cooling effect generated by the air gap fan. Nusselt number correlations for airgap flows with axial flow have been covered by the Gronwald and Kern [98]. Kim *et al.* [77] analyzed the improvement in thermal performance of a 100 kW 30 kRPM motor from the use of two airgap fans to cool the rotor while using external air to cool the rotor and stator. The analysis showed a significant increase in the total heat transferred from the rotor and stator from 2095 W to 3013 W with the inclusion of the airgap fans. Additionally, the heat transfer rate within the airgap alone saw a significant jump from 782 W to 1,675 W, resulting in an reduction of approximately 100°C in the maximum rotor temperature. Airgap fan designs were presented in [74], [95], however the thermal performance of the motor was not compared with one that did not use an airgap fan.

Another self driven air cooling strategy uses integrated fans or other component geometries to pump air through holes in the rotor hub as shown in Fig. 3.1d) [63], [75], [79], [96]. Yi *et al.* [75] developed a 15 kRPM outer rotor radial flux motor for aerospace propulsion with a power density target of 13.6 kW/kg. The integrated centrifugal fan primarily pulls air through a heat sink attached to the stator inside the motor cavity, however the air pulled through the motor provided some cooling to the rotor along with the heat transferred directly from the rotor to the ambient air due to the outer rotor configuration. High-speed outer rotor motors are not common in the literature for traction applications. Jaeger *et al.* [96] used a hollow shaft cooling approach to cool a 30 kW, 10 kRPM motor. An integrated fan on the inner diameter of the rotor shaft pumped external air from a stationary feed tube through an annular gap formed by the rotor inner diameter and stationary feed tube as seen in Fig. 3.1e). The cooling air does not contact the air within the motor cavity. The effect of the rotor cooling was determined by comparing the temperature field of the motor with and without the hollow shaft cooling. It was found that rotor cooling solution resulted in a maximum of 40°C drop in the magnet temperature at the peak operating condition, improving the time spent at the peak operating point by 50%. Zhu *et al.* [79] presented a unique solution to the self driven air cooling approach for a 15 kW, 30 kRPM motor. A number of axial and radial vents in the rotor and stator created a ventilation system for both components with clapboards within the radial vents of the rotor driving the flow through the channels as shown in Fig. 3.1b). The highest temperature rise figure was reduced by 26.5°C and the PM temperature rise was reduced by 6.1°C.

Boxberg *et al.* [78] studied air cooling of a 100 kW, 29 kRPM surface mounted PM motor using compressed air injected at the middle of the airgap through radial ducts in the stator, which is shown in Fig. 3.1c). The study showed that the cooling system was robust and reliable to keep the magnet temperatures well within their temperature limits. Anderson *et al.* [81] studied forced convection through the rotor cavity with external air pumped in to cool a 30 kRPM motor. Taylor-Couette flow structures with axial flow were numerically analyzed and novel correlations were provided for the motor's geometry and speeds. Connor *et al.* [73] conducted CFD analysis on a forced air cooled design similar to [81] by pumping air through the airgap with additional rotor cooling provided through a liquid-cooled hollow shaft. The results showed a limit to the provided axial flow through the airgap at which point higher axial flow rates led to much higher windage losses resulting in a net heating effect.

### 3.2.2 Liquid Cooling

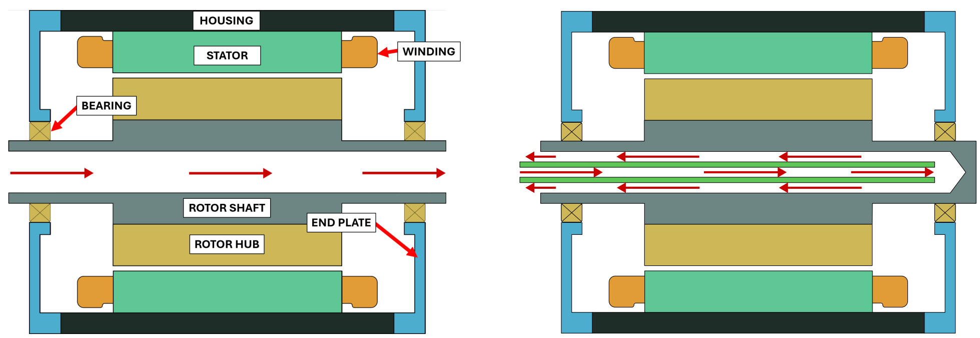


(a) (b)

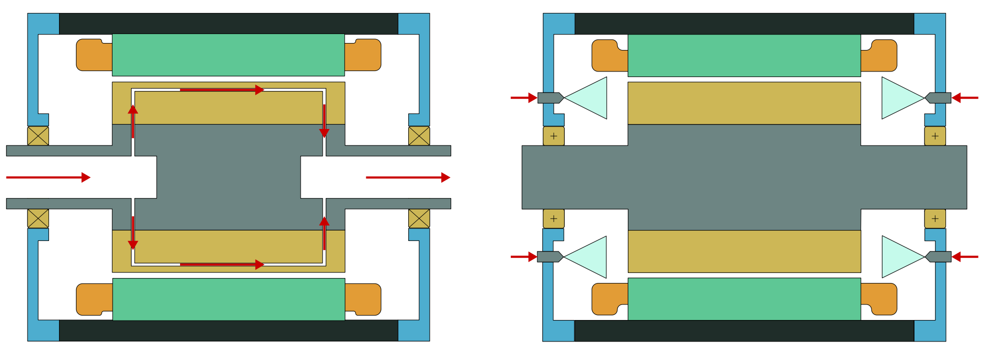

(c) (d)

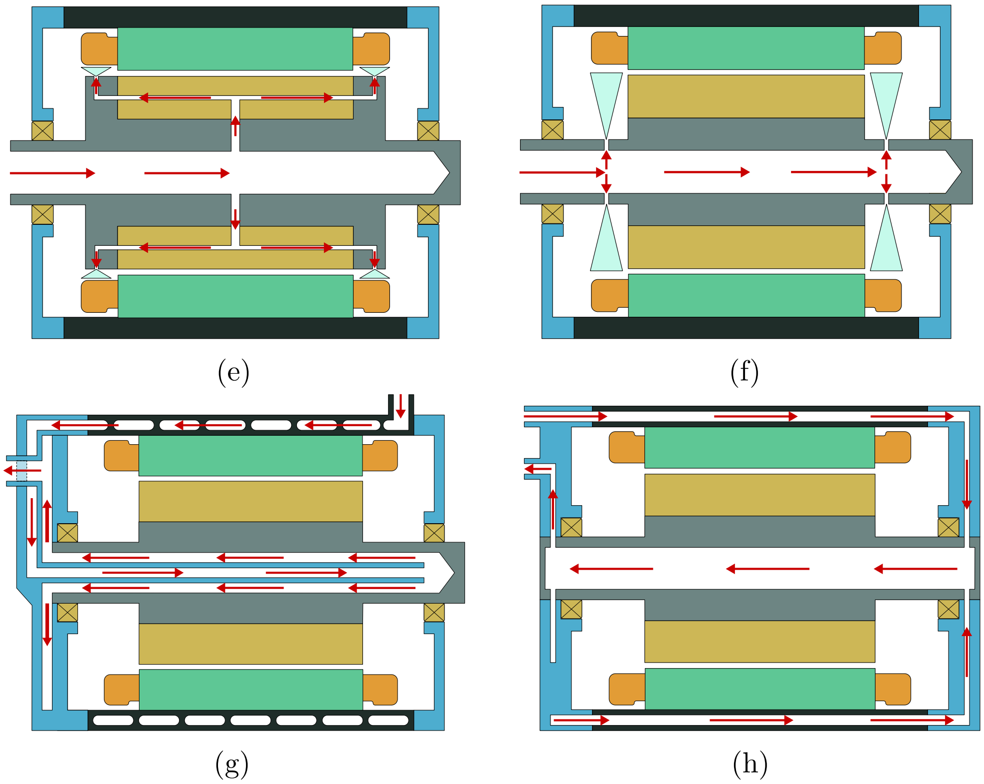

Figure 3.2: Rotor cooling methods seen in literature: (a) & (b) Simple hollow shaft cooling design variations [64], [68], [84], [87], [90], [99], [100], (c) hollow shaft cooling with coolant pumped through the rotor hub [82], (d) spray cooling onto the ends of the rotor hub and windings [83], [101], (e) hybrid cooling through the rotor hub with spray cooling to the end windings [85], [92]–[94], [102], (f) hybrid cooling through a simple hollow shaft spraying onto the end windings [89], [92]–[94], [102], and (g) & (h) combined stator-rotor cooling variations [84], [85]. Red arrows indicate the path of the coolant within the motor.

Most liquid rotor cooling designs introduce coolant to the rotating assembly through the hollow rotor shaft which can be challenging due to the mechanical provisions required to achieve this task. High surface speeds also limit the types of contact seals that can be used to isolate the liquid cooling channel inside the rotor from the motor cavity in cases where sealing is required. Liquid cooling can be separated into a few categories: hollow shaft cooling, spray cooling, hybrid cooling methods, and combined rotor-stator cooling systems. Flood cooling is also a liquid cooling method that is commonly used to cool the stator and can also be used to cool the rotor by increasing the fluid so that it enters the air gap. This is generally not favourable for high-speed machines due to the sharp increase in viscous losses within the airgap [91].

### 3.2.3 Hollow Shaft Cooling

Hollow shaft cooling is a common method used to cool components within the rotating assembly without introducing fluid to the air gap or motor cavity. Hollow shaft cooling systems in high-speed machines are arranged in one of two configurations, as shown in Fig. 3.2. The inlet and outlet of the hollow shaft may be placed on opposite ends of the rotor shaft [63], [64], [87], [99], [100] as seen in Fig. 3.2a) and Fig. 3.2c) or on the same side of the rotor shaft [68], [84], [90]as shown in Fig. 3.2b). In the recirculating hollow shaft design, where the inlet and outlet are on the same side of the motor, a stationary inlet tube attached to the motor casing is placed within the hollow shaft to redirect coolant from the stationary tube and through the hollow shaft in the direction of the inlet. The outlet of the hollow shaft is the annular gap formed by the stationary inlet tube and the shaft inner diameter.

The heat transfer characteristics inside a rotating hollow shaft are complex. A secondary flow occurs due to the rotation, which causes the fluid to be pushed against the inner walls of the shaft from centrifugal effects [99]. Gai *et al.* [63], [64], [87], [99], [100] developed heat transfer correlations for hollow shaft cooling flow using the following dimensionless parameters:

$$Nu = \frac{h \cdot D_h}{\lambda} \tag{3.16}$$

$$Re_a = \frac{\rho \cdot D_h \cdot V_a}{\mu} \tag{3.17}$$

$$Re_r = \frac{\rho \cdot D_h \cdot V_r}{\mu} \tag{3.18}$$

$$Pr = \frac{\mu \cdot c_P}{\lambda} \tag{3.19}$$

where $Nu$ is the Nusselt number, $Re_a$ is the axial Reynolds number, $Re_r$ is the radial Reynolds number, $Pr$ is the Prandtl number, $h$ is the heat transfer coefficient, $D_h$ is the hydraulic diameter, $\lambda$ is the thermal conductivity, $c_P$ is the specific heat capacity, $V_a$ is the average axial velocity, and $V_r$ is the tangential speed at the surface of the channel.

Hollow shaft cooling is more beneficial at higher rotational speeds due to the significant increase in the heat transfer coefficient[87], [100]. The rate of change of the heat transfer coefficient reduces as the rotational speed increases past 10 kRPM in the hollow shaft geometry shown by Gai *et al.* [87]. The heat transfer coefficient in the shaft is largely independent of the flow rate through the hollow shaft as indicated by experimental data and the exclusion of the axial Reynolds number in the resulting empirical Nusselt number correlation proposed by Gai *et al.* [87]:

$$Nu = 3.811 \times 10^{-3} \left( \frac{1}{Re_r \cdot Pr} \right)^{-0.641} \tag{3.20}$$

### 3.2.4 Spray Cooling

Spray cooling is common when it comes to cooling the end windings of a motor using manifolds and nozzles that work together to evenly distribute coolant [101], however spray cooling may also be used to cool the rotor. Unlike hollow shaft cooling, spray cooling exposes the coolant directly to the electromagnetic components which limits the coolants to ones with high dielectric strengths only such as Automatic Transmission Fluid (ATF). Radial flux motor topologies restrict coolant from being sprayed anywhere but each end of the rotor. The thermal path from the rotor's center to the rotor hub's ends will cause a sizeable axial temperature gradient within the hub. This may lead to demagnetization occurring near the middle of the rotor. Radial flux machines with a shorter rotor length may benefit from this cooling design. Proper coolant selection is critical when considering an active cooling method that exposes internal electromagnetic components to the coolant. Properties required for coolant in addition to high dielectric strength are high chemical stability, low toxicity, and good material compatibility [101], [103]. Limited coolant selection, increased risk of short circuits and corrosion, and additional requirements to mitigate frictional losses limit the practicality of an active cooling solution [99]. Ludois and Brown [83] and Bourhis *et al.* [89] presented designs that incorporated spray cooling for the axial faces of the rotor and the end windings, as shown in Fig. 3.2d), although the thermal aspects of the motor were not discussed in detail.

### 3.2.5 Hybrid Cooling Methods

Hybrid rotor cooling systems seen in the literature combine hollow shaft cooling and spray cooling to cool the rotor and end windings, respectively [92]–[94], [102]. This cooling strategy is shown in Fig. 3.2g). Coolant enters the rotor through a hollow shaft, which uses a series of radial channels drilled into the shaft to carry coolant towards corresponding axial channels adjacent to the magnets. These axial cooling channels within the hub distribute coolant along the length of the rotor, providing cooling for the magnets and rotor hub. The fluid exits the hub through nozzles at one end, as in the case of Park *et al.* [92], [94] and Lim *et al.* [93], or both ends, as in the case of Wang *et al.* [102], to cool the end windings. This approach has the additional benefit of minimizing the thermal resistance between the magnets and coolant. Fig. 3.2f) shows a similar hybrid cooling method in which fluid enters through the hollow shaft and sprays onto the end windings through radial holes in the shaft. The cooling benefits to the magnets and rotor hub are reduced since the coolant is not passed through the rotor hub as with the design shown in Fig. 3.2e).

### 3.2.6 Combined Rotor-Stator Cooling Systems

From a practical perspective, it may be beneficial to combine the stator and rotor cooling circuits into a single cooling circuit where possible. This limits the number of components required to complete the cooling system for the motor. The most

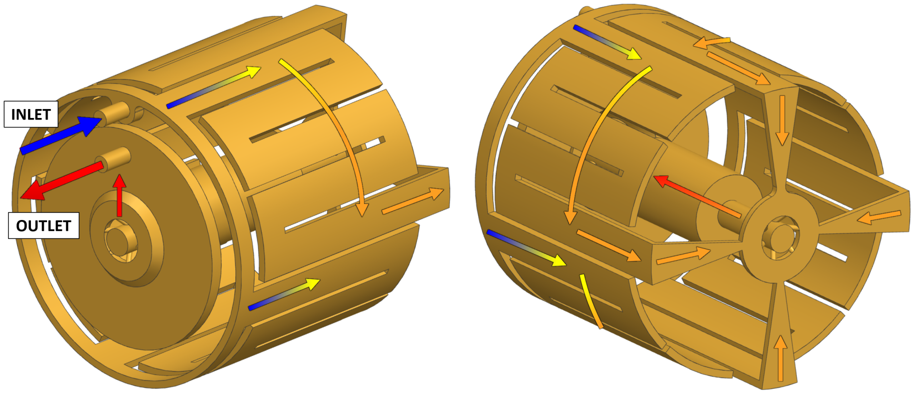


Figure 3.3: Fluid domain representation developed by Lee *et al.* [85]. Arrows indicate the path of the coolant from the inlet (blue) to the outlet (red).

commonly combined stator and rotor cooling systems are the liquid outer jacket and hollow shaft cooling. Audi utilizes a hollow shaft solution for the APA250 and AKA320 drive units and an outer cooling jacket for the stator [84]. The inlet and outlet of the hollow shaft system are placed on the same side of the motor like the one shown in Fig. 3.2b). Using an integrated cooling solution with this layout leads to increased bulk in the motor due to necessary mechanical provisions to direct fluid from the cooling jacket to the hollow shaft.

Lee *et al.* [85] developed an integrated hollow shaft cooling solution in which radial ports drilled through the shaft directed coolant from the motor housing into the center of the shaft as shown in Fig. 3.3. Additional radial ports were drilled at the opposite end of the shaft to evacuate the coolant from the center of the shaft and into the housing once again towards the outlet of the cooling loop. The combined rotor-stator cooling system saw a 50% and 38% temperature decrease in the coils compared to equivalent air cooled and jacket cooled motors, respectively. Although the studied motor was a PMSM, the effects of the designs on the magnet temperatures were not discussed in detail.

The cooling requirements of the motor also limit integrated solutions. As seen in the APA250 and AKA320 motors developed by Audi [84], hollow shaft cooling of the rotor may occur before or after cooling of the stator. Depending on the cooling requirements of the rotor and stator, the fluid passing through the components later in the loop will be at a higher temperature, which leads to higher component temperatures. It should also be noted that the losses generated in the rotor in both motors from Audi are also relatively high since they are induction motors.

## 3.3 Mechanical Considerations

The main mechanical consideration of high-speed radial flux motors are covered in this section. Bearing lubrication is first introduced, comparing the effectiveness of different lubrication methods for heat dissipation and lubricant distribution in high-speed motors. General design principles of the rotor and hub design are then discussed, highlighting the general construction, stresses, and dynamics of the rotating assembly.

### 3.3.1 Bearing Lubrication

Bearings in electric motors may be cooled by active or passive means. The most common method for bearing cooling and lubrication is using oil. Oil may be injected into the bearing cavity as a jet or oil-air mist, which atomizes the incoming oil before being injected into the bearing cavity. Passive cooling methods can provide cooling to the inner and outer rings of the bearings without any contact between the coolant and the rolling elements or cage. It is typically paired with grease lubrication for the bearings. The main disadvantages of grease lubrication are higher churning losses due to higher viscosities compared to oils, and the requirement to use a more passive cooling solution at the outer or inner raceway, which both lead to higher temperatures. The speed factor $DN$ is a useful term to relate the rotational speed and size of bearings and is given by:

$$DN = \frac{D+d}{2} \cdot n_{max} \tag{3.21}$$

where $D$ and $d$ are the outer and inner diameters in millimeters, respectively, and $n_{max}$ is the maximum speed in RPM. According to Pinel *et al.* [104], grease and splash lubrication are preferable for low-speed applications with speed factors less than 200,000 mm min$^{-1}$. However, speed limits for grease lubrication vary depending on many factors, including whether passive cooling methods are used to cool the bearing.

An oil bath is another lubrication method that may cool the bearing when using a re-circulation system to flow relatively low-temperature oil through the bearing. This method is mainly suitable for low-speed applications up to 300,000 mm min$^{-1}$ without frequent oil changes [105]. Higher churning losses lead to significant reductions in speed rating for bearings using oil bath cooling. SKF [69] suggests the a maximum speed of a bearing using oil bath lubrication should not exceed 0.3 to 0.4 times that of oil jet lubrication. It is also important that the oil level does not exceed half the diameter of the lowest rolling element. Exceeding this level leads to foaming and higher churning losses.

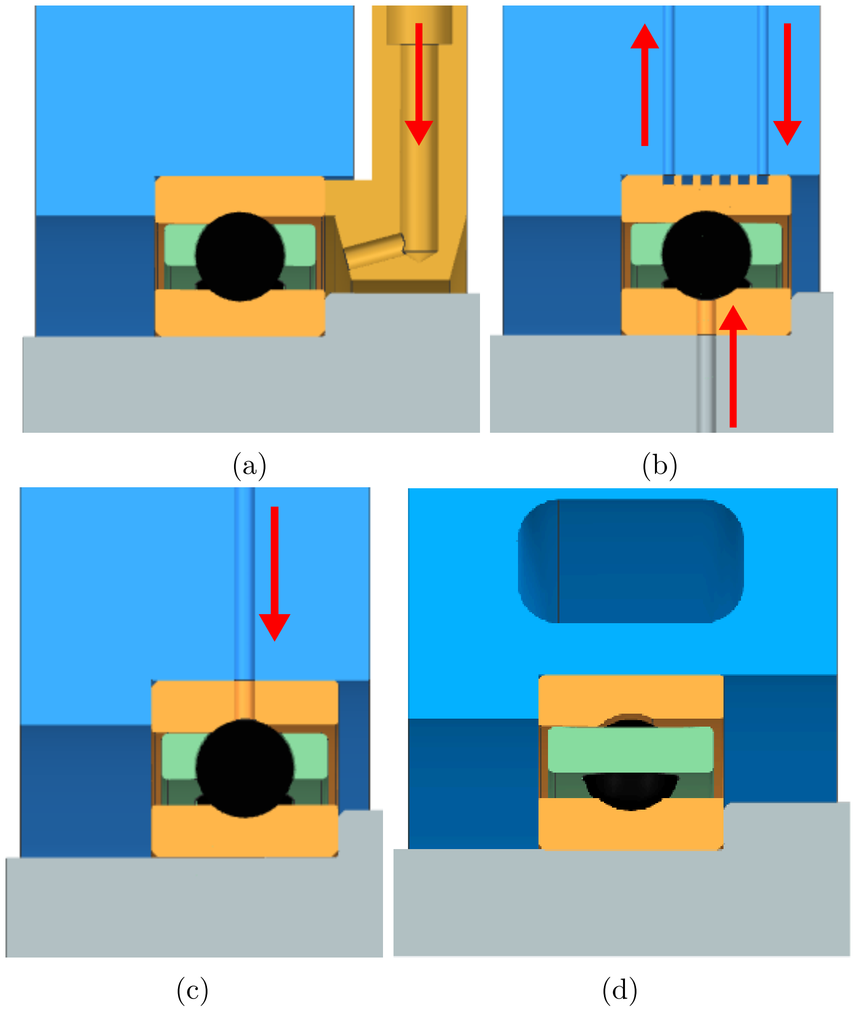


Figure 3.4: Common bearing cooling strategies (a) passive cooling channel in the housing [84], [106], (b) outer raceway spiral channel with inner raceway oil jet [107], [108], (c) oil jet/oil air mist [69], [104], [109]–[112], and (d) outer race jet [113].

Oil jet lubrication is commonly used to lubricate bearings in high-speed electric motors. The system mainly contains an external sump, pump, heat exchanger, and filter [69]. One or more cooling jets are placed adjacent to one of the ends of the bearing, as seen in Fig. 3.4a). Oil injected into bearings is quickly flung outwards within the bearing cavity, especially at high speeds. Therefore, jets should be pointed towards the inner raceway to maximize the cooling and lubrication effects of the incoming oil. However, inner ring-guided cages may partially obstruct the oil jet which may increase churning losses [69]. Jet lubrication of bearings is highly complex due to the two-phase flow present within the bearing cavity and its interaction with the races and rotating elements. Factors that significantly affect oil jet lubrication, other than the bearing geometry and operating condition, include oil flow rate, nozzle angle, nozzle location, and the number of jets. Centrifugal forces that push the oil-air flow towards the outer ring reduce the cooling effect of the oil on the inner ring, creating a non-uniform radial temperature distribution with higher temperatures seen at the inner ring. Additionally, the oil-air volume fraction within the bearing cavity varies in the circumferential direction, decreasing in the direction of rotation from the peak oil-air fraction at the jet's injection point. High speeds reduce the variation in the circumferential direction because of the greater ability of the rolling elements to carry the lubricant along the direction of rotation. The maximum temperature variation shown in simulations of a bearing at 10 kRPM with 5.0 kN of axial load in [109] is 7°C on the inner ring. Similar simulations of a 10 kRPM bearing at 5.0 kN of axial load in [111] showed a maximum temperature variation of 7°C on the outer ring, while inner ring temperatures were not shown. The effect of additional jet nozzles in high-speed bearings has been evaluated by multiple authors [110]–[112]. At the same net flow rate, multiple jet nozzles show a more uniform oil-air distribution in the circumferential direction than single jet nozzles. Wu *et al.* [112] simulated bearings at speeds of up to 40 kRPM using between 1 to 6 jets. The effect of the number of nozzles on the oil-air volume fraction was greatest at lower speeds and negligible at 40 kRPM due to the effect of even lubrication and cooling at higher speeds.

Oil-air mist cooling is similar to jet cooling in that oil enters the bearing cavity using a similarly shaped nozzle, as shown in Fig. 3.4a), yet oil flow rates in oil-air mist applications are significantly lower than in jet cooling. An advantage of oil-air mist lubrication in high-speed applications is reduced churning losses [104]. However, oil-air mist has a significantly lower cooling capacity when compared to oil jet cooling because bearing temperatures are primarily a function of flow rates. Pinel *et al.* [104] compared oil jet to oil-air mist cooling in angular contact bearings for turbomachine applications in the speed range of 30 kRPM to 65 kRPM. Because of the reduced oil flow rates in oil-air mist cooling, the bearing experienced higher ring temperatures at all tested speeds even though the oil temperature used for the oil-air mist was 72 °C lower than that of the oil jet. Due to higher temperatures in oil-air mist-lubricated bearings, an oil jet is the preferred cooling method for high-speed bearing applications. Oil-air mist cooling should still be considered for high-speed traction applications where bearing losses are not excessive. A full system thermal analysis should determine the efficacy of oil-air mist cooling for each high-speed bearing application.

Similar jet lubrication methods exist that necessitate modifications to the bearing raceways to accommodate the oil jet lubrication. Less commonly seen than conventional jet cooling, which uses an external jet to direct fluid to one of the races, the under-race lubrication method introduces fluid through radially drilled holes in the inner raceway as seen as a part of Fig. 3.4b). Under-race lubrication is often used in dual-rotor systems of aero-engine bearings. Jiang *et al.* [114] and Bao *et al.* [115] studied under-race lubrication for high-speed applications. Although the oil injection method slightly differs from conventional jet cooling methods, the trends seen in the oil-air volume fraction with varying ring speeds, oil flow rates, and number of nozzles are consistent with those seen in conventional oil jet cooling. Since these authors do not directly compare this lubrication method to oil jet lubrication under the same operating conditions, the differences between these methods cannot be directly compared.

Yan *et al.* [113] compared oil-air flow in outer-race cooled bearings as shown in Fig. 3.4c), which injects fluid into the bearing cavity from the outer ring, to the oil-air flow seen in conventional oil jet lubricated bearings between 10 kRPM and 50 kRPM. The nozzle position greatly affected the flow and heat transportation inside the bearing cavity. In the conventional oil jet lubricated bearing, flow blockages created by the bearing components are smaller than that of the outer-race cooled bearing, resulting in better heat dissipation. However, lubricating oil supplied from the outer ring was shown to be concentrated in the raceways and cage pocket, which provided a higher utilization rate for the lubricating oil. Practical temperature differences between the two lubrication methods were minimal, with a maximum temperature difference of 2.5°C at 10 kRPM [113].

Outer-race passive cooling methods have been used for high-speed bearings, as seen in Audi's APA250 and AKA320 drive units [84], as well as in the literature on applications extending beyond traction motors [106]–[108]. Outer-race passive cooling may be sufficient in low-load applications (i.e., relatively low speeds and/or bearing axial and radial loads). Coolant is passed through a channel within the housing surrounding the bearing, as shown in Fig. 3.4d). These applications typically use grease lubrication, which increases churning losses at high speeds. Another limitation of outer-ring passive cooling is that the temperature of the inner ring is relatively high due to the lack of cooling supplied to the inner raceway. The main benefit of passive cooling methods is that they can easily be integrated with other cooling systems in the motor, such as the water jacket used to cool the stator [84], [106].

Gloeckner *et al.* [107], [108] improved the outer-ring passive cooling method by cutting channels into the bearing outer raceway in a tight helical shape, with an inlet and outlet at each end of the helix as shown in Fig. 3.4b). A combination of jet cooling and outer race cooling was used and compared to determine the overall flow rate requirements of the bearing for the given loading conditions. It was found that the overall oil consumption could be reduced by significantly reducing the jet lubrication flowrate and introducing a lower amount of flow to the outer ring, resulting in a net lower flowrate.

### 3.3.2 Rotor Shaft and Hub Design

Many factors must be considered in the design of the rotating assembly for high-speed PMSMs. As with any rotating machine, a detailed study of the stresses must be conducted to avoid exceeding the maximum allowable stresses on any component within the assembly. In addition to the component stresses, critical speeds and vibration modes with their associated natural frequencies must be predicted to avoid accelerated wear of the bearings and catastrophic failure of the rotor as the speeds in high-speed machines can approach, and sometimes exceed, the critical frequency. Manufacturability and design complexity must also be considered to avoid impractical designs. High-speed surface mounted PM motors, which mount the magnets to the outer diameter of the hub, also require additional retention of the magnets in the rotating assembly due to the high centrifugal forces that may cause the adhesive bonding of the magnets to the hub to catastrophically fail. Lastly, unbalanced electromagnetic forces as a result of manufacturing tolerances must be analyzed to assess the impact on the critical speed of the machine.

There are two common layouts for the rotor hub in radial flux machines: laminated steel hubs and integrated shafts. Laminated steel rotor hubs are made from stacked electric steel laminations that are welded, bolted, or bonded together. Laminated hubs reduce losses, leading to improved efficiency. Laminations may also be made from the same steel sheet as the stator core, meaning that the rotor laminations can help reduce waste material by using the inner portion of the steel sheet in the cutting operation for the stator core. Cooling channels may be integrated and weight can be optimized by creating cutouts in each sheet. However, this is not viable for hubs that have a variable cross-section along the axis of the motor since it leads to increased costs from additional tooling required for each cross-section design, which is especially important when considering mass production. A design with integrated cooling channels within the laminated rotor hub of an interior PM motor can be seen in [102]. Part count also increases when laminated steel hubs are used since additional components are required to retain the rotor hub to the shaft and balancing provisions need to be incorporated, for example, by using shaft-mounted balancing plates. This increases the complexity of mechanical simulations. The overall mass also increases due to strength differences in the components [116].

Integrated shafts combine the shaft and hub into a single component which improves the structural properties of the rotating assembly [117]. It offers more design freedom as the feasibility of the design features are only limited by the machinability of the hub, easily allowing for cooling channels within the hub as well as offering opportunities for topology optimization with fewer restrictions compared to laminated hubs. Additionally, laminated hub assembled onto steel shafts can lead to an increase in rotating assembly weights due to the strength differences of the shaft material and laminated steel material. Manikandan *et al.* [116] compared the strength difference of 4340HT used for an integrated shaft to the electrical steel used to make a laminated steel hub. The 4340HT steel had a yield stress of 780 MPa whereas the laminated steel stack made from 0.2 mm thick silicon steel had a maximum yield stress of 370 MPa. The rotor design used a Halbach array of magnets which negates the requirements of having a magnetic backiron, since in this type of array the magnetic field is augmented on one side and is near zero on the opposite side of the array. Electromagnetic analysis showed a minor increase in torque ripple and a minor decrease in magnet losses.

Rotor vibrations can be a significant issue in high-speed electric motors since the operating speed can approach or exceed the first natural frequency. Two types of vibrations limit the operating speed of high-speed machines: resonant vibration and self-excited vibration [117], [118]. Resonant vibration occurs when the rotation speed approaches one of the rotor's natural frequencies while self-excited vibration is a phenomenon that occurs above a certain threshold speed after which point rotation is unstable regardless of whether the rotational speed coincides with one of the rotor's natural frequencies. Internal rotor damping caused by material damping and component interfaces, such as bolting, shrink fitting, riveting, etc., contribute to the destabilizing effects that lead to self-excited vibration. Furthermore, two types of vibration modes are excited from radial loading: rigid body modes in which rotor deformation is negligible and internal damping plays no role, and flexural modes in which deformation occurs in the rotating assembly and internal damping plays a role in the dynamics. The rigid body modes are typically ignored as the natural frequencies of the rigid body modes are equal to zero and only occur if the bearing stiffness is exceedingly small [119]. The threshold limit for self-excited vibrations is defined by Borisavljevic *et al.* [120] to be:

$$\omega < \omega_{cr} \left(1 + \frac{c_n}{c_r}\right) \tag{3.22}$$

where $\omega_{cr}$ is the critical speed, and $c_n$ and $c_r$ are viscous equivalents of external and internal damping respectively.

The natural frequency of the rotor can be approximated using the following equation

[117], [121]:

$$\omega_n = a_n\sqrt{\frac{EI}{{}_{l}l^4}} \tag{3.23}$$

where $E$ is the Young's modulus, $I$ is the rotor inertia, $m_l$ is the mass per unit length, $l$ is the rotor length, and $a_n$ is dependent on the boundary conditions and is calculated using the Rayleigh method. Tenconi *et al.* [122] used a similar formula to calculate the first critical speed of a rotor shaft by considering the shaft as a supported beam:

$$n_{cr} = \frac{60}{2\pi} \cdot \sqrt{\frac{48E\pi D^4}{64l^3m}} \tag{3.24}$$

where $n_{cr}$ is the critical speed in RPM, $D$ is the shaft diameter in millimeters, and $m$ is the rotor mass. If the shaft is approximated as a clamped beam, the resulting critical speed is double the speed found using Eq. 3.24. It is suggested that an initial approximation for the critical speed should be the average of the clamped and supported critical speed values. This approximation also does not account for the rotor hub which increases the stiffness and mass of the rotating assembly, however Ede *et al.* [121] suggested that the actual natural frequencies will be lower than that calculated in Eq. 3.23 in rotating systems that use laminated steel hubs since the laminations add little axial stiffness while significantly contributing to the mass of the rotating assembly. Mechanical FEA should be conducted with careful consideration for the boundary conditions of the simulation to accurately determine modal frequencies and stresses in the rotating assembly.

In cases where the modal frequencies are too low, the following methods may be used to increase the natural frequencies of the rotating assembly [117]:

1. Reducing the rotor length.
2. Increasing the rotor diameter.
3. Reducing the bearing span.
4. Increasing the shaft wall thickness.
5. Adding a third center-bearing.

If the rotor hub length is reduced, the hub diameter must be increased to maintain the torque output of the machine. This can negatively affect the stresses within the shaft and hub since the centrifugal forces increase as a result [122]. High-speed surface mounted PM rotors will especially be negatively affected since the requirements of a retaining sleeve must be increased to retain the magnets at peak operating speeds with higher centrifugal forces. Additionally, increasing the diameter can bring the peripheral speeds close to supersonic speeds, which dramatically increases windage losses. Even without approaching supersonic peripheral speeds, the windage losses can increase significantly as a result of the quartic relationship between the rotor outer radius and the windage losses as shown in Eq. 3.3. It should also be noted that rotating systems are able to operate above the critical speeds. Such machines should pass through the critical speeds as quickly as possible to avoid excessive prolonged vibrations that could lead to damage or failure of the motor [122].

Retaining sleeve materials for high-speed surface mounted PM motors must be nonmagnetic and may produce eddy-current losses if the material is conductive [122].

Some materials studied in literature include copper, copper iron alloy, carbon fiber, stainless steel, glass fiber, inconel, and nickel cobalt alloy [117], [123], [124]. Mass, stiffness, yield stress, and conductivity are the main considerations when choosing a sleeve material. Sintered PM material has a much higher compressive stress than tensile stress [124] and can therefore withstand high compressive loading from the retaining sleeve. Li *et al.* [125] analyzed losses generated in different sleeve materials for a 117 kW 60 kRPM surface mounted PM motor. The sleeve materials were found to affect the permanent magnet losses as well. Out of the four sleeve materials tested - stainless steel, carbon fiber, copper, and copper iron alloy - the carbon fiber resulted in the lowest total losses generated in the sleeve and magnets at 119.2 W whereas copper generated almost no losses in the magnets and exhibited slightly higher sleeve losses than the total loss of the carbon sleeve rotor at 168.5 W. The stainless steel and copper iron alloy generated significantly higher total losses. Considering the difficulty in dissipating the heat within the airgap, this is highly undesirable. Carbon fiber is a common sleeve material found in high-speed surface mounted PM motors in the literature [116], [121], [123] due to its low density, high yield strength, high tangential stiffness, and high electrical resistivity. The suggested speed ranges for different sleeve materials is shown in [124]. Carbon fiber has the highest peak linear speeds of up to 500 m/s, whereas the metal sleeves only had a suggested peak linear speed of up to 250 m/s. Unlike metal sleeves, which can be shrink fitted to the rotor, carbon sleeves must be wound directly onto the rotor, which introduces complications and higher costs as a result of inevitable scrap parts, or wound on a mandrel and pressed onto the rotor. Pressed sleeves require very tight tolerances to ensure that the sleeve is not overstressed during operation or during the fitting process.

Shaft seals are the final mechanical rotor components required to prevent contamination, mixing of different fluids within the motor, or leakage of fluid between two regions of the motor depending on the rotor cooling, bearing lubrication strategies, and level of contamination. Grease lubricated bearings may come with elastomer-type lip seals, which produce friction losses as a result of contact between the seal and inner raceway, or metal non-contact shields, which produce no losses and are required for high-speed sealed bearings. Oil lubricated bearings and grease lubricated bearings without integrated seals require external seals to contain grease in the case of grease lubricated bearings, and to prevent oil leakage or external contaminants from entering the bearing cavity in the case of oil lubricated bearings. Non contact seals, such as labyrinth seals, baffle seals, and gap seals, are able to protect the bearing cavity from light contamination and low amounts of splashing liquids which makes them suitable for oil-air mist and grease lubricated bearings. For oil jet lubrication and heavy contamination, a contact seal is required to seal the bearing cavity. Contact seals are also required with many liquid rotor cooling solutions that do not expose the motor cavity to the coolant, such as variations of hollow shaft cooling which were discussed earlier in the chapter.

## 3.4 Chapter Summary

This chapter presents a high level overview of mechanical and thermal aspects of rotor designs in high-speed radial flux motors. Main sources of losses are first highlighted within the stator and rotor. Basic equations are provided to estimate electromagnetic and mechanical losses for each loss generating component; however, it is important to note that these equations generally cannot accurately determine the loss distribution, but they rather help identify and asses the effects of factors that affect the losses through the proportionalities in the equations. For electromagnetic losses, electromagnetic FEA is required whereas windage losses can be determined using correlations within the airgap. CFD is usually required for the remaining rotor surfaces depending on the rotor geometry if such a figure is desired. Bearing losses and contact seal losses must be provided by suppliers due to the number of factors present in the generation of losses in these components. The loss distribution is crucial to the design of rotor thermal management solutions, a number of which are described in this chapter. The main trend that emerges from the literature review of liquid rotor cooling designs is the prevalent use of hollow shaft cooling and hybrid cooling variations compared to spray cooling. Bearing lubrication is discussed, highlighting oil-air mist and jet lubrication which are the most common lubrication and cooling methods for high-speed bearings. Other passive methodologies are presented, but oil jet lubrication is found to be the simplest, most practical, and most reliable lubrication and cooling solution for high-speed bearings. Due to the complexity of multiphase simulation to analyze the oil-air flow within the bearing cavity, it is best to determine thermal and lubrication performance experimentally. Lastly, a high level overview of the rotor mechanical design is provided, with critical speeds and stresses identified as the two main concerns for rotating assemblies. Two hub and shaft layouts are introduced along with additional guidelines to maximize the stiffness of the rotating assembly, thereby increasing the critical speeds to prevent these speeds from falling within the operating speed range of the rotor. Retaining sleeve materials for surface mounted PMs were presented with the conclusion that carbon fiber sleeves are most appropriate for high-speed machines in cases where higher costs and tight tolerances are not an issue due to its high tangential stiffness, high strength, high maximum operating speed, and low losses. The information presented in this chapter provides useful context for the design of the rotor within the proposed motor presented in the next chapter.

# Chapter 4

# Proposed High-Speed Power Dense Radial Flux Surface-Mounted PM Motor Design

This chapter presents a design overview of the electric motor proposed for this thesis. While the author did not contribute to the electromagnetic design of the motor, a high-level overview is discussed to provide a basis for the mechanical design of the stator and rotating assemblies while providing context for the thermal analysis of the rotor described in the following chapter. Following the electromagnetic design, the mechanical design of the stator assembly is discussed with emphasis on the author's contributions to the components within the stator assembly. This section explores the use of additive manufacturing for the motor housing and end plate to reduce weight while reducing part count, which in turn improves the reliability due to the reduction in points of failure within the design. Furthermore, the discussion covers the shrink fitting process of the stator within the housing along with the stator potting process and tooling design. The thermal management strategy for the rotor is first introduced in the rotating assembly section as a precursor to the thermal analysis of the rotor covered in the following chapter. Due to the complexities of the internal shaft design, billet machining is not viable. Therefore, alternative manufacturing methods and their respective challenges are presented. Since the design of the shaft is relatively complex, only a preliminary design is presented with the understanding that mechanical FEA is required to finalize the design.

The electromagnetic design is credit to Giorgio Pietrini, Mohamed Abdelmagid, and Srikanth Pillai, and the stator thermal management design is credit to Samantha Jones Jackson and Dikhsita Choudhary. The mechanical FEA conducted for the housing and end plate is credited to Akshay Manikandan.

The terms "A-side" and "B-side" are used to denote each half of the motor in the axial direction as shown in Fig. 4.1. These terms correspond to the drive end and non-drive end, respectively. The A-side of the motor contains the spline and mounting surface of the housing to mate with external components. The B-side of the motor contains the end plate and fluid connections between the stator and rotor, which are described later in the chapter.

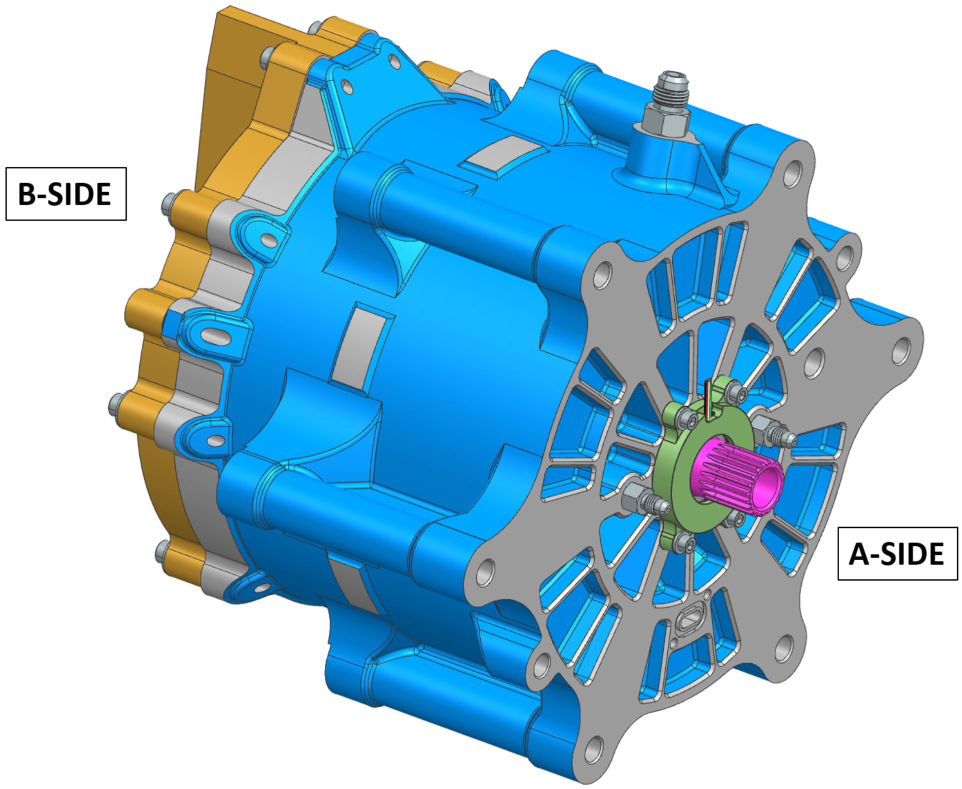


Figure 4.1: Proposed motor highlighting the A-side and B-side of the motor.

## 4.1 Electromagnetic Design

The motor proposed in this thesis is an inner rotor radial flux surface mounted PM motor. The inner rotor configuration helps mitigate rotor eddy current losses with the implementation of distributed windings. The size of the motor, based on the outer diameter and stack length of the stator, was provided as a minimum requirement for the motor design. The number of poles and slots in the stator were chosen to minimize torque ripple and maximize the power factor while keeping the fundamental frequency within an acceptable range. The stator backiron thickness and tooth length, which determine the of the stator, were optimized to mitigate saturation of the non-oriented NO20 silicon steel laminations. While cobalt steel grades offer higher levels of saturation compared to silicon steel, the material cost of cobalt steels is significantly higher. The slot area, the final geometric parameter of the stator, was designed to achieve a 50% slot fill factor, a figure considered appropriate for hand-wound stators.

The number of turns, current, and magnet thickness have been optimized to achieve 73Nm of torque. The maximum power and operating speed of the motor are 150 kW and 20 kRPM.

A 4-segment Halbach array configuration is adopted for each pole of the magnets due to its ability to enhance the field distribution. Additionally, a Halbach array configuration diminishes the necessity for a magnetic laminated steel rotor hub. Electromagnetic FEA analysis was conducted on the rotor to compare the performance using a 6.8 mm backiron thickness made from non-oriented silicon steel and AISI 4340 in conjunction with a Halbach array. The comparison showed little to no difference in the power, torque, phase voltage, magnet losses, and total machine losses, however the use of AISI 4340 resulted in a slight increase in the torque ripple from 4.7% to 6.3%. It should be noted that the backiron thickness may be further reduced as a result of the Halbach array configuration.

## 4.2 Stator Assembly Design

The stator assembly design consists of all the non-rotating components within the motor. The main components in the stator assembly include the housing, end plate, stator, windings, and potting. Fig. 4.2 shows the components within the stator assembly with the exception of the potting around the stator windings. In this section, the stator cooling design is introduced and the manufacturing of the housing, end plate is discussed. The assembly of the stator assembly is also provided, focusing on the stator shrink fitting and winding potting processes along with the associated tooling used for the potting.

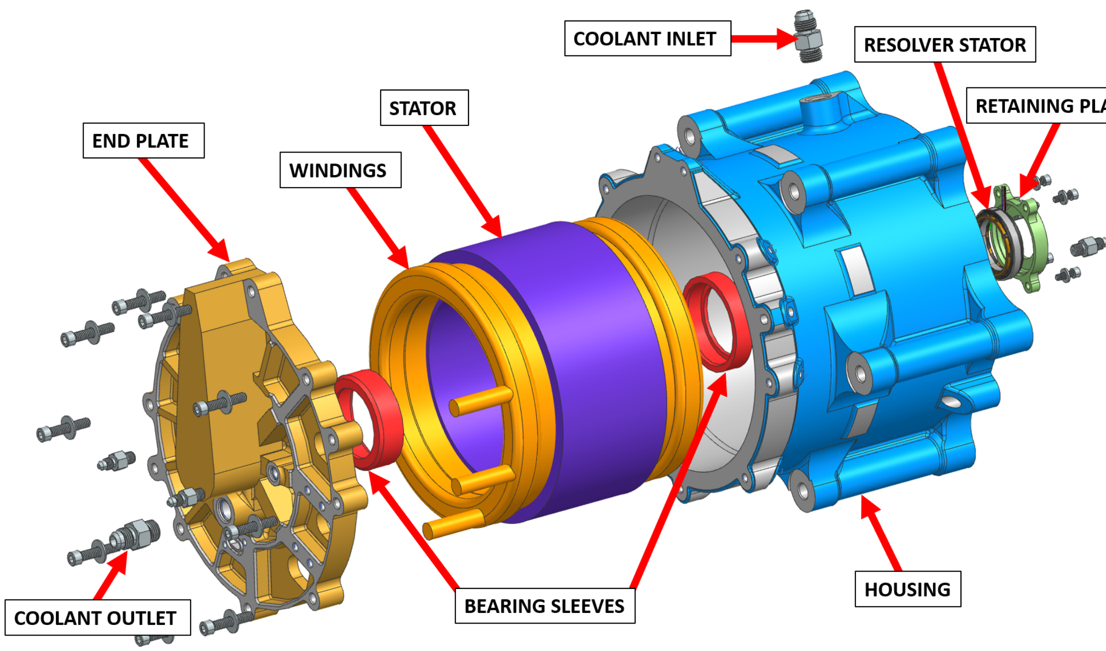


Figure 4.2: Exploded view of the stator assembly.

### 4.2.1 Housing and End Plate Design and Manufacturing

The motor housing uses an internal snake-line cooling jacket design for the stator and winding thermal management as shown in Fig. 4.3. The path of the coolant extends along the axial length of the windings, encompassing the windings along its

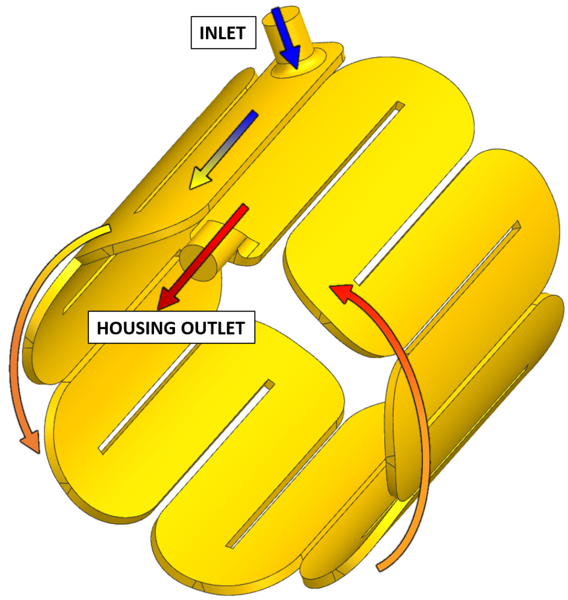


Figure 4.3: Representation of the coolant jacket design within the housing.

path throughout the circumference of the motor. The coolant path for the stator terminates on the B-side mounting flange on the housing where it is directed to the rotating assembly. The end plate on the A-side of the motor is integrated into the housing to improve the overall stiffness of the stator assembly. Motors using a cooling jacket design are normally conventionally machined in two parts: an inner sleeve and outer housing. The coolant path is machined into the outer diameter of the sleeve along with o-ring grooves at each end. When the sleeve is fitted into the outer housing, which is the main structural component in the stator assembly, the coolant is fully contained between the inner and outer sleeve of the assembly.

The proposed motor uses a housing made with Additive Manufacturing (AM) with the cooling channels integrated into the housing. AM is used to reduce the housing structure to a single component, allowing for a lower overall weight when compared to a multi-part design of a similar size due to the increase in stiffness. It should be noted that the A-side integrated end plate does not contain any features that necessitate AM apart from two bearing lubrication channels, however the added benefit of the overall stiffness outweighed the assumed additional manufacturing cost and material usage in AM as opposed to machining a separate end plate. $AlSi_{10}Mg$ was the material of choice for the housing as it is a common, lightweight, well understood AM alloy similar to aluminum 6061 T6. After manufacturing parts using Laser Powder Bed Fusion (L-PBF), there is a high degree of anisotropy in the mechanical, thermal, and electrical properties, which is related to the build direction inside the L-PBF printer. To address this anisotropy, the aluminum alloy is first undergoes Hot Isostatic Pressing (HIP) before being heat treated as per the T6 heat treatment specification outlined by EOS [126], or similar, to relieve residual stresses and improve the material density which reduces the anisotropy in the component's mechanical, thermal, and electrical properties. Some of the mechanical properties of HIP and heat treated $AlSi_{10}Mg$, and aluminum 6061-T6 can be compared using Table 4.1.

Table 4.1: Material properties of HIP and heat treated $AlSi_{10}Mg$ and Aluminum 6061-T6. Note that the $AlSi_{10}Mg$ exhibits some level of anisotropy after HIP and heat treating, hence the display of properties in the horizontal and vertical directions relative to the build direction of the part.

| | **$AlSi_{10}Mg$** | | **Al6061-T6** |
|---|---|---|---|
| | Vertical (Z) | Horizontal (X/Y) | - |
| Yield Strength (MPa) | 250 | 260 | 276 |
| Elongation at Break (%) | 11 | 11 | 17 |
| Thermal Conductivity (W/mK) | 165 | 155 | 167 |
| Coefficient of Thermal Expansion ($10^{-6} \cdot 1/K$) | 22 | | 23.6 |

Design considerations for L-PBF AM are similar to many other AM methods in that

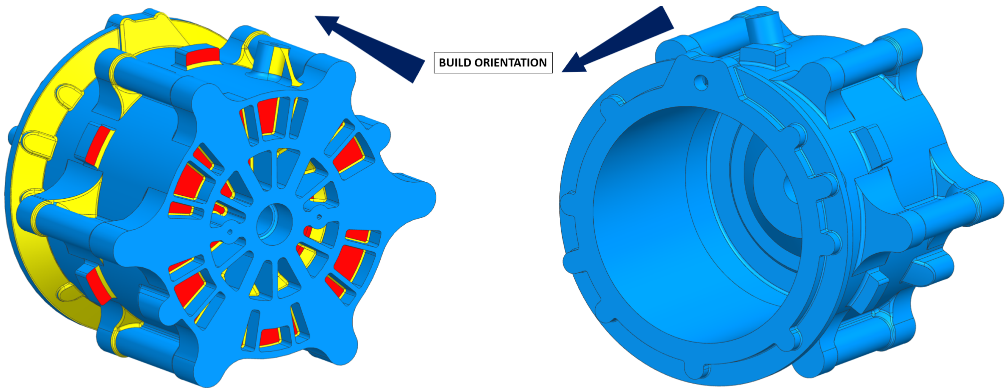


(a) (b)

Figure 4.4: As-printed housing viewed from the (a) A-side and (b) B-side highlighting overhanging surfaces that require support material in red and surfaces that do not require support material in yellow.

overhanging surfaces require support structures up to a prescribed angle relative to the build plate of the printer since the aluminum powder, also known as the feedstock material, underneath overhanging surfaces is typically unable to support large areas of newly sintered metal on top of nothing but underlying unsintered feedstock material. To prevent the use of support material, which utilizes more feedstock material, requires additional post processing, and leaves a lower-quality surface finish, overhanging surfaces must be made at an angle larger than roughly 35° to the build plate with larger angles providing better surface finishes on the overhanging surfaces. This angle largely depends on the printing parameters and feedstock material. Support material is used within the pockets between the ribs of the integrated end plate when printing the housing due to the build orientation shown in Fig. 4.4. In addition to the pocket surfaces, tabs on the side of the housing also use support material as indicated by the red surfaces in Fig. 4.4a). These tabs are present for clamping during machining operations completed after the printing process and are removed in a separate machining process after potting, therefore the presence of support material is not a concern. Support material removal is limited to these areas with all other overhanging surfaces modelled at a minimum of 35° to the build plate, which are indicated in yellow in Fig. 4.4a), to prevent the unnecessary use of support material elsewhere on the external surfaces of the housing.

There are two concerns with printing the cooling channels within the housing: support material and powder removal. Since the L-PBF process sinters the cross section of the part from a thin layer of deposited powder, the final component leaves unsintered powder within the channel. A small hole is placed at the location of the inlet port on the housing for powder removal. The outlet of the housing on the B-side flange is also used to evacuate trapped powder within the channel. Powder evacuation was also successfully tested on a preliminary simplified 1:2 scale model of the housing printed using L-PBF. Support material is easily avoided within the cooling circuit of the housing by using a 45° angle between the overhanging surfaces and the build plate. Since the housing requires machining after printing, excess material was added in the locations that were to be machined.

The B-side end plate contains an integrated channel that directs the coolant from the housing to the rotor which necessitates AM. This significantly reduces part count since the number of parts, including seals and bolts, which are necessary to connect the stator coolant channel to the rotor, are reduced to a single AM part. The same design principles for AM described above were used for the design of the B-side end plate. In a production setting, the end plate design can be slightly modified to use casting instead of AM to reduce part costs under higher production volumes. The print orientation for the end plate is shown in Fig. 4.6. It should be noted that the geometry surrounding the integrated channel is hidden.

The printed housing resembles a cast component and hence is treated in a similar manner with regards to post-machining of the critical features. These features are indicated by the gray surfaces in Fig. 4.5. The main critical features are the stator bore, bearing bore, motor mounting flange on the A-side of the housing, and B-side end plate mounting flange. Features to locate the resolver stator and contact seal are machined along with the bolt holes, coolant inlet port, bearing oil drain, and bearing oil channel inlet and outlet holes. Similarly, the B-side end plate has features machined for the bolting holes, bearing bore, contact seal diameter, inlet tube mating diameter, the mating surface to the housing and potting, bearing lubrication inlet and outlet ports, bearing oil drain, and the coolant outlet port as shown in Fig. 4.6.

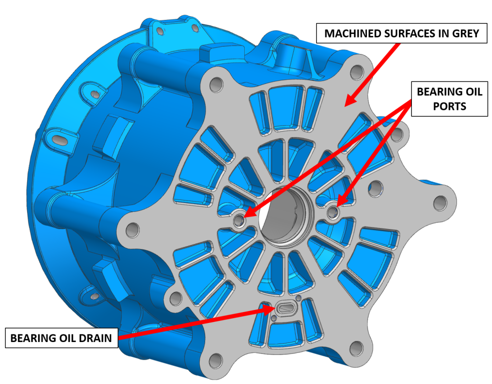


(a)

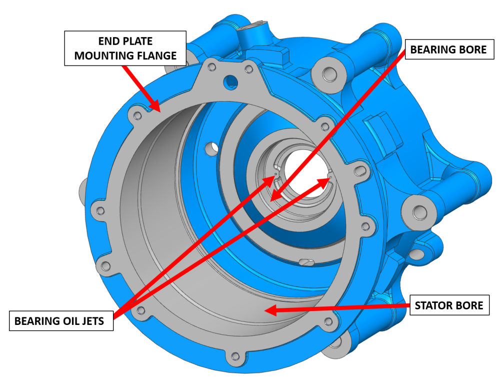


(b)

Figure 4.5: As-machined housing viewed from the (a) A-side and (b) B-side

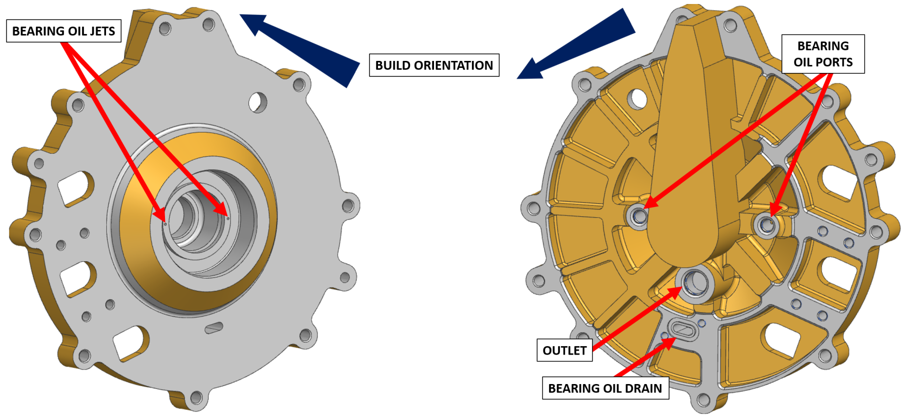


(a) (b)

Figure 4.6: As-machined end plate viewed from the (a) inside facing surfaces and (b) outside facing surfaces.

### 4.2.2 Stator Shrink Fitting

The stator is connected to the housing using a shrink fit. The housing is heated up to create a clearance fit between the housing and stator before quickly inserting the stator and allowing the housing to cool and create an interference fit. The minimum shrink fit specified must prevent the stator from slipping under the maximum rated torque of the motor. Therefore tolerances need to be determined to maintain a minimum press fit and avoid excessive stresses under minimum and maximum material conditions throughout the operating temperature range. Conventional press fit equations are used to calculate the stresses, required interferences, etc. for the shrink fit. A number of geometric and material input parameters required for the calculations are shown in Table 4.2.

Table 4.2: Input parameters for the calculation of the stator-housing shrink fit.

| **Material Properties** | | |
|---|---|---|
| Stator Elastic Modulus (MPa) | $E_i$ | 190,000 |
| Housing Elastic Modulus (MPa) | $E_o$ | 70,000 |
| Stator Poisson Ratio (-) | $\nu_i$ | 0.28 |
| Housing Poisson Radio (-) | $\nu_o$ | 0.30 |
| Stator CTE (1/°C) | $\alpha_i$ | 1.2 x $10^{-5}$ |
| Housing CTE (1/°C) | $\alpha_o$ | 2.2 x $10^{-5}$ |

| **Physical Conditions** | | |
|---|---|---|
| Applied Torque (Nm) | $T_{app}$ | 74 |
| Max. Operating Temperature (°C) | $T_{max}$ | 93 |
| Min. Operating Temperature (°C) | $T_{min}$ | 25 |
| Interface Coefficient of Friction (-) | $\mu_f$ | 0.15 |

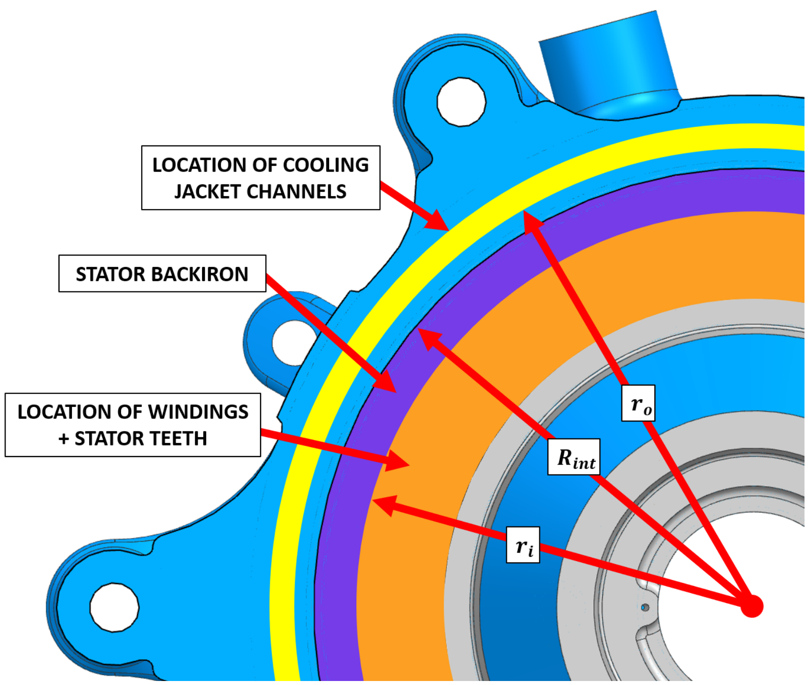


Figure 4.7: Cross section of the stator assembly highlighting the radii used in the shrink fit calculations.

The minimum required interface contact pressure is calculated using the applied torque $T_{app}$ in the following equation:

$$T_{app} = 2\pi\mu_f p_{int} L_{int} R_{int} \tag{4.1}$$

where $\mu_f$ is the friction coefficient at the interface, $L_{int}$ is the interface length, which is the stator length in this instance, $R_{int}$ is the interface radius, which is the stator outer radius and housing inner radius shown in Fig. 4.7, and $p_{int}$ is the interface pressure. The minimum radial interference between the two components can be found using the equation below:

$$p_{int} = \frac{\delta_{int}}{R_{int}\left[\frac{1}{E_o}\left(\frac{r_o^2+R_{int}^2}{r_o^2-R_{int}^2}+\nu_o\right)+\frac{1}{E_i}\left(\frac{R_{int}^2+r_i^2}{R_{int}^2-r_i^2}-\nu_i\right)\right]} \tag{4.2}$$

where $r_i$ and $r_o$ are the inner cylinder inner radius and outer cylinder outer radius shown in Fig. 4.7, and $\delta_{int}$ is the radial interference. The interference required from the stator and housing, respectively, are given by the following equations:

$$\delta_{int,o} = \frac{p_{int}R_{int}}{E_o}\left(\frac{r_o^2+R_{int}^2}{r_o^2-R_{int}^2}+\nu_o\right) \tag{4.3}$$

$$\delta_{int,i} = \frac{p_{int}R_{int}}{E_i}\left(\frac{R_{int}^2+r_i^2}{R_{int}^2-r_i^2}-\nu_i\right) \tag{4.4}$$

Due to the larger Coefficient of Thermal Expansion (CTE) of the aluminum housing compared to the steel stator, the minimum interface pressure and radial interference must be maintained at the maximum operating temperature. Since the maximum temperature is the limiting condition, thermal expansion is considered to determine the stresses in the stator and housing at the minimum operating temperature. The following equation is used to determine the unpressed radii of both components:

$$R_{int,i/o} = (R_{int} \pm \delta_{i/o}) + (R_{int} \pm \delta_{i/o})(\alpha_{i/o}(T_{min} - T_{max})) \tag{4.5}$$

where where $i/o$ in $R_{int,i/o}$, $\delta_{i/o}$, and $\alpha_{i/o}$ denote the inner cylinder and outer cylinder, which are the stator and housing in this case. The radial interference at the minimum temperature, given by the difference $R_{int,o} - R_{int,i}$, is used to calculate the interface pressure using Eq. 4.2, which is then used to calculate the stresses within the components. The tangential stresses on both components and Von Mises stress (denoted as "effective stress") on the housing are calculated using the following equations:

$$\sigma_{t,i} = -p_{int} \left( \frac{R_{int}^2 + r_i^2}{R_{int}^2 - r_i^2} \right) \tag{4.6}$$

$$\sigma_{t,o} = p_{int} \left( \frac{R_{int}^2 + r_o^2}{R_{int}^2 - r_o^2} \right) \tag{4.7}$$

$$\sigma_o = \frac{1}{\sqrt{2}}((\sigma_{t,o} + p_{int})^2 + p_{int}^2 + \sigma_{t,o}^2)^{0.5} \tag{4.8}$$

where $\sigma_{t,i}$ is the tangential stress on the inner cylinder, $\sigma_{t,o}$ is the tangential stress on the outer cylinder, and $\sigma_o$ is the effective stress on the outer cylinder.

Using Eq. 4.2 to Eq. 4.8, the calculated minimum radial interference, stator tangential stress, and housing effective stress are shown in Table 4.3.

Table 4.3: Minimum stator-housing shrink fit interference and stresses at minimum and maximum temperatures.

| | | |
|---|---|---|
| Minimum Required Radial Interference (mm) | $\delta_{int}$ | 0.00339 |
| Stator Tangential Stress @ Max. Temperature (MPa) | $\sigma_{t,i,min}$ | -1.13 |
| Stator Tangential Stress @ Min. Temperature (MPa) | $\sigma_{t,i,max}$ | -21.97 |
| Housing Effective Stress @ Max. Temperature (MPa) | $\sigma_{o,min}$ | 2.20 |
| Housing Effective Stress @ Min. Temperature (MPa) | $\sigma_{o,max}$ | 42.80 |

The minimum required radial interference is used as a reference value when iterating through tolerances for the stator Outer Diameter (OD) and housing Inner Diameter (ID). Radial interferences, stator tangential stresses, and housing effective stresses were calculated under the four following conditions:

- Maximum material condition (MMC) & minimum operating temperature (LOT)
- MMC & maximum operating temperature (MOT)
- Minimum material condition (LMC) & LOT
- LMC & MOT

The two limiting conditions are MMC & LOT, and LMC & MOT which result in the highest and lowest radial interference, respectively. Component stresses should be well within the yield strength at the highest radial interference while maintaining the minimum fit requirements at the lowest radial interference considering the tolerances and thermal expansion. A minimum tolerance range of 0.001" (or 0,025 mm) and 0.002" (or 0,051 mm) are implied for the housing bore diameter and stator OD respectively for manufacturability. The tolerances, resulting radial interferences, and component stresses are shown in Table 4.4 and Table 4.5.

Table 4.4: Stator OD and housing stator bore diameter tolerances applied to the nominal interface diameter $2R_{int}$.

| | Inches | Millimeters |
|---|---|---|
| Stator Outer Diameter | $^{+0.001}_{-0.001}$ | $^{+0,025}_{-0,025}$ |
| Housing Bore Diameter | $^{-0.008}_{-0.009}$ | $^{-0,203}_{-0,229}$ |

Table 4.5: Stator-housing interferences and stresses under the limiting conditions.

| | | MMC & LOT | LMC & MOT |
|---|---|---|---|
| Radial Interference (mm) | $\delta_{int}$ | 0.127 | 0.027 |
| Interface Contact Pressure (MPa) | $p_{int}$ | 4.26 | 0.89 |
| Stator Tangential Stress (MPa) | $\sigma_{t,i}$ | -42.41 | -8.89 |
| Housing Tangential Stress (MPa) | $\sigma_{t,o}$ | 80.38 | 16.85 |
| Housing Effective Stress (MPa) | $\sigma_o$ | 82.59 | 17.31 |

Note that some of the input parameters from Table 4.2 may vary from the tabulated values. The interface coefficient of friction depends heavily on the surface finish of the two mating components and can be hard to quantify. Additionally, the interface length may be shorter in reality due to the presence of glue between the laminations to bond the steel sheets, which does not contribute to the strength of the joint. Lastly, the outer radius of the housing is not accurate to the true geometry due to the presence of the cooling channels within the cross section, as shown in Fig. 4.7, which reduces the cross sectional area of the housing. The interface coefficient of friction only affects the minimum fit requirements in Table 4.3 whereas the interface length and housing outer radius affect the values in the aforementioned table as well as the calculation of the stresses when considering the tolerance of the components in Table 4.4 and Table 4.5. The friction coefficient was varied and it was determined that a value of 0.02 for the friction coefficient resulted in a near identical minimum required radial interference to the LMC & MOT condition, the loosest possible fit considering tolerances. This value is extremely low and unrealistic, therefore resolving the issue in the variation of the friction coefficient. Changing the interface length and housing outer radius to account for the fill factor in the lamination stack and variation in the housing cross section, respectively, did not result in significant variations in the values shown in Table 4.5.

Using Eq. 4.1 and the interface pressure from the LMC & MOT condition, the minimum holding torque was calculated to be 581 Nm. The resulting safety factors of the press-fit are 7.85 for the holding torque and 3.05 for the maximum possible housing effective stress.

### 4.2.3 Stator Potting

The stator and windings are potted in a two-component epoxy resin to provide a thermal connection between the windings and the coolant flowing through the housing by filling any pores between the wires and stator. Stator potting is a superior stator impregnation process when compared to other processes like roll dipping and trickle impregnation for motors using a cooling jacket design since the potting epoxy provides a direct thermal connection between the end windings and the coolant rather than dissipating the heat through the stator and to the air within the motor cavity. If a more direct stator cooling method was used, such as spray cooling or flood cooling, then varnishing, roll dipping, and other similar processes are superior from a thermal point of view since the amount of material covering the end winding is minimized, reducing the thermal resistance between the windings and the coolant.

The stator potting for the proposed motor is designed in collaboration with Demak S.r.l. The two-component epoxy resin used for the potting process provides high operating temperatures, high flowability, low temperature curing, relatively high thermal conductivity (compared to other potting epoxies with similar properties), and excellent crack resistance. The properties of the potting material provided by Demak are shown in Table 4.6.

Table 4.6: Properties of the potting epoxy resin provided by Demak S.r.l. [127].

| | |
|---|---|
| Curing | Room Temperature |
| Density | 2.60 g/cc |
| Epoxy + Hardener Viscosity | 2200 cps |
| Thermal Conductivity | 1.6 W/mK |
| Glass Transition Temperature | 90-100°C |
| Max Operating Temperature | 200°C |

Potting materials with thermal conductivities more than 2 times higher than the one used in the proposed motor are available on the market, however the viscosities of these potting epoxies are far higher, significantly increasing the potential for voids forming in the potting, reducing its ability to dissipate heat. These higher conductivity potting epoxies should be explored in the future to further improve the stator thermal management.

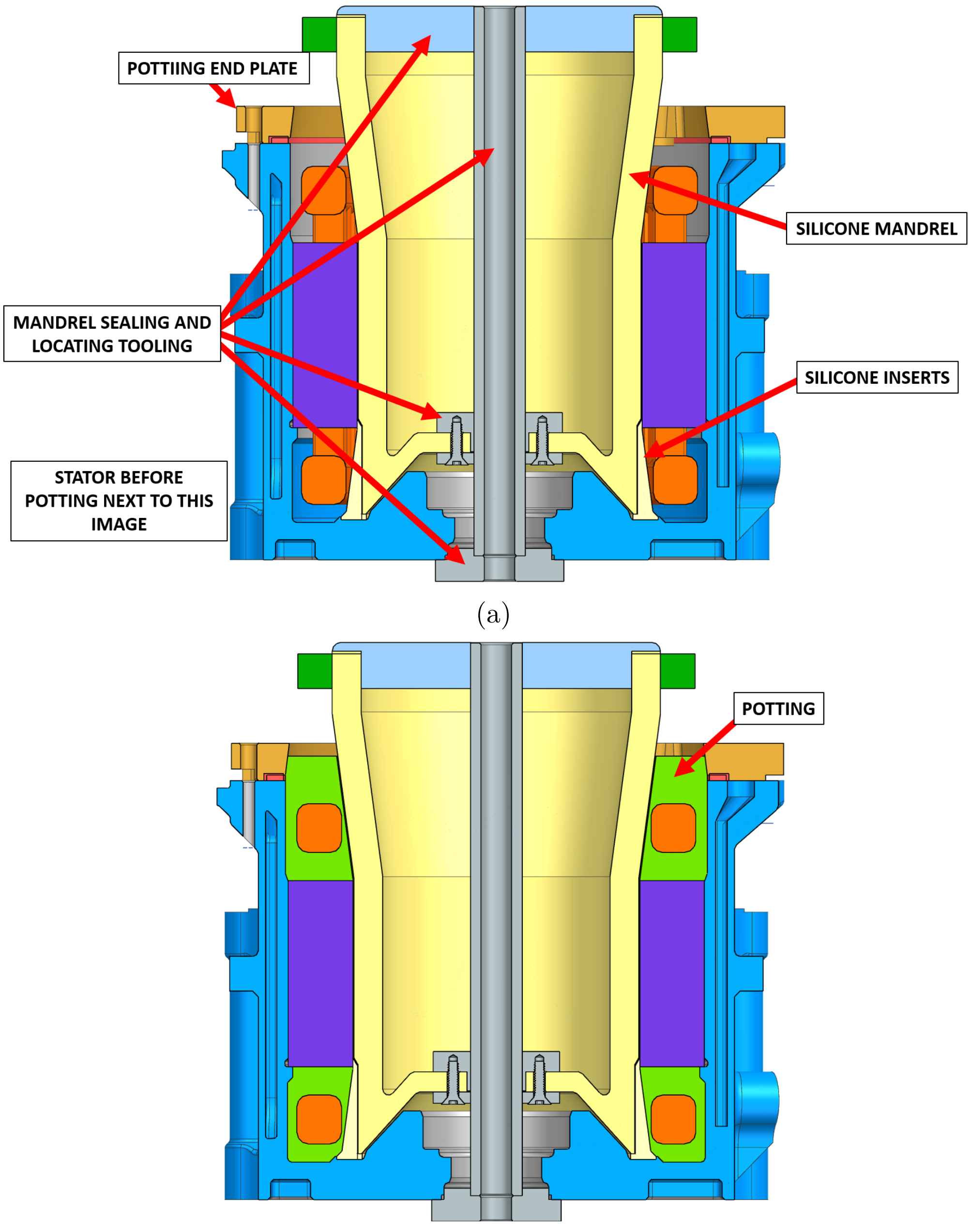


Figure 4.8: Stator assembly cross-section (a) before potting, highlighting the potting tooling, and (b) after potting. The tooling design is patented by Demak S.r.l [128].

The potting tooling, shown in Fig. 4.8a) and Fig. 4.8b), mainly consists of a silicone mandrel and a stand-in end plate on the B-side of the housing. The potting epoxy is filled from a port on the A-side of the housing. A meniscus forms at the top of the epoxy once it has reached the desired level. To maximize the heat dissipation of the end windings, the epoxy should maintain a good thermal connection with the end plates on both sides of the stator assembly. Since the A-side end plate is integrated into the housing, the best possible thermal contact is achieved, however, filling the stator with epoxy below the level of the B-side end plate mounting flange results in a poor or non-existent thermal connection due to the meniscus. Therefore, the stator is overfilled with epoxy and machined down in a later machining process. The stand-in end plate mounted to the B-side of the housing during the potting process ensures that the epoxy can be filled past the flange on the housing. It also serves a secondary purpose of locating the termination wires which is important for final assembly.

The filling process and tooling design, with the exception of the stand-in end plate, is patented by Demak S.r.l [128]. The silicone mandrel is a hollow molded part which connects to a sealing plate containing an air-supply fitting used to pressurize the mandrel before beginning the filling process. Pressurizing the mandrel ensures that the OD of the mandrel presses against the ID of the stator, preventing any epoxy from leaking into the air gap and curing afterwards. The inner face of the potting within the end winding regions is angled outwards towards the ends of the motor to allow bearing oil to drain towards the end plates. On the B-side of the motor, this shape is achieved by drafting the corresponding face on the mandrel. However, on the A-side of the housing, the mandrel cannot be drafted otherwise it will not be possible to insert it through the ID of the stator. Three silicone pieces are inserted into the A-side of the housing, filling the drafted volume to create the corresponding angled surface in the potting on the A-side. These inserts are highlighted in Fig. 4.8a).

During the initial machining of the housing, the B-side mounting flange is not machined to the final dimension. Instead, some extra material is left to be machined after the potting process which is shown in Fig. 4.9a). To maintain the best possible thermal contact between the epoxy and end plate, the flange and epoxy are machined together to the final housing height as shown in Fig. 4.9b). During final assembly, boron nitride thermal paste is used to fill any small air gaps between the B-side end plate and the epoxy.

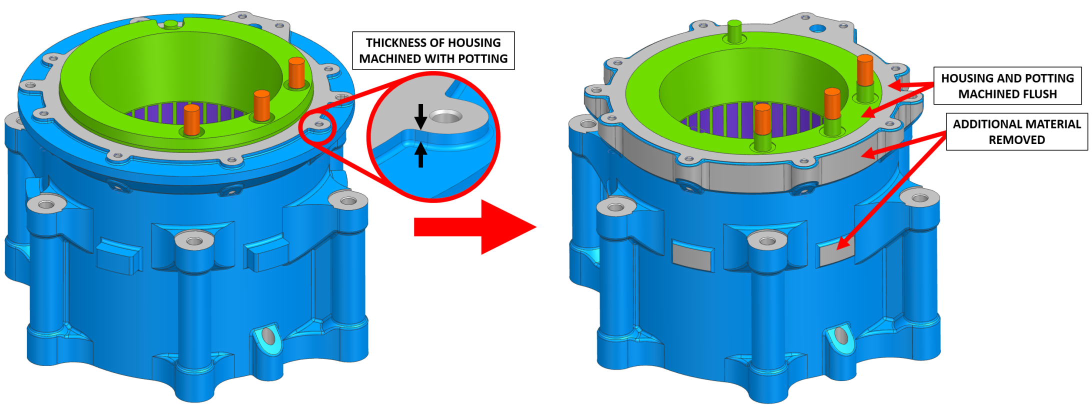


(a) (b)

Figure 4.9: Potted stator and housing (a) before machining the epoxy and housing and (b) after machining the potting and housing.

## 4.3 Rotating Assembly Design

The main components in the rotating assembly are the integrated shaft, magnets arranged in a Halbach configuration glued to the surface of the rotor, carbon fiber retaining sleeve, and bearings. These main components, along with the bearing oil baffle, wave spring, and inlet tube, are shown in Fig 4.10. It should be noted that the inlet tube is part of the stator assembly as it is pressed into the end plate, however since it is an integral component in the rotor cooling design, the inlet tube is introduced and discussed in this section. Since the magnets are configured in a Halbach array, the motor can use an integrated shaft design without seeing an increase in losses. As mentioned in section 3.3.2, combining the hub and shaft improves the axial stiffness, allowing for a lower overall shaft and hub weight when compared to a traditional structure which uses a laminated steel hub on a solid steel shaft. Since the integrated shaft design is relatively complex, FEA analysis is required to accurately determine the mechanical performance of the design. The discussions surrounding the rotor design revolve around manufacturability, and general mechanical and thermal considerations.

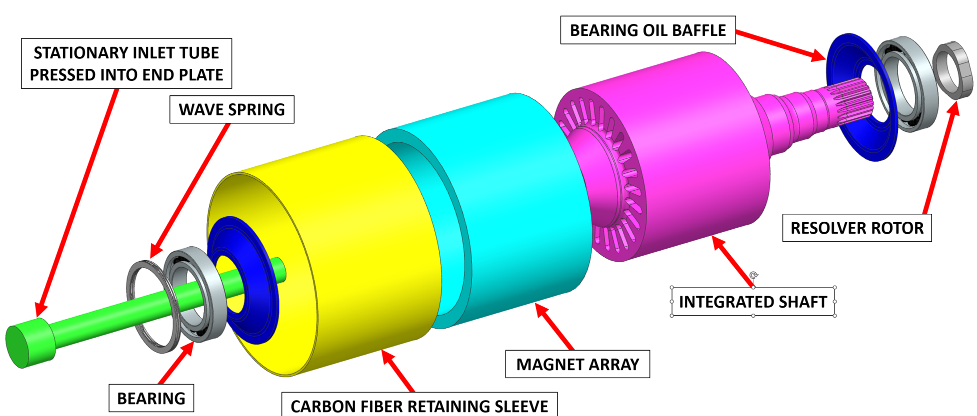


Figure 4.10: Exploded view of the rotating assembly.

### 4.3.1 Rotor Cooling Design

The rotor cooling uses a recirculating hollow shaft cooling design as described by [68], [129] and is integrated with the stator cooling loop as shown in Fig. 3.2b). The coolant path in the proposed motor is shown in Fig. 4.11. It should be noted that the channels within the housing and end plate are hidden. The coolant specified for the stator cooling is a 50/50 mixture of Water and Ethylene Glycol (WEG 50/50) by volume. WEG 50/50 is a commonly used coolant for many applications and is effective at operating at temperatures far below the freezing point of water, making it highly versatile for traction applications. Due to the versatility of the coolant coupled with the low viscosity, which limits pressure drop and fluid friction losses, the coolant was unchanged from the original specification.

Coolant exits the housing from a port on the B-side end plate flange, passing through the B-side end plate from the integrated channel. The fluid then enters the stationary inlet tube to pass fluid to the inner rotating hollow shaft at the A-side of the shaft cavity. The coolant flows through towards the outlet of the shaft which is the annular gap between the shaft and inlet tube at the B-side of the motor. The fluid enters a small chamber where it then flows through an outlet port within the end plate. The coolant within the outlet chamber in the end plate is separated from the bearing chamber on the inside of the end plate using a low friction, high-speed contact shaft seal to prevent mixing the rotor coolant and bearing lubricating oil while minimizing generated losses. The OD of the shaft at the location of the seal varies between 17 mm to 29 mm. This variation is due to the rotor cooling design optimization described in the following chapter. A large benefit of the recirculating hollow shaft design is the minimal use of seals, and therefore minimum generated losses from the seals, with only a single shaft seal required to seal the cooling loop compared to two seals required for a conventional hollow shaft solution with one seal at each end of the shaft. However, an additional shaft seal is used to seal the A-side bearing from external contamination and preventing oil leakage as non-contact seals are inadequate for preventing any leakage from an oil jet lubricated bearing. The shaft seals used in the proposed motor utilizes a proprietary low-friction material capable of achieving very high surface speeds up to 60 m/s with low generated losses [130]. The maximum surface speeds at both sealing surfaces is only 30.3 m/s, well under the maximum rated surface speed, however these speeds still exceed the capabilities of most off-the-shelf shaft seals.

It should be noted that a hybrid cooling solution, as seen in [85], [92]–[94], [102] and in Fig. 3.2e), was considered. In this design, fluid axially flows into the hollow shaft and through a series of radial channels at the axial midplane of the rotor that would carry the fluid to a set of axial channels adjacent to the magnets. The fluid would then move towards nozzles at the ends of the rotor hub where it exits the hub and sprays onto the end windings. This cooling solution has better potential to provide effective cooling for the magnets and end windings, however the cooling design requires a significant redesign of the stator to use a different impregnation process, such as roll dipping, to minimize the thickness of material between the windings and coolant, therefore minimizing the thermal resistance. Ideally, coolant should also spray onto the OD of the end windings from the housing to avoid hotspots in the locations that

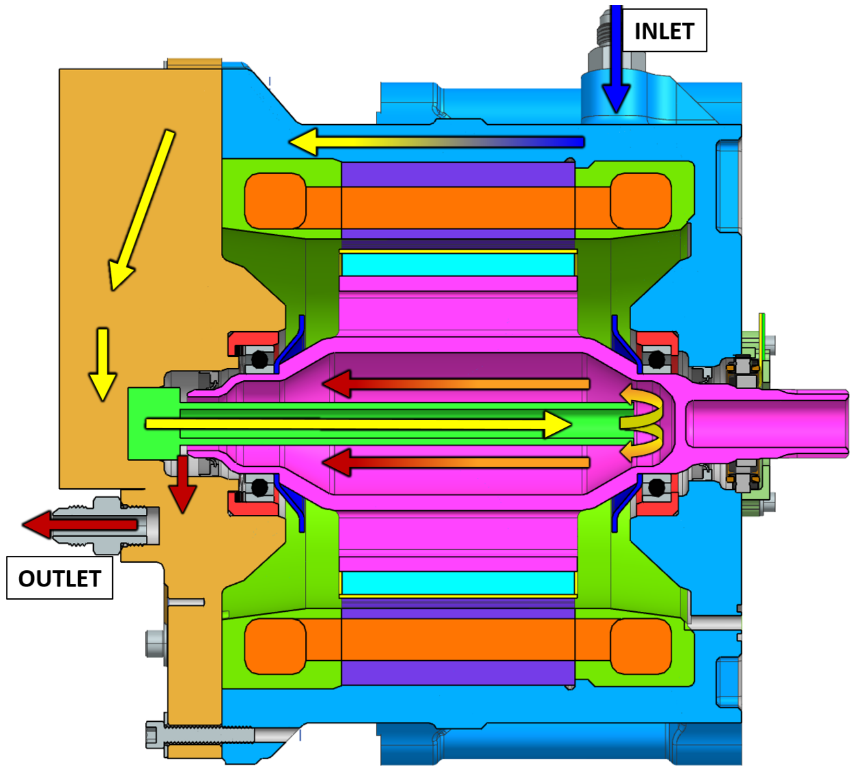


Figure 4.11: Cross section of the full motor highlighting the rotor cooling loop. Arrows indicate the coolant path from the inlet in the cooling jacket to the outlet in the B-side end plate. Coolant channels within the housing and end plate are hidden.

are not exposed to the rotor coolant spray. Analysis of this motor cooling strategy requires highly complex, time consuming, and troublesome multiphase simulations. The inclusion of the stator and motor cavity along with the rotor in the domain leads to a very large simulation, leading to long run times. Initial simulations were attempted, however the design was abandoned due to time limitations. Such a design is worth exploring in the future to help increase the power density of the motor by allowing for more thermal headroom in the stator, winding, and magnet temperatures.

Experimental validation is critical to ensure that the multiphase simulations were carried out correctly.

### 4.3.2 Integrated Hub Manufacturing and Rotor Assembly

The significant undercut created by the large ID and small inlet/outlet hole in the B-side of the rotor shaft makes it difficult or impossible to manufacture the shaft from a single piece of raw material. Three methods are proposed as potential options for manufacturing the integrated shaft which need to be validated using FEA simulations since all three proposed methods require manufacturing the shaft as two separate components before joining. The joint should be placed between the bearing seat and hub on the B-side of the shaft to minimize the torque loads transferring through the joint. This minimizes the effects of any stress risers and compromised joint strength as a result of the manufacturing methods. The first method is friction welding. Akiyama *et al.* [131] evaluated the runout accuracy and weld quality of lightweight friction welded hollow shafts using an ultraprecision friction welding system. Welding two pieces with the same cross-section at the weld location resulted in a weld free of cracks and voids which can be attributed to the welding parameters and symmetrical heat distributions in both parts local to the welding location. The welding process was able to achieve impressive runouts less than 0,10 mm (0.004") over a total shaft length of 325,5 mm in 6 welding trials. For high-speed applications, maximum shaft runouts of 0,04 mm to 0,07 mm (0.001" to 0.003") are recommended between bearing seats [132]. The shaft runout variation seen in [131] may be minimized through process refinement, welding machine design, or post-machining of critical surfaces to the required specification. The resulting weld leaves excess material in the shape of a curved lip on each side of the weld which may affect the flow within the hollow shaft. Additionally, post-weld heat treatment must be completed to maintain the required material properties. The second manufacturing method is conventional welding. Conventional welding is simple, well understood, and can be easily controlled, especially in terms of accuracy. The runout accuracy can be increased by designing more accurate jigs to hold each part of the shaft during welding. Just as with the friction welding solution, the part will require post-weld heat treatment to restore the mechanical properties of the part surrounding the weld. The third manufacturing option is using a simple press fit or shrink fit. A press fit is simple, low-cost, and consistent, however the largest drawback is the reduced part stiffness which reduces the critical speed and modal frequencies of the rotating assembly. Conventional welding would be the primary choice of manufacturing method for the shaft due to its simplicity and accuracy, avoiding the need to post-machine the shaft to the required tolerance.

Glue is used to initially retain the magnets before a carbon sleeve is wrapped onto a mandrel and press fit on the OD of the magnet array. As discussed in section 3.3.2, the use of a carbon retaining sleeve results in a high strength and high stiffness sleeve with low generated losses and low weight. Due to the unpredictability of composite components, the sleeve is built well past the minimum required thickness to ensure that the sleeve does not fail.

### 4.3.3 Bearing Selection, Lubrication, and Integration

The bearings used in the rotating assembly are 15° angular contact high precision hybrid bearings. DGBBs are typically used for standard radial flux motors, especially when axial and radial loading is relatively low, however the thermal and mechanical speed ratings of off-the-shelf DGBB options are lower than that of the available high precision angular contact hybrid bearings. This is attributed to the higher levels of precision, the use of silicon nitride rolling elements, and the use of better cage materials, such as phenolic or Polyether Ether Ketone (PEEK) cages compared to standard stamped sheet steel cages. The increased limiting speeds of the angular contact bearings relative to the DGBB results in a larger selection of bearing sizes, with larger bearings providing higher stiffness at the cost of higher generated losses. A 35 mm bearing is chosen as a compromise between generated losses and bearing stiffness. Bearing spacing is determined based on the largest shaft ID for the optimization study of the rotor cooling solution, which is shown in Fig. 4.11 and is further described in the following chapter. FEA analysis of the rotating assembly should be carried out to determine whether the bearing spacing is sufficient and whether smaller bearings may be used. It should be noted that the higher limiting speeds and lower losses of the high precision angular contact bearings results in higher costs. Since the proposed motor is intended for aerospace applications, this may be feasible since higher cost components can be justified for better performance compared to other industries like the automotive industry. A 250 N preload is applied to the outer race of the B-side bearing using a wave spring. The preload is chosen to maximize bearing life without allowing for excess skidding of the rolling elements in the bearing races. Wave spring preloading minimizes the variation in the bearing preload due to the CTE differences between the stator assembly, which is primarily the aluminum housing, and the rotor assembly, which is primarily the steel shaft. A hard preload method, using shims for example, results in a much larger variation in preload over the temperature range due to CTE differences since the effective spring rate depends on the stiffness of the assemblies, which is much higher than the spring rate of a wave spring.

To use a wave spring to preload the bearing, a tight slip fit must be used and maintained between the outer race and the end plate throughout the operating temperature range to allow for relative movement while a slight press fit, or line fit, is used between the inner race and shaft. Maintaining a tight slip fit is not possible between a steel outer race and aluminum end plate due to the significant CTE differences. To address this, a steel sleeve is shrink fitted into the end plates on both sides of the motor. The variation in the fit between the sleeve and end plates results in a much smaller relative deflection between the sleeve and the outer raceway, resulting in a more consistent fit for the outer race. Shrink fit calculations were performed using the same equations and methods used for the stator to housing fit. Minimum required radial interference calculations were not performed since the torque applied to the sleeve by the outer race of the bearing is negligible, therefore the minimum radial interference required is any amount larger than no interference. At low interferences, vibration may be an issue that could cause relative movement between the sleeve and end plate, although this can be addressed by knurling one of the parts or opting for a tighter fit. The input parameters, LMC & MOT, and MMC & LOT are shown in Table 4.7 to Table 4.9. The bearing assemblies on the A-side and B-side of the motor along with the dimensions used for the shrink fit calculations are shown in Fig. 4.12.

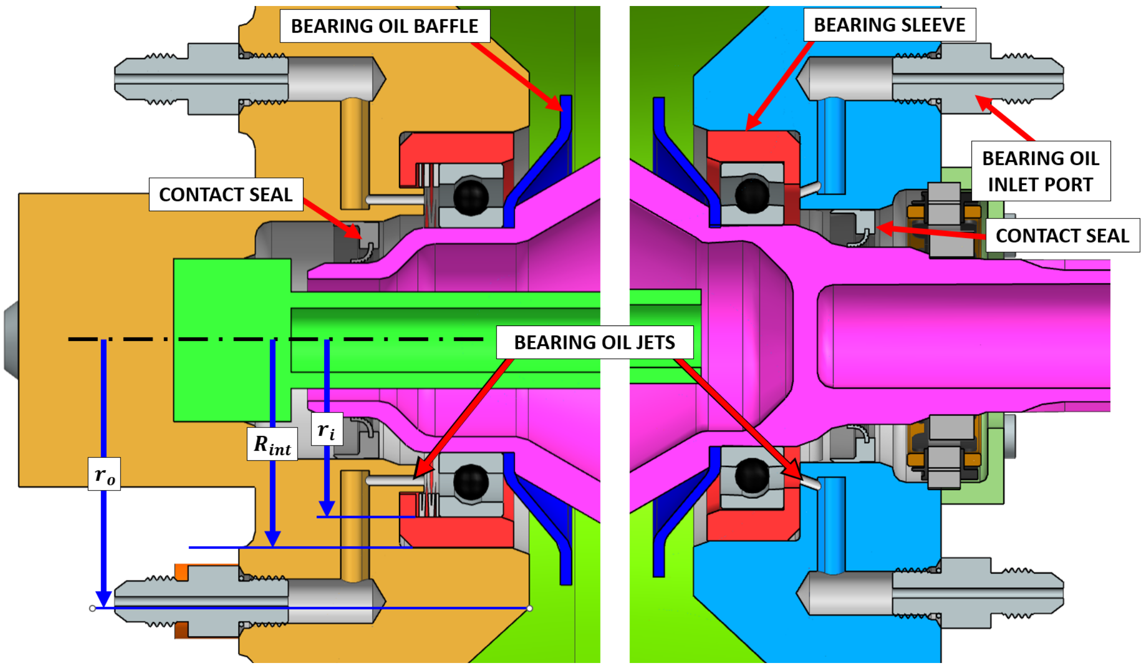


Figure 4.12: Cross-section of the bearing assemblies on the B-side (left) and A-side (right). Blue arrows indicate the radii used for the bearing sleeve shrink fit calculations.

The bearings are cooled and lubricated using oil jet lubrication, which is the best performing cooling and lubrication method for high-speed bearings. Although the operating speed is well within the limits of the bearing using grease lubrication, adequate cooling of greased bearings is much harder, especially for larger bearing sizes. As a result, more complex and expensive cooling systems would have to be used to adequately cool the bearings, such as customizing the outer race of the bearing with a helical cooling channel or using a cooling jacket within the end plate to cool the bearings, methods covered in section 3.3.1, both of which increase the complexity

Table 4.7: Input parameters for the calculation of the sleeve-end plate shrink fit.

| **Geometric Parameters** | | |
|---|---|---|
| Sleeve Inner Radius (mm) | $r_i$ | 27.5 |
| End plate Outer Radius (mm) | $r_o$ | 41.7 |
| Transition Radius (mm) | $R_{int}$ | 32.4 |
| Interface Length (mm) | $L_{int}$ | 14.7 |
| Interface Coefficient of Friction (-) | $\mu_f$ | 0.15 |

| **Material Properties** | | |
|---|---|---|
| Sleeve Elastic Modulus (MPa) | $E_i$ | 190,000 |
| End plate Elastic Modulus (MPa) | $E_o$ | 70,000 |
| Sleeve Poisson Ratio (-) | $\nu_i$ | 0.28 |
| End plate Poisson Radio (-) | $\nu_o$ | 0.30 |
| Sleeve CTE (1/°C) | $\alpha_i$ | 1.2 x $10^{-5}$ |
| End plate CTE (1/°C) | $\alpha_o$ | 2.2 x $10^{-5}$ |

| **Physical Conditions** | | |
|---|---|---|
| Max. Operating Temperature (°C) | $T_{max}$ | 130 |
| Min. Operating Temperature (°C) | $T_{min}$ | 25 |

Table 4.8: Sleeve outer diameter and end plate bore diameter tolerances.

| | Inches | Millimeters |
|---|---|---|
| Sleeve Outer Diameter | $2.550^{+0.001}_{+0.000}$ | $64.770^{+0,025}_{+0,000}$ |
| End plate Bore Diameter | $2.550^{-0.0040}_{-0.0050}$ | $64.770^{-0,102}_{-0,127}$ |

Table 4.9: Stator-housing interferences and stresses under the limiting conditions.

| | | MMC & LOT | LMC & MOT |
|---|---|---|---|
| Sleeve Radius (mm) | - | 32.413 | 32.441 |
| End plate Radius (mm) | - | 32.337 | 32.424 |
| Radial Interference (mm) | $\delta_{int}$ | 0.076 | 0.017 |
| Interface Contact Pressure (MPa) | $p_{int}$ | 25.26 | 32.42 |
| Sleeve Tangential Stress (MPa) | $\sigma_{t,i}$ | -155.42 | -34.36 |
| End plate Tangential Stress (MPa) | $\sigma_{t,o}$ | 102.40 | 22.71 |
| End plate Effective Stress (MPa) | $\sigma_o$ | 117.09 | 25.96 |

of the cooling system. Two lubrication points are present for each bearing which are located at 180° with respect to each other to ensure the bearings are adequately cooled and lubricated, however utilizing one of the two supplied jets should be adequate. Low viscosity VG32 hydraulic oil, a common bearing lubricating oil suitable for high-speed applications, is sent through channels integrated into the end plates of the motor as shown in Fig. 4.12. Accurately simulating bearing thermal performance is highly complex and time consuming as it depends on many factors in the geometry and operating conditions. Therefore, thermal performance should be determined experimentally by varying the flow rate through the oil jets and monitoring the losses and bearing temperatures, ensuring the bearing is well within it's operating temperature limits without generating excessive churning losses. The oil drains into the motor cavity towards the end plates after hitting a baffle placed in front of the bearings shown in Fig. 4.10 and Fig. 4.12. to ensure that the lubricating oil is flung radially, preventing the oil from moving towards the air gap where the presence excess oil ingress could lead to elevated windage losses. The baffle is only a precautionary measure since the flow structures within the airgap likely provide a strong blocking effect to any incoming oil, however the effectiveness of the drainage path and effects of oil within the airgap should be determined experimentally. The drainage system avoids the primary issue of oil pooling at the ID of the stator to partially or fully fill the airgap, which significantly increases windage losses and potentially causes issues like foaming as seen in [91].

## 4.4 Chapter Summary

This chapter provides an overview of a power a high-speed dense radial flux surface mounted PM motor proposed for this thesis, highlighting the electromagnetic design, stator design and manufacturing, and rotor design and manufacturing. The housing and end plate designs provide an opportunity for the use of AM to reduce part count, and reduce overall weight, thereby improving the power density of the machine. AM is especially suitable for the aerospace industry and in prototype projects where individual part costs may be sacrificed for performance. The design of both components are discussed accounting for the post machining required at the critical locations. The stator shrink fitting process is presented with the relevant calculations accounting for the tolerances and thermal expansion to ensure that the stator does not move under load. Finally, multiple insulation processes are described and the potting process is justified given the stator cooling design and is described using the potting tooling as a reference.

The second half of the chapter introduces the mechanical design of the rotating assembly, rotor cooling loop, shaft mechanical design and manufacturing, sleeve material, and bearing integration. The initial design of the cooling loop is presented with the largest possible shaft ID tested in the optimization study in the following chapter, which limits to the positions of the bearings to the locations shown in this chapter. Methods for manufacturing the integrated shaft and hub are presented since conventional billet manufacturing was not deemed feasible with the design as shown. The chapter concludes with the bearing selection, integration and lubrication. High precision hybrid angular contact bearings are chosen for this application for their higher permissible operating speeds and lower generated losses when compared to a DGBB of a similar size. To allow for relative movement between the outer race of the bearings and the end plates throughout the full operating temperature range, a sleeve shrink fitting process is presented which mirrors the stator shrink fitting process. Finally, the bearing lubrication is simplified by opting for oil jet lubrication with a simple drainage solution that uses angled surfaces in the potting within the end winding regions to move the oil towards the end plates.

The final weight of the motor is 23.9kg, resulting in a power density of 6.28 kW/kg. This power density exceeds most of the motors presented in Chapter 2 with the exception of motors from H3X, Helix, and the Evolito D500. It is important to note that the designs for the stator and rotating assemblies require mechanical FEA to identify and address any significant stress concentrations and less rigid locations leading to undesirable vibration characteristics in the stator and rotating assemblies. Alternatively, mechanical analysis may reveal areas where material can be removed, improving power density. The following chapter will provide a deep dive into the thermal analysis of the rotor cooling design presented in this chapter, using CFD to optimize the design of the rotor cooling loop.

# Chapter 5

# Rotor Thermal Modeling, Analysis, and Optimization

This chapter provides an extensive review of the analysis and optimization of the rotor cooling design using the Taguchi method for optimization in conjunction with ANSYS CFX. The first section begins with a discussion on the theory behind the thermal CFD analysis presented in this chapter, mainly covering the Navier Stokes equations, energy equations, turbulence modeling, and other relevant equations. Before delving into the CFD analysis, the motor losses are highlighted, restricting the values presented in this section to the relevant loss figures used in the analysis (e.g. winding losses are excluded). Next, the geometry used in the analysis is shown with simplifications and assumptions made to minimize the computational load of the simulations with a minimal impact on accuracy. The boundary conditions are then presented, highlighting regions where the losses are applied to the model. The meshing is discussed along with mesh independence studies that were conducted to validate the mesh sizing used in the subsequent simulations. The background on the Taguchi method for design optimization is then introduced before applying the optimization method to the rotor cooling design and presenting the results of the Taguchi Design Of Experiments (DOE). Performance metrics for the Taguchi method, known as signal to noise ratios, are shown using the results of the DOE to determine the effects of changes in the DOE parameters on the relevant outputs from the simulations. Finally, the signal to noise ratios are used to determine an optimal rotor cooling design to minimize the magnet temperatures. The simulation results of the final design are presented and its effects on the other simulation outputs are highlighted.

## 5.1 Governing Equations

In this section, the mass, momentum, and energy equations are presented. Rotational effects are discussed for each of the applicable equations considering the rotating reference frame approach. Since the equations depend on the physics and desired accuracy of the model, the discussion is limited to the relevant equations for the rotor simulations. The equations have been simplified for steady state, 3-dimensional, incompressible flow. Therefore, any time-dependent terms ($\frac{\partial}{\partial t}$) and density gradients ($\nabla\rho$) have been equated to zero, and density is constant.

### 5.1.1 Navier Stokes Equations

The continuity and momentum equations are defined by the following equation:

$$\nabla U = 0 \tag{5.1}$$

$$\rho \nabla \cdot (U \otimes U) = -\nabla p + \nabla \cdot \tau + S_M \tag{5.2}$$

where $U$ is the velocity field, $U \otimes U$ is the outer product $UU^T$, $\tau$ is the shear stress, p is the pressure field, and $S_M$ is the source term.

### 5.1.2 Total Energy Equation

The total energy equation is defined by the following equation:

$$\rho \nabla \cdot (U h_{tot}) = \nabla \cdot (\lambda \nabla T) + \nabla \cdot (U \cdot \tau) + U \cdot S_M + S_E \tag{5.3}$$

where $\nabla \cdot (U \cdot \tau)$ represents the work due to viscous stresses, $U \cdot S_M$ represents the work due to external momentum sources, and $S_E$ represents any additional energy sources. $h_{tot}$ is the total enthalpy, related to static enthalpy by:

$$h_{tot} = h + \frac{1}{2}U^2 \tag{5.4}$$

Subtracting the mechanical energy equation from the total energy equation yields the following thermal energy equation after neglecting time dependent terms and assuming constant fluid properties:

$$\rho \nabla \cdot (Uh) = \nabla \cdot (\lambda \nabla T) + \tau : \nabla U + S_E \tag{5.5}$$

### 5.1.3 Conjugate Heat Transfer (CHT) Equation

The CHT equation is used to solve heat transfer within solid domains within the simulation using the following equation:

$$\rho \nabla \cdot (U_S h) = \nabla \cdot (\lambda \nabla T) + S_E \tag{5.6}$$

where $U_S$ and $S_E$ are solid motion and volumetric heat source terms, respectively. Solid motion is optional within CFX and is used when a solid and fluid rotate with the same rotational speed among other cases irrelevant to the simulations in this chapter. The left hand side of the equation is simply an advection term that applies to the temperature field. In the case of the proposed motor a stationary reference frame, and therefore zero solid motion, is also valid but confusing with regards to model setup.

## 5.2 Rotation Effects

For reference frames rotating at speed $\omega$, additional sources of momentum must be accounted for within the momentum equations. The forces responsible for this additional momentum are the Coriolis force ($S_{Cor}$), centrifugal force ($S_{cfg}$), and angular acceleration ($S_{M,\omega}$):

$$S_{M,rot} = S_{Cor} + S_{cfg} + S_{M,\omega} \tag{5.7}$$

$$S_{Cor} = -2\rho\omega \times U \tag{5.8}$$

$$S_{cfg} = -\rho\omega \times (\omega \times r) \tag{5.9}$$

$$S_{M,\omega} = -\rho\frac{\partial\omega}{\partial t} \times r \tag{5.10}$$

where $S_{M,rot}$ is the total source from rotational effects. Since the simulations are run under steady state conditions, the angular acceleration source term is zero. Rotating flows also affect the total and thermal energy equations. The advection term within the energy equations use rothalpy, $I$, defined by the following equation:

$$I = h_{stat} + \frac{1}{2}U^2 - \frac{1}{2}\omega^2 R^2 \tag{5.11}$$

## 5.3 Turbulence Modeling

Turbulence consists of time-dependent fluctuations within the flow field resulting in complex eddies that are hard to accurately model. This modeling difficulty stems from the three dimensional, unsteady nature of the flow that consists of a large range of scales. In order to resolve the smallest Kolmogorov scales in turbulent flows, Direct Numerical Simulation (DNS) may be used with an extremely fine mesh. However, the computational expense of DNS is orders of magnitude higher than practical simulations which limits the control volumes in DNS to very small domains, which is impractical for most applications. Turbulence modeling is introduced to account for the effects of turbulence without the computational cost from the prohibitively fine mesh used in DNS.

Apart from Large Eddy Simulation (LES) and Detached Eddy Simulation (DES), most turbulence models use a statistical approach. The approach introduced by Reynolds decomposes the velocity field $U_i$ into a time averaged component $\overline{U_i}$ and fluctuating component $u_i'$:

$$U_i = \overline{U_i} + u_i' \tag{5.12}$$

Substituting the equation above into the continuity and momentum equations results in the following Reynolds Averaged Navier Stokes (RANS) equations:

$$\nabla \cdot (\overline{U_i} + u_i') = 0 \tag{5.13}$$

$$\rho \frac{\partial (U_i U_j)}{\partial x_j} = -\frac{\partial p}{\partial x_i} + \frac{\partial}{\partial x_j}(\tau_{ij} - \rho \overline{u_i u_j}) + S_M \tag{5.14}$$

Similarly, the Reynolds averaged energy equation is given by:

$$\rho \frac{\partial (U_j h_{tot})}{\partial x_j} = \frac{\partial}{\partial x_j}\left(\lambda \frac{\partial T}{\partial x_j} - \rho \overline{u_j h}\right) + \frac{\partial}{\partial x_j}[U_i(\tau_{ij} - \rho \overline{u_i u_j})] + S_E \tag{5.15}$$

The total enthalpy is given by:

$$h_{tot} = h + \frac{1}{2} U_i U_i + k \tag{5.16}$$

which is similar to Eq. 5.4 except for the addition of the turbulent kinetic energy $k$ given by:

$$k = \frac{1}{2}\overline{u_i^2} \tag{5.17}$$

Turbulence modeling is classified into two main categories: eddy viscosity models, and Reynolds Stress Models (RSMs). Eddy viscosity models rely on the Boussinesq eddy-viscosity approximation which assumes that the Reynolds stress tensor $\tau_{ij}$ is directly proportional to the mean strain tensor $S_{ij}$. These models assumes that the turbulent flow is isotropic, which is incorrect; however, this approach still provides accurate solutions to many engineering problems. Among the most commonly used eddy viscosity models are the $k - \epsilon$ and $k - \omega$ models, also known as two-equation models, with their respective variations to improve turbulence prediction for a more broad range of engineering applications. The $k - \omega$ SST model has been found to be the superior turbulence model for a wide variety of engineering applications due to its ability to use the $k - \epsilon$ and $k - \omega$ formulations where they are most accurate, which is the free-stream and near-wall flow respectively, while avoiding the over prediction of the eddy viscosity using a limiting function. One weakness of eddy viscosity models is that they are insensitive to streamline curvature and system rotation, resulting in under predicted turbulence production. A curvature correction function is available for two-equation models to be used as a multiplier of the production term. A scaling coefficient is available in CFX to tune the curvature correction function.

RSMs do not use the Bousinesq eddy viscosity approximation used in the two-equation models, instead solving an equation for the transport of each component within the Reynolds stress tensor. In 3-dimensional flows, this results in 6 equations that need to be solved, significantly increasing the computational load when compared to the two-equation models. With the introduction of these equations, a number of new unknowns need to be modeled, leading to a variety of RSMs that differ in the modeling of these unknowns. In practice, RSMs are more difficult to achieve convergence compared to two-equation models as they are prone to numerical errors and non-optimal meshes [133]. They are generally not found to be superior to two-equation turbulence models, even for complex flows, therefore reserving RSMs to be used in cases where they have been shown to be superior to two-equation models. A significant advantage of RSMs is the ability to simulate the anisotropy of the Reynolds stresses due to the Coriolis forces in the rotating frames of reference, making them the preferred option for rotating flows [134], although it is suggested that the curvature corrected two-equation models provide similar results to RSMs [133].

Most authors in the literature default to the $k-\omega$ SST turbulence model for hollow shaft cooling simulations since it is ubiquitous and accurate for most engineering applications. Although the recirculating hollow shaft cooling approach is not commonly seen in the literature when compared to conventional hollow shaft cooling, two notable papers, authored by Wang *et al.* [68], [129], mention the use of the $k-\omega$ SST model in their recirculating hollow shaft simulations. The heat transfer measurements were compared between simulations and experimental results. The minimum, maximum, and average discrepancies in the Heat Transfer Coefficients (HTCs) were 13%, 30%, and 20%, respectively, at rotational speeds below 5000 RPM. Meanwhile, Gai *et al.* [63], [87] compared HTCs between experiments and simulations using different turbulence models for a conventional hollow shaft cooling design operating at speeds up to 30 kRPM. The $k-\omega$ SST simulations had minimum and maximum relative errors of 24% and 38% and the RSM simulation had minimum and maximum relative errors of 17% and 27% at speeds above 10 kRPM. The relative error between the $k-\omega$ SST and RSM simulations across the full speed range was smaller than the relative error between the simulations and the experimental results.

The turbulence model chosen for the simulations in this chapter is the $k-\omega$ SST model without curvature correction. Compared to the RSMs, the $k-\omega$ SST model is a more robust turbulence model that requires four fewer equations to be solved in each iteration, however the model comes at a cost of accuracy for rotating hollow shaft flows. Curvature correction was mentioned as a method to account for the under prediction of turbulence in rotating flows in the $k-\omega$ SST model, however simulations conducted by the author attempting to replicate the results from Gai *et al.* [63], [87] with the curvature corrected $k-\omega$ SST model yielded HTC values that did not correlate with HTC values from the RSM and experimental results for the geometry presented in the aforementioned papers. The curvature correction in CFX must be tuned for specific flows and geometries, meaning that experimental results would be required for the proposed rotor cooling design to validate the results of the simulations and provide reference data for the tuning of the curvature correction factor for future design iterations.

## 5.4 Simulation Setup

### 5.4.1 Motor Losses

A list of losses applied in rotor simulations are shown in Table 5.1. The airgap windage losses were calculated using Eq. 3.3 to Eq. 3.6 at 20 kRPM and at a 100°C assumed air temperature for the density and dynamic viscosity. The airgap is accountable for a majority of the windage losses in the proposed motor, therefore the windage losses generated by the other surfaces of the rotor are ignored. Generated loss values were not available for the bearings chosen for the proposed motor at the given operating operating condition, therefore conservative bearing loss values were generated using

SKF SimPro Quick. Conventional 35 mm angular contact bearings lubricated by VG32 oil were tested with the given shaft geometry, bearing preload, and operating speed. Losses for the low-friction shaft seals were estimated using the available loss data from the seal supplier [130].

Table 5.1: Losses considered in the rotor CFD simulations.

| Loss Parameter | Total Loss (W) |
|---|---|
| Magnets | 172 |
| Airgap Windage | 62 |
| Bearing (Each) | 1220 |
| Seal (Each) | 180 |

### 5.4.2 Geometry Simplification

The geometry of the rotor hub is simplified to reduce the computational load of the simulation without significantly affecting the accuracy. Most of the analysis presented in this chapter is performed on a 60° sectional model of the rotor geometry as shown in Fig. 5.1. The computation time is minimized by limiting the simulation domain to the fluid domain, integrated shaft, magnets, and carbon fiber sleeve. The fluid domain can be further broken down into the rotating domain, inlet tube flow, inlet extension, and outlet extension. The inlet tube itself is excluded as it does not provide any useful information in the simulations. The inlet and outlet extensions are present to avoid reverse flow effects at the boundaries. The air within the motor cavity is excluded from all simulations since the airgap loss account for a majority of the windage loss.

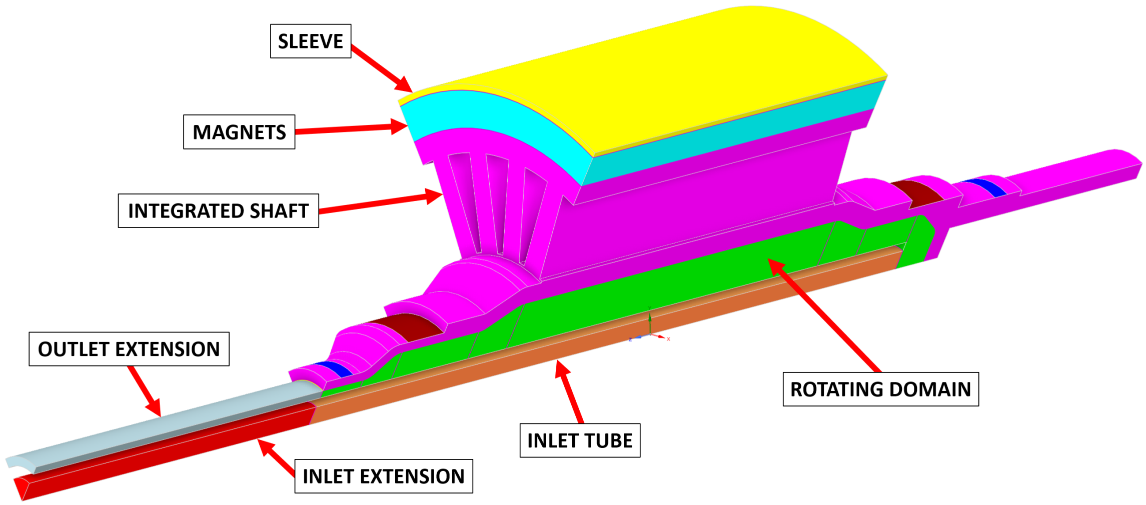


Figure 5.1: 60° model with the solid and fluid domains used in the CFD analaysis.

Two versions of the geometry were initially used for the mesh independence studies discussed in section 5.5: a full rotor model and the previously mentioned sectional rotor model. Results between the two models were compared to ensure minimal variance between the two geometries, validating the use of the sectional geometry in subsequent simulations to reduce computation time. The true outlet geometry as shown in the CAD model in the previous chapter (Fig. 4.11) is not included in the simulation as the location of the outlet port is offset from the axis of the motor, making it impossible to accurately model in the sectional model. Instead the region where the fluid exits the rotor shaft is considered the outlet in the full rotor and sectional simulations. The magnet array in the proposed motor is simplified to a single body with a simple contact resistance included between the magnet array and rotor hub to account for the adhesive used to glue the magnets to the hub. Finally, the carbon sleeve is a simplified body with anisotropic thermal conductivity. While the thermal conductivities are not completely accurate in the axial and circumferential direction due to the layering of the carbon fiber, the variation in the axial and circumferential direction are minimal and not important.

### 5.4.3 Rotation Modeling

Rotation is modeled using the Multiple Reference Frame (MRF) approach. This modeling approach is used in simulations with domains rotating relative to one another. The stationary part of the fluid domain contains the inlet tube flow, inlet extension, and outlet extension regions. The rotating part consists of the fluid from the exit of the inlet tube region to the entry of the outlet extension. Centrifugal and Coriolis forces are considered within the rotating domain.

### 5.4.4 Boundary Conditions

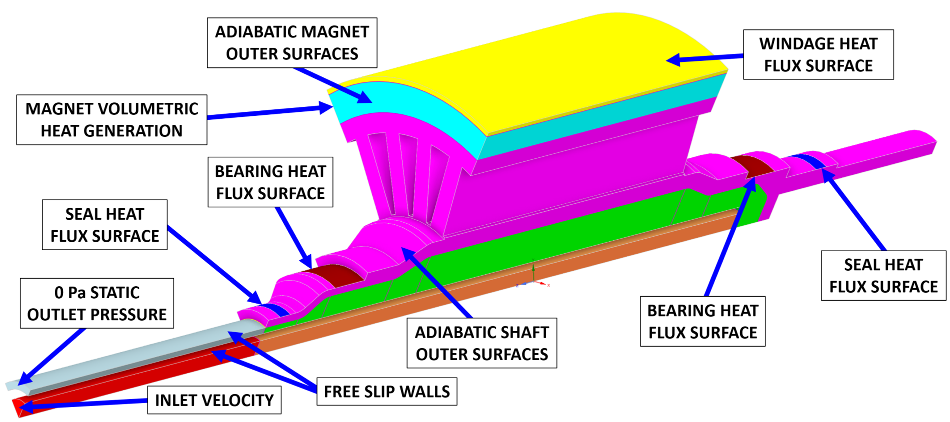


Figure 5.2: 60° model highlighting the boundary conditions of the simulation.

The sectional model is shown in Fig. 5.2, highlighting the locations of the boundary conditions presented in this section. Normal velocity and static pressure outlet

Table 5.2: Material properties of WEG 50/50 at 80°C.

| Property | Value |
|---|---|
| Density (kg/m$^3$) | 1081.3 |
| Specific Heat Capacity (J/kgK) | 3273 |
| Freezing Point (°C) | -38 |
| Boiling Point (°C) | 107 |
| Dynamic Viscosity (cP) | 3.23 |
| Thermal Conductivity (W/mK) | 0.233 |

boundary conditions are applied to the inlet and outlet, respectively. The inlet velocity varies based on different inlet flowrates and inlet tube geometries, which are discussed in section 5.6.2. The inlet flow temperature is 80°C, which is a prescribed value provided for the motor design. Material properties for the WEG 50/50 are shown in Table 5.2. The inlet and outlet extension regions contain free-slip walls to prevent the walls within these regions from contributing to the overall pressure drop and affecting the upstream flow. The OD of the inlet tube wall, which is also the ID of the rotating domain, is given a counter-rotating wall velocity in the rotating frame of reference which equates to a stationary wall in the stationary frame of reference. A periodic interface is set at each set of periodic faces in the sectional geometry. The windage losses, shaft seal losses, and magnet losses shown in Table 5.1 are applied as a heat flux on the OD of the carbon sleeve, a heat flux on the contact patch of the contact seal at each end of the shaft, and a volumetric heat generation within the magnet body respectively. The bearing losses are also considered in the simulation, however the exact distribution of the bearing losses into the rotor is difficult to quantify since the effectiveness of the oil-jet lubrication plays a significant role in determining the losses dissipated into the rotor and end plates. Therefore, half of the individual bearing losses shown in Table 5.1 are applied as a heat flux on each bearing seat as a highly conservative estimation. The remaining surfaces of the integrated shaft are given an adiabatic boundary condition. The heat transfer from the rotor to the air within the motor cavity is minimal when compared to the heat transferred to the forced liquid cooling, therefore this assumption can be justified.

## 5.5 Meshing

The final mesh of the solid and fluid domains for the sectional model is shown in Fig. 5.3. Hexahedral meshing is used where possible within the fluid domain to minimize numerical diffusion. Inflation layers are applied near the walls to fully capture the flow physics within the boundary layer. A first layer thickness is chosen to provide a $y^+ < 1$ value at the wall, as recommended for the $k - \omega$ SST model, and a smooth transition between the final elements of the inflation layer and the free stream mesh elements is ensured to avoid numerical errors. A 2 mm mesh is used for the solid domain since a high resolution in the axial and radial temperature distributions is not required. Meshing quality differed between the full rotor and sectional rotor simulations. The mesh within the full rotor geometry contained uneven inflation layers in some regions of the rotating fluid domain and the mesh within the outlet regions of the fluid domain contained only a single element in the radial direction outside of the inflation layers which likely resulted in inaccuracies within this region of the fluid domain. Meshing of the sectional rotor geometry was much more uniform

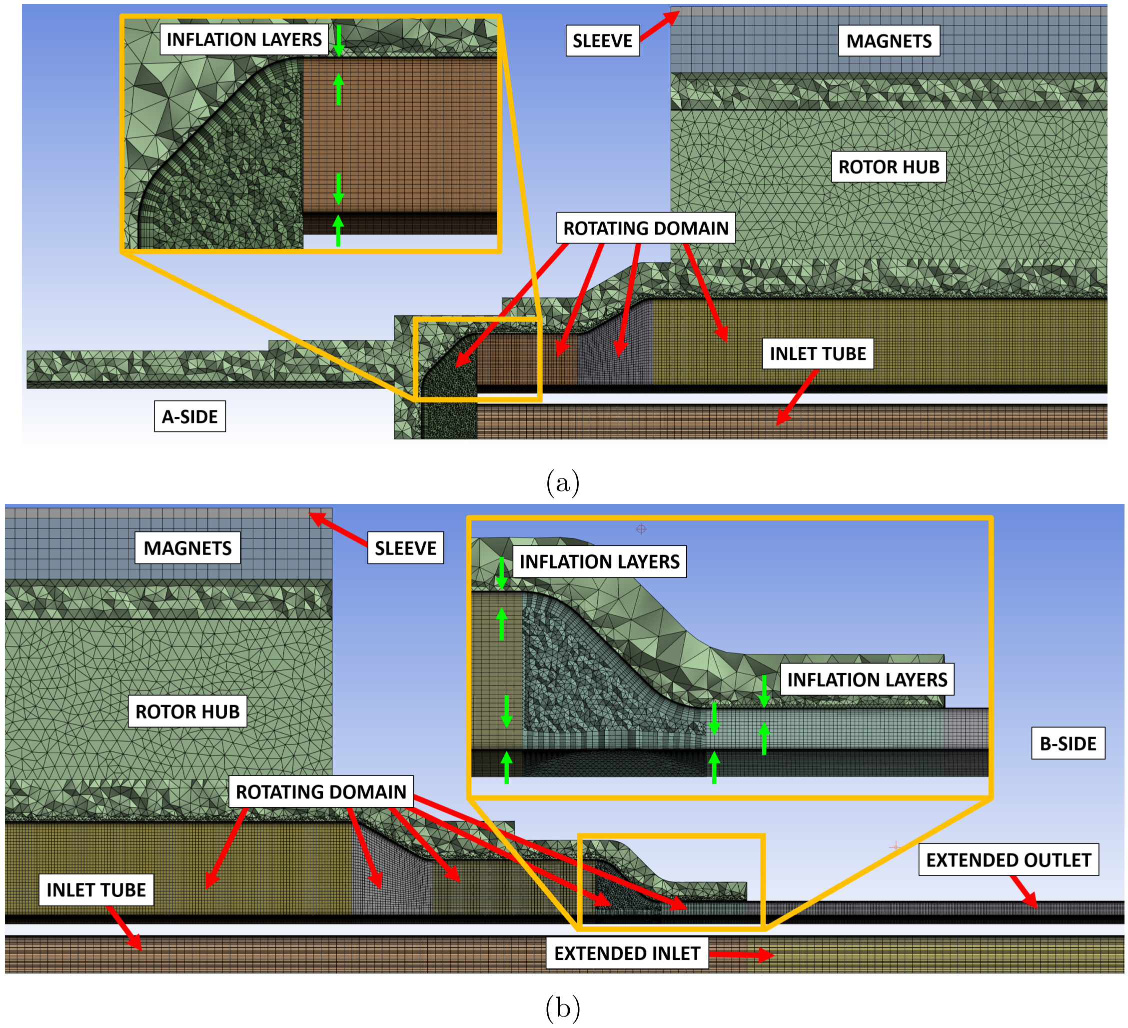


Figure 5.3: Sectional model mesh of a) A-side of the simulation domain, and b) B-side of the simulation domain.

and acceptable, especially in the outlet region where a fine mesh was maintained with a smooth transition between the last elements within the inflation layer and the free stream mesh to properly resolve the flow field.

### 5.5.1 Mesh Independence Study

To achieve accurate results, mesh independence studies were conducted. This involved refining the mesh (i.e., increasing the element count) until the simulation results showed minimal changes. The final results of the mesh independence studies are shown in Table 5.3. The maximum magnet temperature, HTC, pressure drop, and fluid friction loss were monitored as these are the desired outputs from the analysis later used in the Taguchi method in section 5.6.2. Mesh 1 to 4 simulations used full rotor and fluid geometry whereas mesh 5 to 7 used the 60° sectional model due to the high computational load of the full model simulations with increasingly refined meshes. It should be noted that the element count for the sectional models in Table 5.3 reflects the equivalent number of elements for a full model; i.e., the element count should be divided by 6 to acquire the true element counts of the sectional simulations.

There are three notable deviations in the mesh independence study simulations that result in differences in the ouput parameters when compared to simulations presented later in this chapter: seal losses were excluded, bearing losses were lower than the final value presented in Table 5.1, and the geometry differed slightly from the final simulations. The reason behind these deviations is that the mesh independence studies were carried out before finalizing the loss values and geometry. Note that the changes in the geometry between the mesh independence studies and the final models are minor did not impact the meshing strategy used in subsequent simulations.

Note that only the relative errors of the HTC and fluid friction loss are listed in Table 5.3 because these outputs see a consistent convergence with increasing element

Table 5.3: Results of the mesh independence study.

| Mesh # | Full/Section Geometry | Magnet Max Temp. (°C) | HTC (W/m$^2$K) | Pressure Drop (Pa) | Fluid Friction Loss (W) | Element Count (x10$^6$) | HTC Rel. Error (%) | Friction Loss Rel. Error (%) |
|---|---|---|---|---|---|---|---|---|
| Mesh 1 | Full | 95.335 | 14037 | 38017 | 512 | 2.50 | - | - |
| Mesh 2 | Full | 95.521 | 12849 | 38233 | 364 | 3.90 | 8.5 | 22.9 |
| Mesh 3 | Full | 95.987 | 10097 | 40508 | 253 | 6.52 | 21.4 | 30.5 |
| Mesh 4 | Full | 96.410 | 8444 | 32350 | 196 | 9.70 | 16.4 | 22.5 |
| Mesh 5 | Section | 96.691 | 7700 | 32905 | 168 | 11.13 | 8.8 | 14.3 |
| Mesh 6 | Section | 96.897 | 7158 | 36769 | 147 | 22.00 | 7.0 | 12.5 |
| Mesh 7 | Section | 96.917 | 6960 | 6754 | 140 | 29.49 | 2.8 | 4.8 |

Relative errors were calculated using the following formula: $Rel.Error = |\frac{current-old}{old}| \times 100\%$

counts. The magnet temperatures see the same convergence, although the change in temperatures throughout the runs is very small. The pressure drop does not show a clear trend with increasing element counts, instead remaining between 32 kPa and 40 kPa with the exception of the pressure drop from mesh 7. Since the HTC and fluid friction loss less than a 5% relative error between mesh 6 and mesh 7, the subsequent simulation geometries are meshed using the mesh size from mesh 6. The pressure drop for mesh 7 is deemed an erroneous result and is therefore ignored. The validity of the inflation layer mesh in mesh 6 is verified by observing the contour plot for the y$^+$ value along the walls of the fluid domain, and the velocity profile in the axial and circumferential directions throughout the fluid domain. Fig. 5.4 shows that the y$^+$ values are well below 1 in all but one small region which does not impact the results of the simulation. Additionally, the boundary layer flow is shown to be fully captured within the inflation layers in both the axial and circumferential directions as seen in Fig. 5.5.

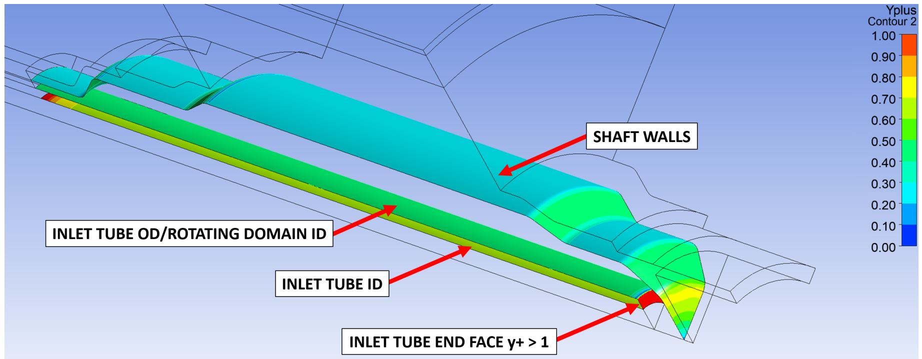


Figure 5.4: $y^+$ contour plot on the no-slip walls of the fluid domain.

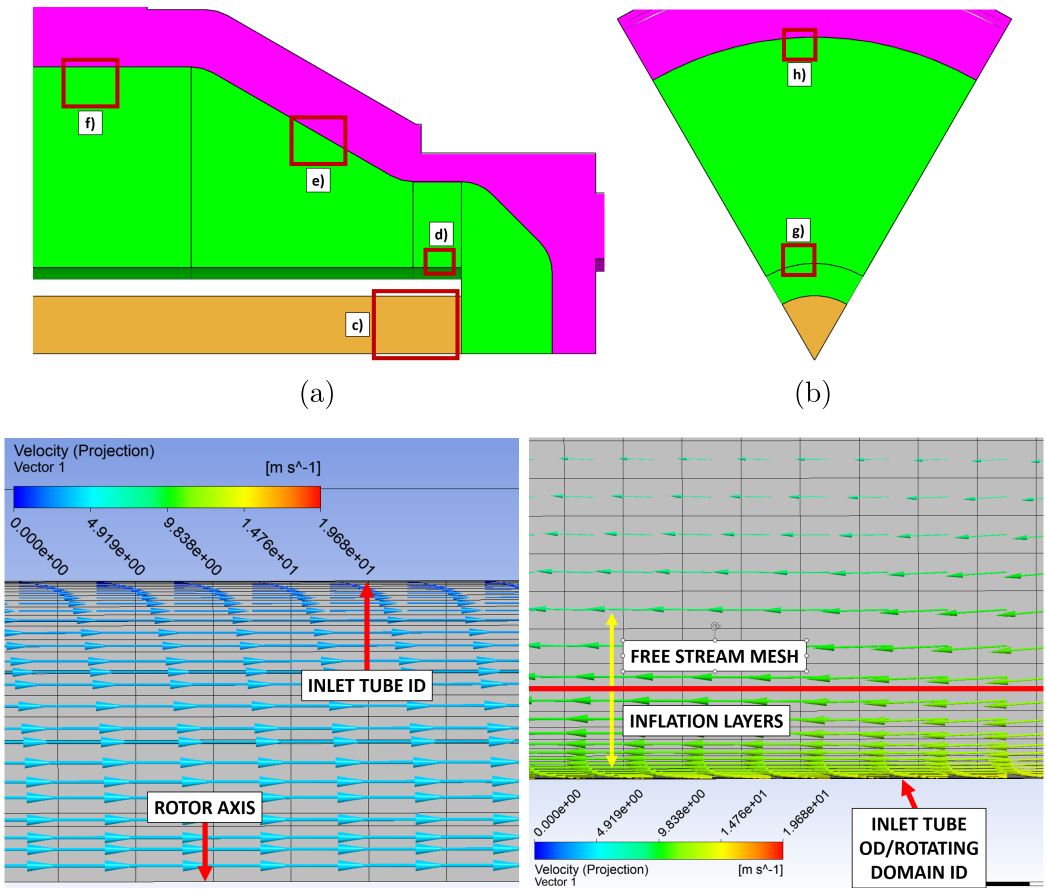


(a) (b)

(c) (d)

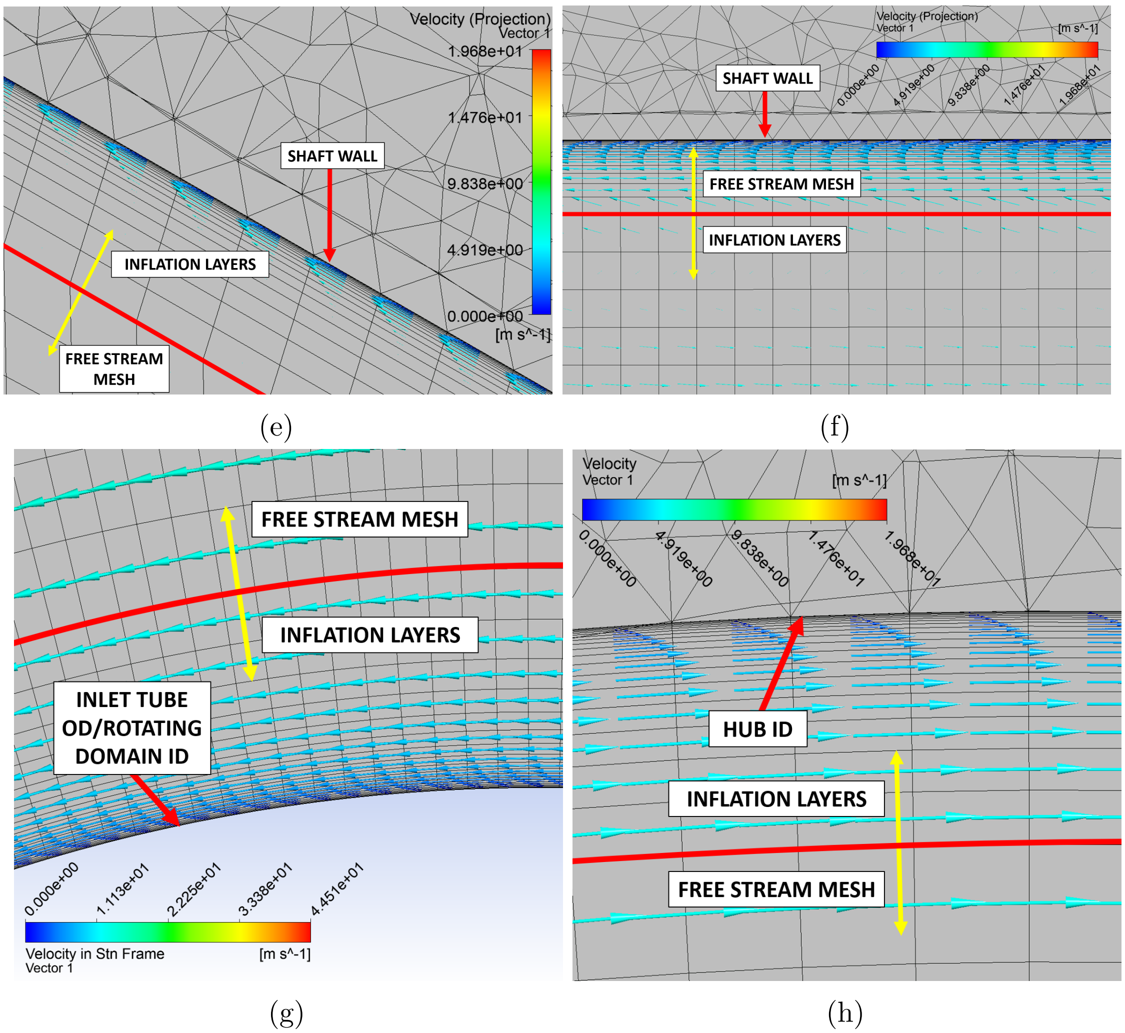


Figure 5.5: Velocity profiles within the boundary layers at key locations shown in a) and b) within the fluid domain in c)-f) the axial direction, and g), h) the circumferential direction.

## 5.6 Taguchi Method for Design Optimization

### 5.6.1 Background

The Taguchi Method is a statistical design method originally used to improve the quality of manufactured goods, however this method has been used extensively in many areas of interest including the optimization of rotor thermal designs [92], [93], [102], [135]. In the case of the proposed motor, the Taguchi method was used to determine the effect of multiple input parameters on the performance of the design. Given a number of factors and levels for each factor, an orthogonal array can be constructed for a DOE. Taguchi orthogonal arrays are denoted as "$LN(L^P)$" arrays where N is the number of runs with L and P in $L^P$ denoting the number of levels and factors in the DOE, respectively. The arrays are constructed such that for any level of any factor, all levels from each of the other factors are tested at least once. Taguchi orthogonal arrays are predetermined and the required array can be chosen if the number of factors and levels are known. For example, a 3 factor 3 level orthogonal array requires a total of 9 runs and is denoted as an $L9(3^3)$ orthogonal array. The orthogonal array for this DOE is shown in Table 5.4. Note that a full factorial design, where each combination of factors and levels are tested exactly once, requires a total of $L^P$ runs, which is a total of 27 runs in this example.

The Taguchi method uses Signal to Noise (S/N) ratios to quantify the effectiveness of a given level of a factor. The desired goals for the outputs of the experiments must be known in order to calculate the S/N ratios. The three goals in the Taguchi method and their associated S/N ratios formulations are shown in the Table 5.5. "Smaller the better" is typically the goal for temperatures of critical components within the motor, such as the windings or magnet temperatures.

Table 5.4: Taguchi L9($3^3$) orthogonal array example. "a", "b", and "c" denote the factors and "1", "2", and "3" denote the levels.

| Run # | a | b | c |
|---|---|---|---|
| #1 | 1 | 1 | 1 |
| #2 | 1 | 2 | 2 |
| #3 | 1 | 3 | 3 |
| #4 | 2 | 1 | 2 |
| #5 | 2 | 2 | 3 |
| #6 | 2 | 3 | 1 |
| #7 | 3 | 1 | 3 |
| #8 | 3 | 2 | 1 |
| #9 | 3 | 3 | 2 |

Table 5.5: Signal to noise ratio formulations.

| Goal | Data Characteristic | S/N Formula |
|---|---|---|
| Larger the Better | Positive | $S/N = -10 \cdot \log(\sum(1/Y^2)/n)$ |
| Nominal is Best | Positive, zero, or negative | $S/N = -10 \cdot \log(\sigma_d^2)$ |
| Smaller the Better | Non-negative with a target value of zero | $S/N = -10 \cdot \log(\sum(Y^2)/n)$ |

### 5.6.2 Taguchi DOE for the Optimization of the Rotor Cooling Design

Four factors were chosen for the application of the Taguchi method to the rotor design, shown in Fig. 5.6: the inlet tube ID, annular gap thickness at the outlet of

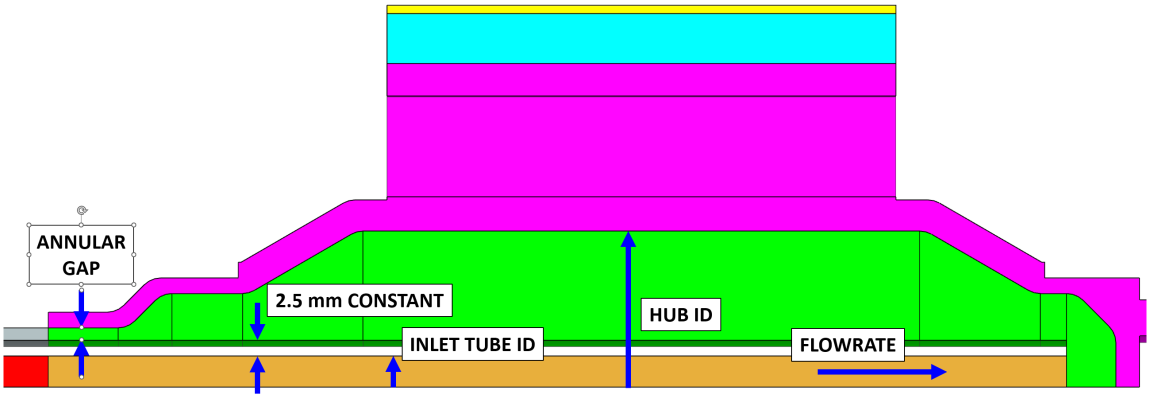


Figure 5.6: Sectional model highlighting the factors of the Taguchi DOE.

the rotating domain, the largest ID within the integrated shaft, denoted at the hub ID, and the inlet flowrate. These factors were chosen as they were thought to have the most significant impact on the outputs. The relevant outputs of the experiments previously mentioned in section 5.5 are the maximum magnet temperature, HTC, pressure drop, and fluid friction loss. The hub ID was thought to have the largest impact on the magnet temperatures due to the reduction in hub material in the radial direction, resulting in a lower thermal resistance and lower magnet temperature. The wall thickness of the stationary tube was kept at a constant 2.5 mm thickness, as shown in Fig. 5.6, meaning that changes in the inlet tube diameter also changed the diameter of the shaft at the annular gap.

A total of 3 levels were chosen for each factor to create an L9($3^4$) array. The DOE was restricted to 3 levels since an increase to 4 levels for a 4 factor design would have resulted in a total of 16 runs (L16($4^4$)). Similarly, the DOE was restricted to 4 factors as an increase to 5 factors would have resulted in a total of 18 runs (L18($3^5$)). A summary of the factors, levels, and orthogonal array are shown in the Table 5.6 and Table 5.7.

Table 5.6: Parameters and levels used for the Taguchi method.

| Level | Tube ID (a) | Annular Gap (b) | Hub ID (c) | Inlet Flowrate (d) |
|---|---|---|---|---|
| 1 | 5 mm | 1.5 mm | 34 mm | 5 LPM |
| 2 | 10 mm | 2 mm | 42.5 mm | 10 LPM |
| 3 | 15 mm | 3 mm | 50 mm | 15 LPM |

Table 5.7: Taguchi L9($3^4$) orthogonal array.

| Run # | a | b | c | d |
|---|---|---|---|---|
| #1 | 1 | 1 | 1 | 1 |
| #2 | 1 | 2 | 2 | 2 |
| #3 | 1 | 3 | 3 | 3 |
| #4 | 2 | 1 | 2 | 3 |
| #5 | 2 | 2 | 3 | 1 |
| #6 | 2 | 3 | 1 | 2 |
| #7 | 3 | 1 | 3 | 2 |
| #8 | 3 | 2 | 1 | 3 |
| #9 | 3 | 3 | 2 | 1 |

The maximum magnet temperature is the critical output parameter of the DOE as the rotor cooling design must, at a minimum, keep the magnets below the material's demagnetization temperature of 180°C with any further decrease in magnet temperatures potentially enabling increased in the power output. The HTC is used to understand the effectiveness of the rotor cooling design for future design improvements. The fluid friction loss is required to determine the overall motor efficiency, however this is not critical for this initial revision of the rotor cooling design due to the high losses generated in the bearings and seals that should first be minimized in future revisions. Finally, the pressure drop should be known to size a coolant pump in a cooling loop, however the design of an external cooling loop is out of the scope of this thesis and is presented as a useful metric for the performance of the cooling design. The results of the DOE for each run and output parameter are shown in Table 5.8.

Table 5.8: CFD results of the Taguchi L9($3^4$) orthogonal array.

| Run # | Maximum Magnet Temperature (°C) | HTC ($W/m^2K$) | Pressure Drop (kPa) | Fluid Friction Loss (W) |
|---|---|---|---|---|
| #1 | 116.1 | 5635 | 102.1 | 47.3 |
| #2 | 111.1 | 5683 | 189.5 | 82.5 |
| #3 | 101.8 | 5021 | 302.5 | 127.8 |
| #4 | 103.4 | 10621 | 45.8 | 149.6 |
| #5 | 102.2 | 5203 | 22.6 | 146.6 |
| #6 | 107.3 | 8561 | 32.0 | 112.5 |
| #7 | 100.9 | 7201 | 23.9 | 229.2 |
| #8 | 104.7 | 11856 | 23.2 | 216.4 |
| #9 | 103.8 | 9198 | 7.6 | 196.0 |

In order to measure the impact of the levels for each factor on a particular output, main effects plots were produced and are displayed in Fig. 5.7. The plots indicate the effects of the levels for each parameter on the performance of the design through the S/N ratio values. "Smaller the better" is the goal for the maximum magnet temperature, pressure drop, and fluid friction loss, whereas "larger the better" is the goal for the HTC. Higher values indicate a positive impact on the performance and is the desired outcome regardless of the goal. As previously mentioned, minimizing the

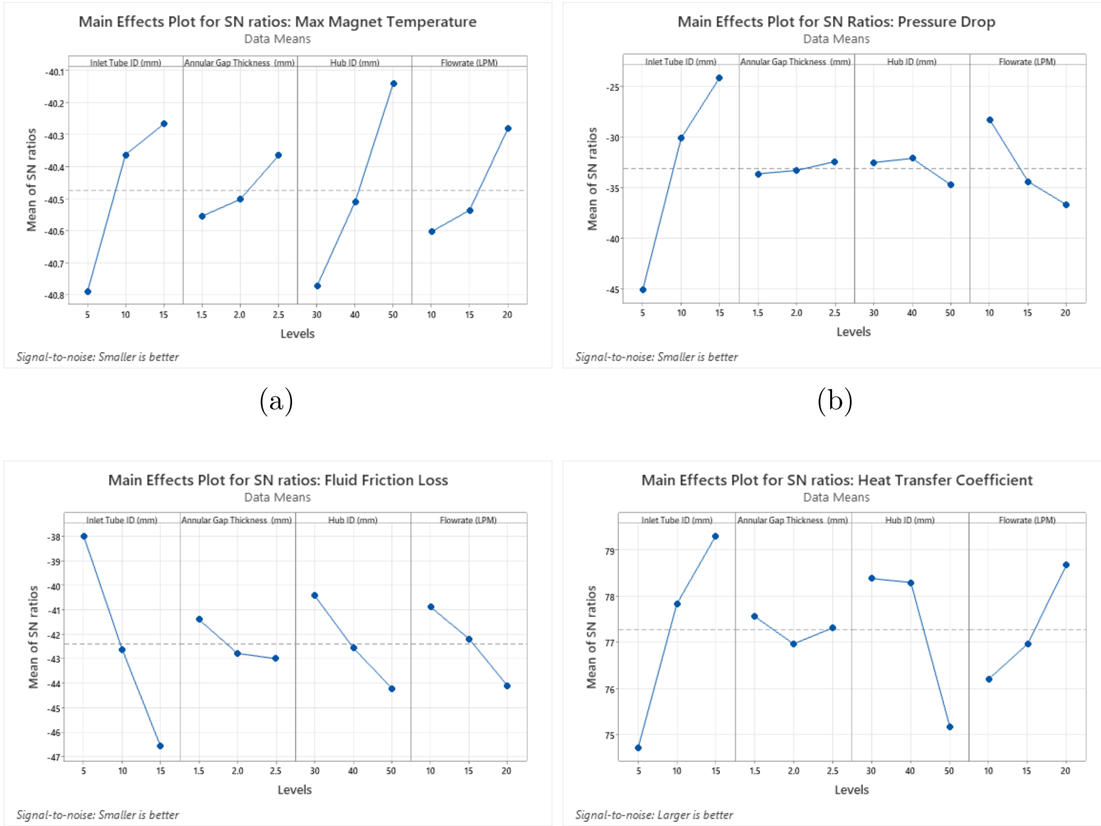


(a) (b)

(c) (d)

Figure 5.7: Main effects on S/N ratios from Taguchi DOE for: a) Maximum magnet temperature, (b) Pressure drop, (c) Fluid friction loss, (d) Heat transfer coefficient.

maximum magnet temperature is the primary outcome of the Taguchi DOE in this case, however the pressure drop, HTC, and fluid friction loss are important for future design iterations. Therefore, further understanding the effects of each factor on each of the less critical output parameters is required.

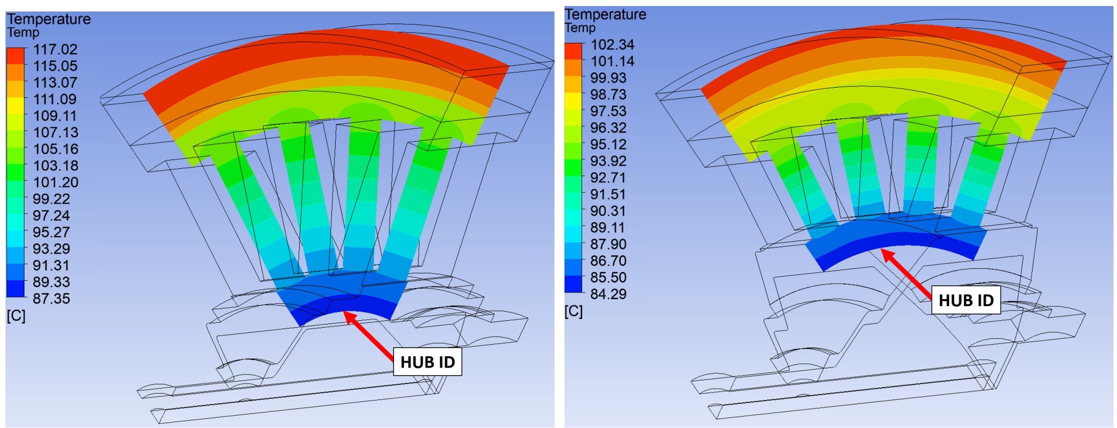


(a) (b)

Figure 5.8: Temperature distributions in the cross section for the solid domain (rotor hub, magnets, and carbon fiber sleeve) at the middle of the hub in (a) run 1, and (b) run 3.

### 5.6.3 In-Depth Analysis of Taguchi Runs

Among the factors examined in the DOE, the hub ID was expected to have the most significant impact in reducing magnet temperatures. Increasing the hub ID reduces the thickness of solid material between the coolant and the magnets, which results in a lower thermal resistance and lower magnet temperatures. The temperature distribution of the solid domain at the cross section at the axial midplane of the hub in run 1 and run 3 is shown in Fig. 5.8. Understanding the impact of the levels within the other factors on each output parameter is less obvious. Since a full factorial DOE was not conducted, it is not possible to observe differences in the flow when changing only one of the four factors since any two experiments within a L9($3^4$) Taguchi array will only share the same levels for a maximum of 2 factors. It is still useful to try to understand differences in the results by closely analyzing the runs of the DOE.

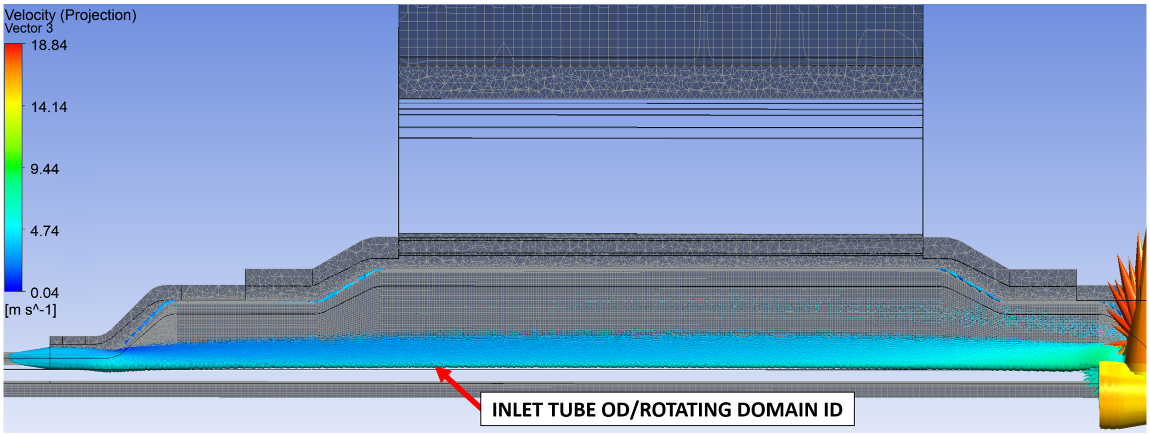


Figure 5.9: Velocity vector plot showing the distribution of the velocity component tangential to the section plane. Vector sizes are scaled to the magnitude of the velocity component and exaggerated to improve visibility of the low-velocity vectors within the domain.

Runs 1 and 3 are first compared to observe differences in the flow field mainly due to the hub ID without changing the inlet tube ID. The annular gap and flowrate also differ between the two runs, however trends still emerge that appear to be less dependent on these two factors. The flow velocity was highest at the OD of the inlet tube, or the ID of the rotating domain, as shown in the vector plot in Fig. 5.9. The vectors within the plot are tangential to the section plane, scaled to the tangential velocity magnitude, and exaggerated to show the relative difference between the flow velocities around the inlet tube and within the rest of the rotating domain. The presence of small, nearly invisible vectors within the rotating domain away from the OD of the inlet tube indicates that the in-plane velocity component of the flow is far lower than the region adjacent to the OD of the inlet tube. Axial components of the velocities around the inlet tube OD exceed 1.5 m/s and depend on the levels for each factor in the experiment. The same component of the velocity towards the hub ID does not exceed 0.3 m/s.

In order to visualize the flow structures in the hollow shaft rotating domain between runs 1 and 3, a similar vector plot showing velocities tangential to the slicing plane with normalized vector sizes is shown in Fig. 5.10 and Fig. 5.11. As expected, on the sloped surfaces within the the shaft, the centrifugal forces carry fluid towards the larger diameter sections along the walls, which can be seen in the edges of the fluid domain in Fig. 5.10b) to Fig. 5.11c) and Fig. 5.11e).

For heat to be effectively transferred from the hub to the coolant, the fluid must be circulated from the OD of the inlet tube, where a majority of the fluid flows in the rotating domain, to the surfaces of the shaft. A circulating flow structure is present in every Taguchi run and varies slightly between runs mainly due to the hub ID and inlet tube ID, the latter of which is shown later in this section. In the plots from run 1 in Fig. 5.10, a band of fluid flow moving in the opposite direction to the main flow can be seen, which is called reversed flow for brevity. This band of reversed flow begins adjacent to the annular gap in both runs, as shown in Fig. 5.10b), circulating coolant between the walls of the shaft and the fast moving fluid at the annular gap. The reversed flow meets fluid from the inlet tube moving in the direction of the mean flow in a thin region adjacent to the wall at a point along the length of hub ID which is seen in Fig. 5.10c). The band of reversed flow continues, now detached from the hub ID, towards the inlet side of the rotating domain where mixes with the flow from the inlet tube in a number of vortices generated from the inlet flow impinging on the A-side of the shaft, which can be seen in Fig. 5.10d), completing the large circulating

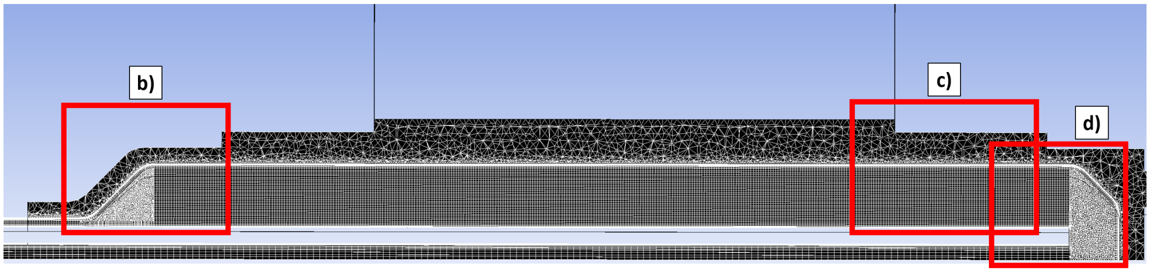


(a)

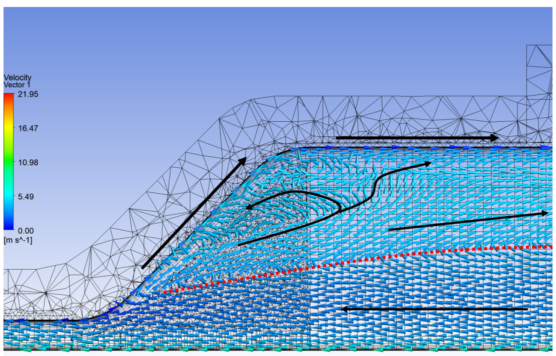


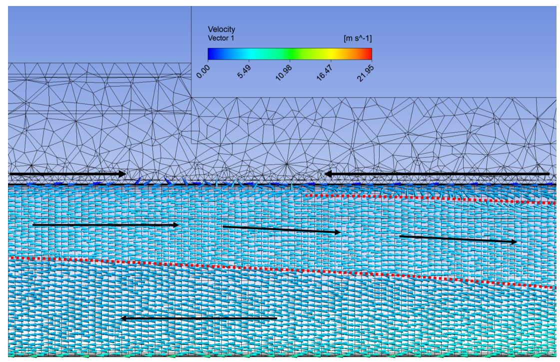


(b) (c)

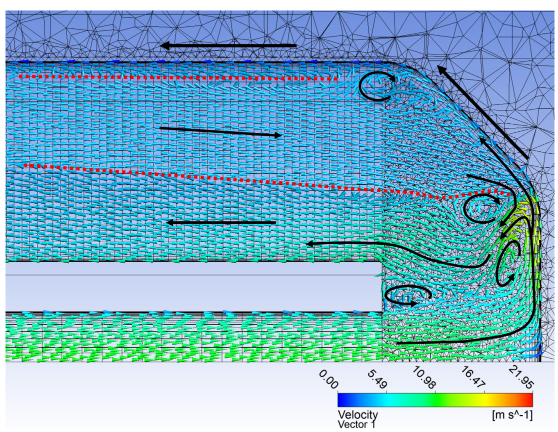


(d)

Figure 5.10: a) Cross section from run 1 identifying locations of velocity vector plots in b)-d) with normalized vector sizes showing velocities tangential to the section plane. Black arrows highlight flow structures and red dotted lines show borders between bands of flow moving in opposing directions.

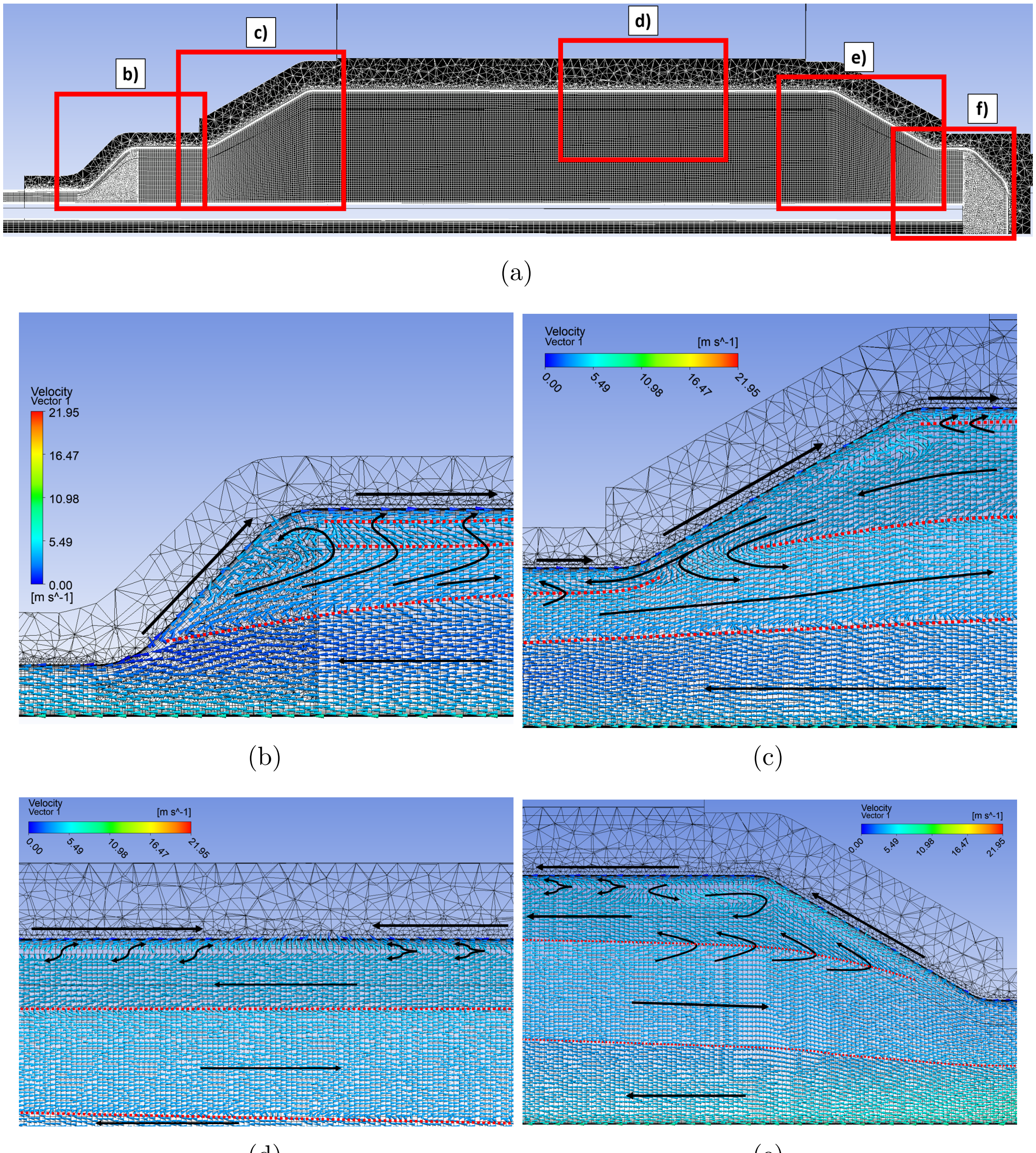


(a)

(b)

(c)

(d)

(e)

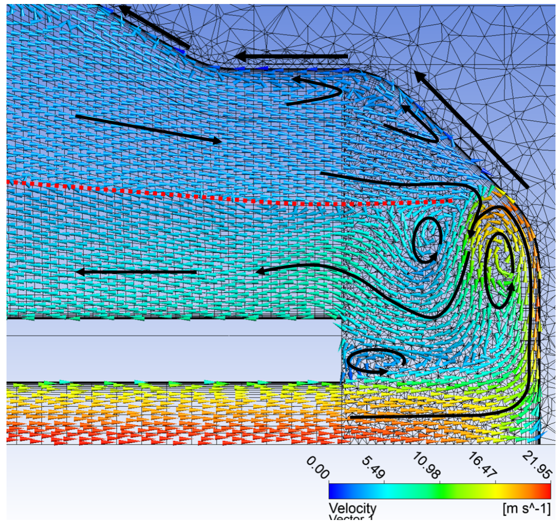


(f)

Figure 5.11: a) Cross section from run 3 identifying locations of velocity vector plots in b)-f) with normalized vector sizes showing velocities tangential to the section plane. Black arrows highlight flow structures and red dotted lines show borders between bands of flow moving in opposing directions.

flow structure throughout the rotating domain.

Similar flow structures are seen in the plots from run 3, however the presence of the additional step in inner walls of the shaft introduces more in-plane circulating flows. The sloped surface between the hub ID and the adjacent diameter underneath the bearing at the B-side of the shaft is seen in Fig. 5.11c). The band of reversed flow is in the same region, extending slightly into the larger diameter section of the rotating domain, however 2 additional bands of fluid can be seen in Fig. 5.11c), Fig. 5.11d), and Fig. 5.11e). Adjacent to the main reversed flow is a band of fluid flowing in the direction of the mean flow towards the B-side of the rotating domain, followed by a thin section of reversed flow at the hub ID wall. As with the flow field in run 1, the reversed flow merges with coolant moving in the direction of the mean flow at the wall, however this merging occurs at a different location from run 1.

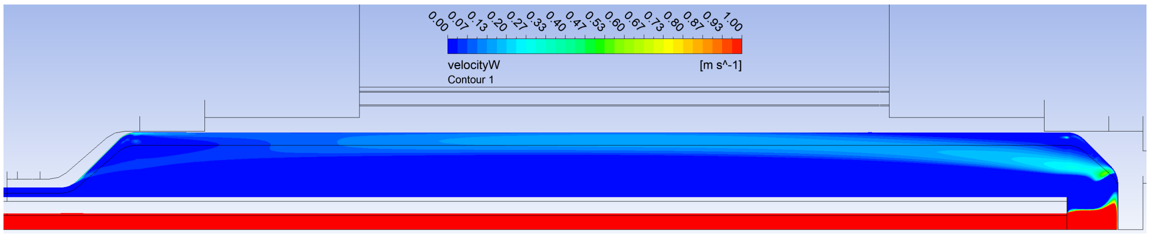


(a)

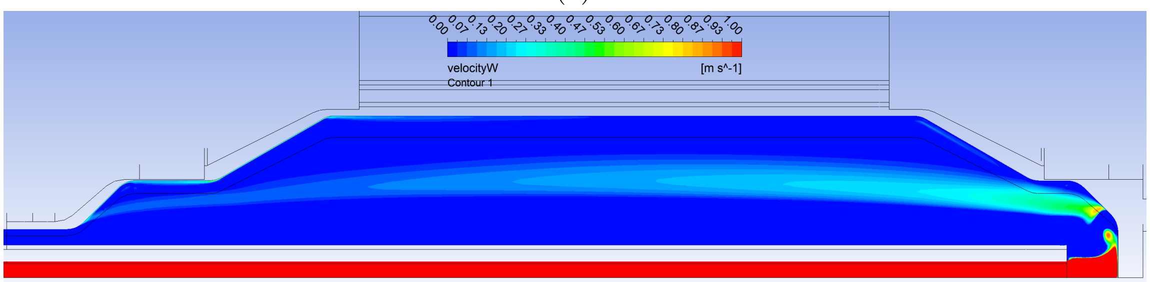


(b)

Figure 5.12: Contour plots of the w-component of the velocity distribution in the fluid domain in a) run 1, and b) run 3. Positive velocities indicate flow moving from left to right.

The regions of reversed flow can also be visualized with a contour plot showing the w-component of the velocity, which is in the axial direction, along the same plane which is seen in Fig. 5.12 for run 1 and run 3. Since the w component of the velocities are relatively low, the scale of the plot was changed to show velocities between 0 m/s and 1 m/s where positive velocities indicate flow away from the direction of the outlet in the axial direction and negative velocities indicate flow towards the outlet in the rotating domain. The plots show that the w component of the velocities is slightly higher in run 3 than in run 1, however this may be due to the increase in flowrate to 20 LPM in run 3 from 10 LPM in run 1. This is also the cause of the stronger vortical structures and velocity magnitudes at the inlet region of the rotating domain seen in run 3 (Fig. 5.11f)).

Contour plots of the HTC and shear stress along the inner walls of the shaft were also gathered to determine the differences in these parameters due to the varying hub ID. As shown in Fig. 5.13, the HTC distribution throughout the walls of the shaft does not vary greatly. The largest difference in the distribution is within the sloped surfaces adjacent to the hub ID where the HTC is lower than that of the hub ID. This results in a slightly lower area averaged HTC in run 3 when compared to run 1, however the larger heat transfer surface area in the geometry used in run 3 accounts for the difference in HTC, helping reduce magnet temperatures. The shear stresses at the inner surfaces of the shaft, which are responsible for the fluid friction losses, are shown in Fig. 5.14. The shear stress distributions do not vary significantly between run 1 and run 3, however the sloped surfaces adjacent to the hub ID in run 3 experience higher average shear stresses. These regions of slightly higher shear stresses coupled with the increased surface area of the shaft walls in run 3 contribute to the higher fluid friction losses.

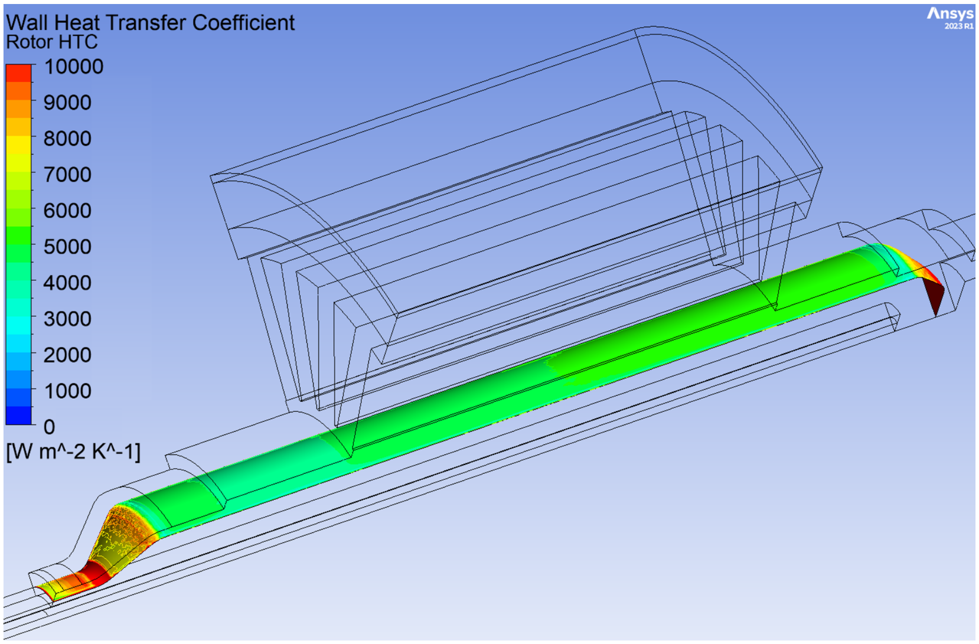


(a)

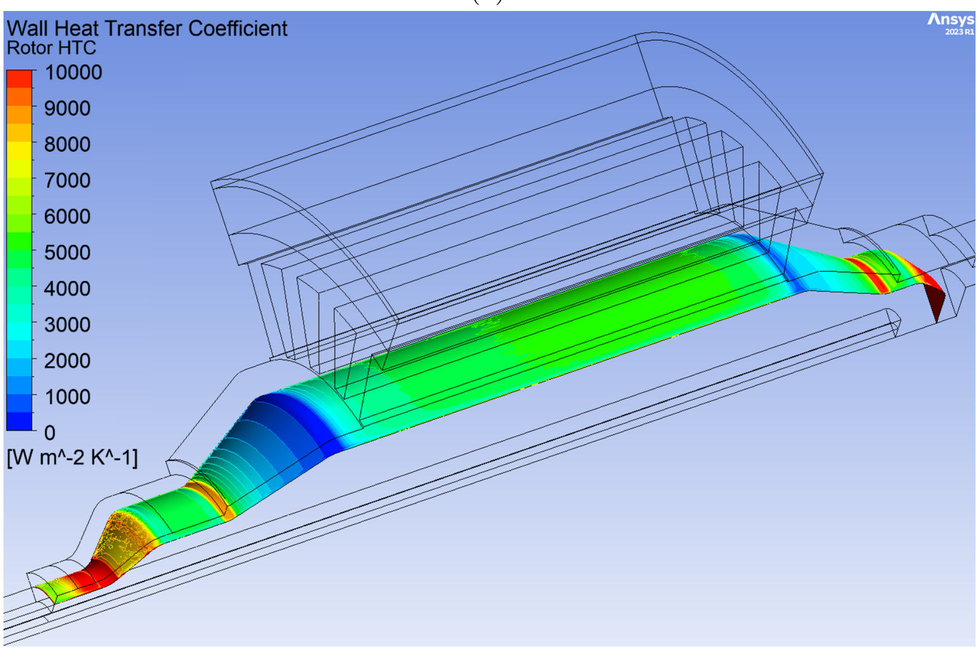


(b)

Figure 5.13: Contour plots of the HTC at the shaft walls in a) run 1, and b) run 3.

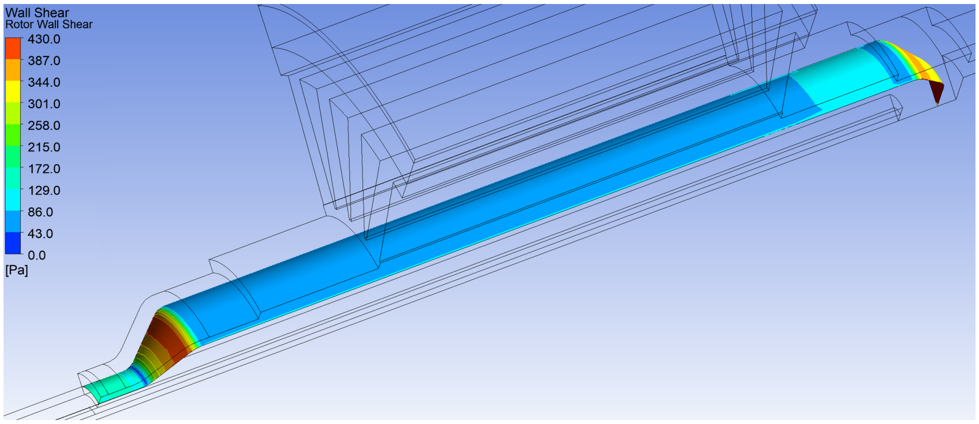


(a)

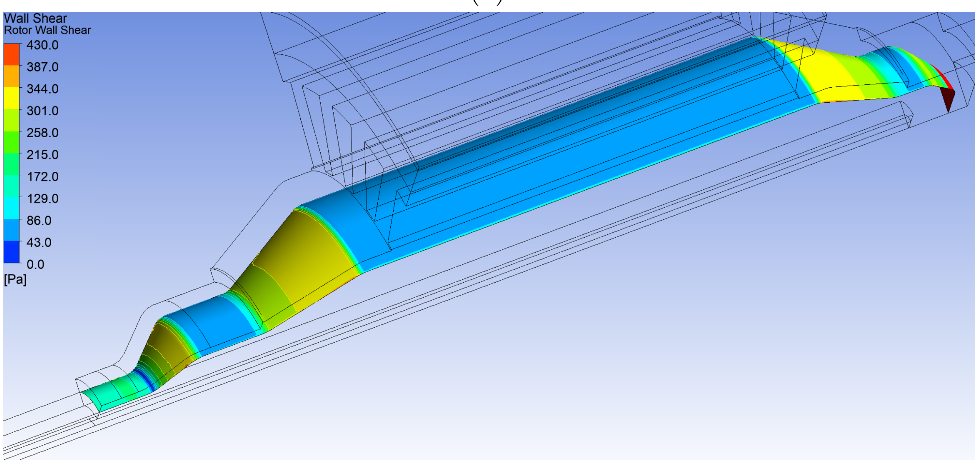


(b)

Figure 5.14: Contour plots of the shear stress distribution at the shaft walls in a) run 1, and b) run 3.

Comparisons were also made between run 2 and run 9 to observe the effects of changes in the inlet tube diameter while maintaining a constant hub ID since the inlet tube diameter appeared to greatly affect the pressure drop, fluid friction losses, and HTC. The S/N plots in Fig. 5.7 show that the annular gap thickness had the smallest effect on these output parameters, therefore the observations made in the flow field, shear

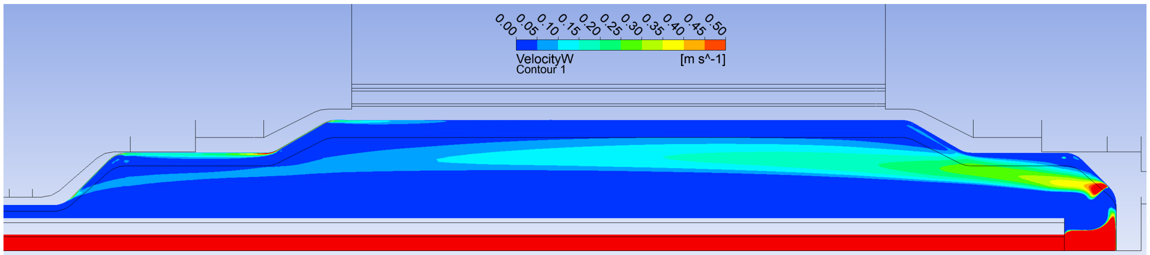


(a)

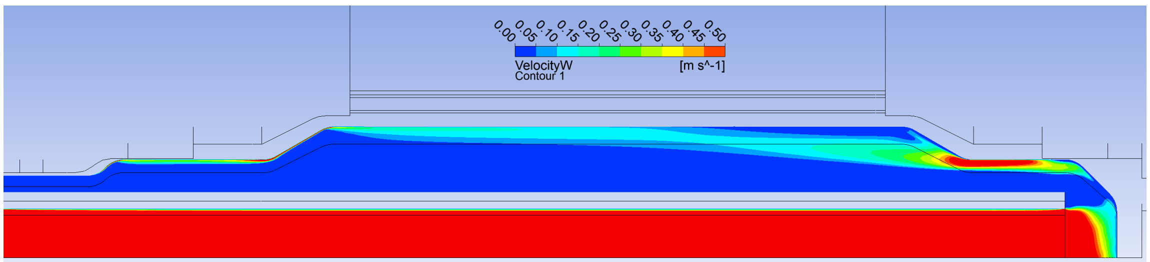


(b)

Figure 5.15: Contour plots depicting the w-component of the velocity distribution in the fluid domain in a) run 2, and b) run 9. Positive velocities indicate flow moving from left to right.

stress, and HTC should not be significantly affected by difference in the annular gap thickness between the two runs. The impact of the flowrate differences is more significant, however the contour plots of the w component of the velocity in run 2 shown in Fig. 5.15a) closely resembles that of the one seen in run 3 shown in Fig. 5.12b) in that the band of reversed flow is roughly the same shape and in the same location with slightly lower velocities throughout the band, likely due to the difference in the flowrate between run 2 and run 3. A similar contour plot of the w component of the velocity in run 9, shown in Fig. 5.15b), presents a slightly different flow structure where the band of reversed flow begins further upstream, compared to run 1, run 2, and run 3, and stays attached to the hub ID throughout half of its

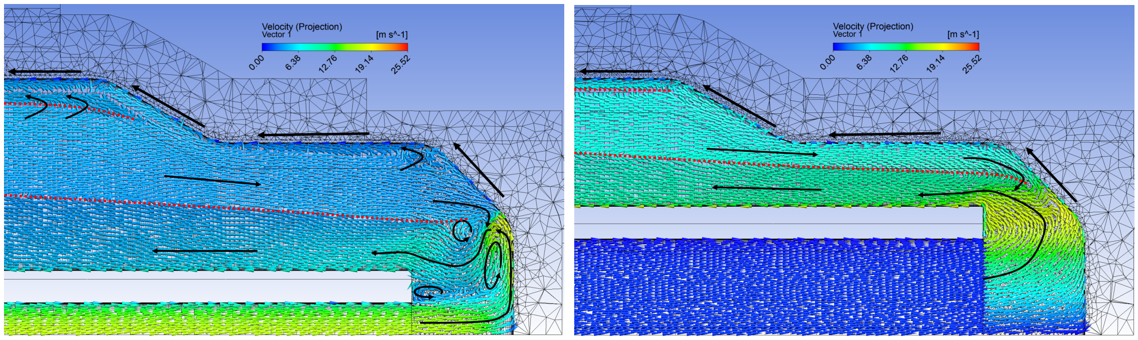


(a) (b)

Figure 5.16: Velocity vector plots with normalized vector sizes showing velocities tangential to the section plane at the A-side of the rotating domain in a) run 2, and b) run 9. Black arrows highlight flow structures and red dotted lines show borders between bands of flow moving in opposite directions.

length on the B-side of the shaft before detaching from the surface. The band of reversed flow reattaches to the shaft surface in the adjacent surfaces on the A-side of the domain. When compared to the plot in Fig. 5.15a), the reversed flow at the inlet side of the rotating domain is pushed against the walls of the shaft to prevent restricting the flow that moves at the ID of the rotating domain as shown in Fig. 5.16. It can also be seen that the flow within the inlet region of the rotating domain in the plot from run 9 (Fig. 5.16b)) is far less vortical when compared to run 2 (Fig. 5.16a)) even though the flowrate in run 9 is 1.5 times that of run 2. Since the inlet tube diameter in run 9 is three times that of run 2, the fluid velocity within the inlet tube is lower. The lower flowrate in run 9 coupled with the aforementioned dimensional differences results in a weaker impinging effect at the A-side of the shaft, reducing the vortical structures in this region.

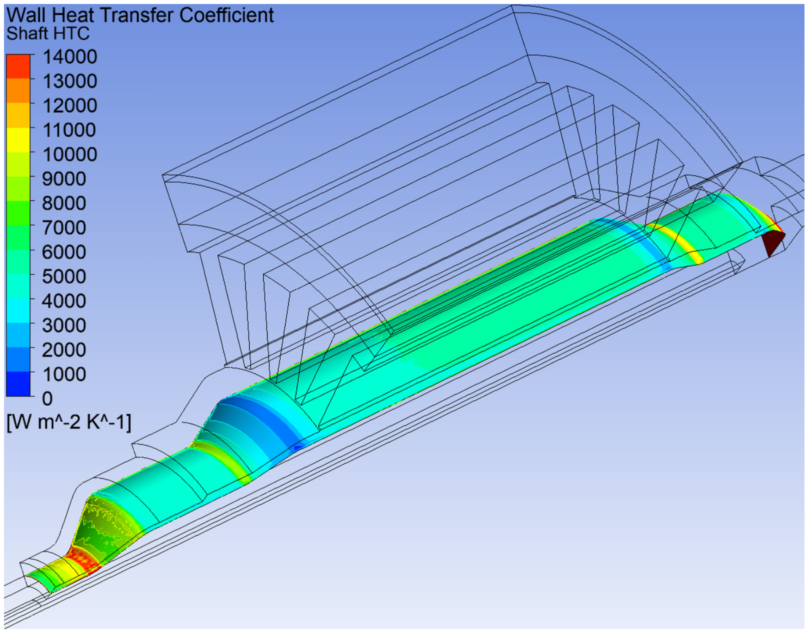


(a)

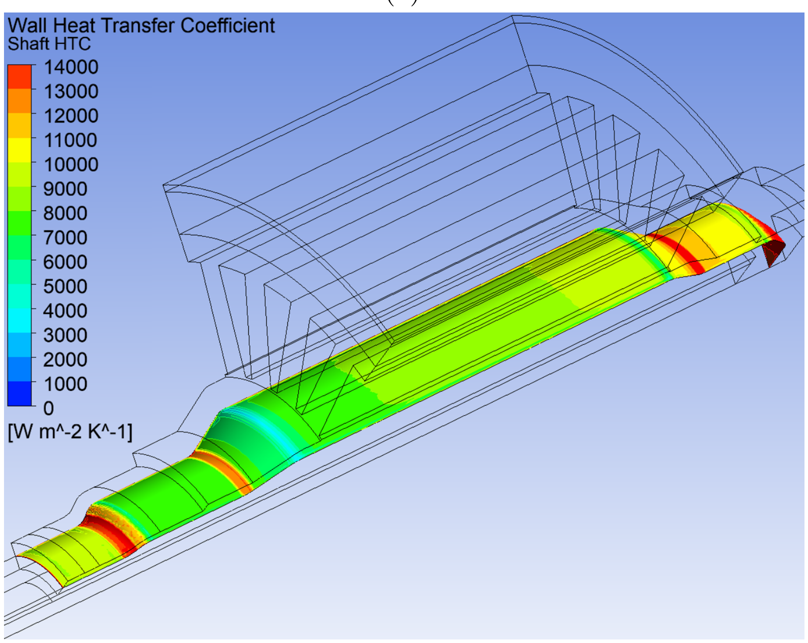


(b)

Figure 5.17: Contour plots of the HTC at the shaft walls in a) run 2, and b) run 9.

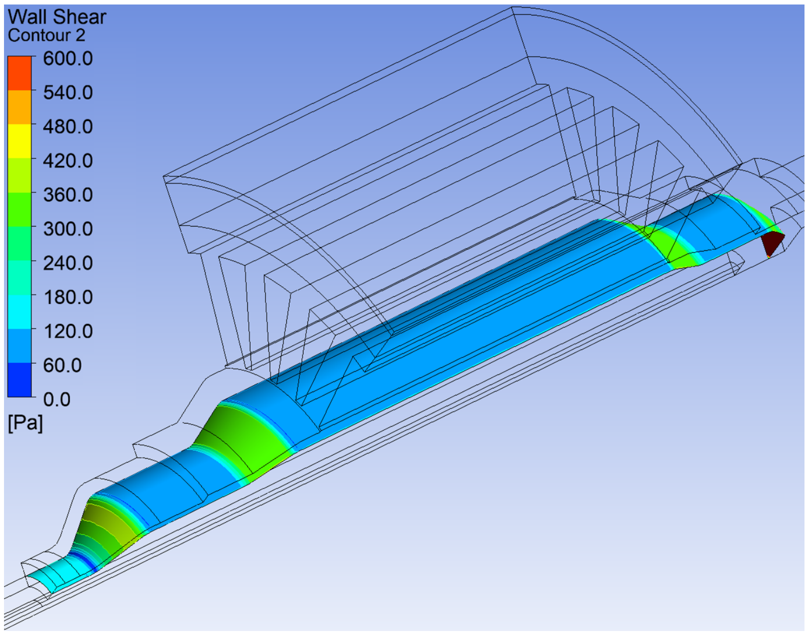


(a)

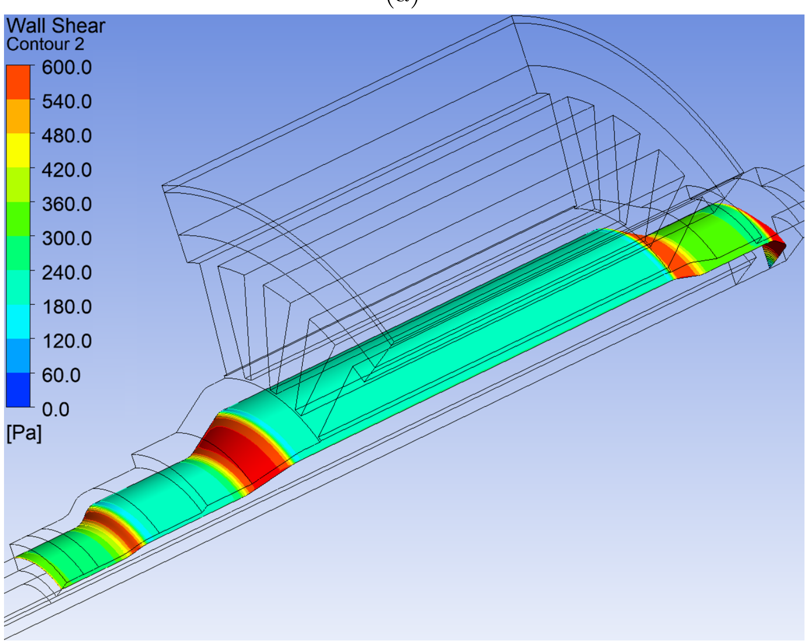


(b)

Figure 5.18: Contour plots of the shear stress distribution at the shaft walls in a) run 2, and b) run 9.

The HTC and shear stress contour plots on the shaft surfaces for run 2 and run 9 are shown in Fig. 5.17 and Fig. 5.18 respectively. It is clear from the plots that run 9 shows higher HTC values throughout all the surfaces of the shaft relative to run 2. Similarly, the shear stresses on the shaft surfaces are universally higher in run 9. Similar to what is observed when comparing run 1 and run 3, the change in flowrate from 5 LPM in run 2 to 10 LPM in run 9 has a far smaller effect on the HTC and fluid friction losses when compared to increasing the inlet tube ID from 5 mm to 15 mm. This can be clearly seen in the main effects plots in Fig. 5.7.

## 5.7 Optimized Rotor Cooling Design

Using the levels with the highest S/N ratios for each factor from the main effects plots for the maximum magnet temperature in Fig. 5.7a), an optimal rotor design can be made to minimize the maximum magnet temperature. According to Fig. 5.7a), such a design uses a 15 mm inlet tube ID, 2.5 mm annular gap thickness, 50 mm hub ID, and 20 LPM flowrate. The results showing each of the output parameters of the optimal design are shown in Table 5.9.

Table 5.9: Output parameters of the optimized rotor cooling design simulation.

| Output Parameter | Value |
|---|---|
| Maximum Magnet Temperature | 99.5°C |
| Heat Transfer Coefficient | 8560 W/m$^2$K |
| Pressure Drop | 33.2 kPa |
| Fluid Friction Loss | 292.2 W |

The output parameters follow the trends seen in the main effects on S/N ratios plots in Fig. 5.7. The pressure drop is greatly affected by the inlet tube diameter, as is shown in Fig. 5.7b), which results in a relatively low pressure drop when using the largest inlet tube ID compared to runs 1 to 3 in the Taguchi DOE each of which experienced relatively high pressure drops. The fluid friction losses are also the highest of any simulation since the optimal levels for minimizing magnet temperatures were expected to yield the highest fluid friction losses according to the main effect plot for these losses in Fig. 5.7c). The HTC is higher than four of the runs in the DOE which coincides with the trends from the S/N ratio plots. The positive effect on the HTC by increasing in the inlet tube diameter and flowrate outweighs the negative effects on the HTC from the increase in hub ID and annular gap. This results in a higher HTC than the first 3 runs, which used the smallest inlet tube diameter, but a lower HTC than runs that used a larger inlet tube diameter with a smaller hub ID. The optimal rotor design resulted in a final maximum magnet temperature of 99.5°C, which is 1.4°C and 16.6°C lower than the lowest and highest maximum magnet temperatures, respectively, in the Taguchi DOE. This minimal reduction in magnet temperature from the lowest value seen in the DOE is somewhat expected since the largest contributing factors to the magnet temperature are known to be the hub ID and stationary tube diameter. Run 7 uses the optimal values for these two factors, resulting in magnet temperatures that are close to the optimal results. Additionally, the range of magnet temperatures in the DOE is not very large, with a total range of 15.2°C in the DOE, therefore a significant reduction of magnet temperatures was not expected.

The vector plots are not shown for the optimized design since they closely resemble the general flow structures seen in run 9. A contour plot of the w component of the velocity in the optimized design is shown in Fig. 5.19. The reversed flow seen in this figure is significantly larger than that seen in run 9. This is likely due to the larger hub ID which allows the band of reversed flow to extend further outward radially while the increased flowrate further encourages in-plane circulation of the flow between the shaft walls and inlet tube OD within the rotating domain.

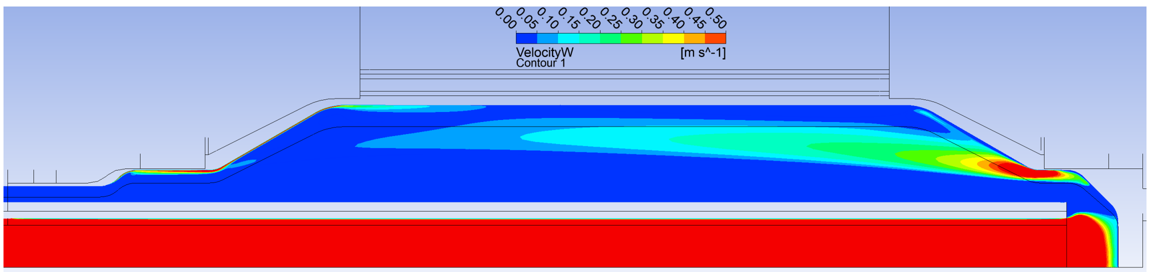


Figure 5.19: Contour plot depicting the w-component of the velocity distribution in the fluid domain of the optimized rotor cooling design. Negative velocities indicate flow moving from left to right.

The HTC and shear stress contour plots are shown in Fig. 5.20 and Fig. 5.21 respectively. The contour plots closely resemble that of run 9, shown in Fig. 5.17b) and Fig. 5.18b). Lastly, the temperature contour plots for the solid domain and magnet array are shown in Fig. 5.22 and Fig. 5.23, respectively. As expected, the magnet temperature mainly varies in the radial direction with little variation in the axial direction since adiabatic boundary conditions were applied to the the outer faces of the rotor hub and magnets. The temperature contours of the full solid domain in Fig. 5.22 reveal very high temperatures in the A-side of the shaft around the spline, seal, and the bearing seat. These high temperatures can be attributed to the adiabatic boundary conditions on the shaft surfaces and the highly conservative estimation of the bearing losses dissipated into the shaft. Additionally, the seal dissipates heat into the spline end of the shaft, well away from the coolant, further contributing to the high temperatures in this region. While the temperatures seen are unrealistic, further investigation into the operating condition of the motor is required to apply the proper boundary conditions in the A-side of the shaft, or the cooling channel may need to be extended further towards the spline to dissipate the heat in future revisions of the design.

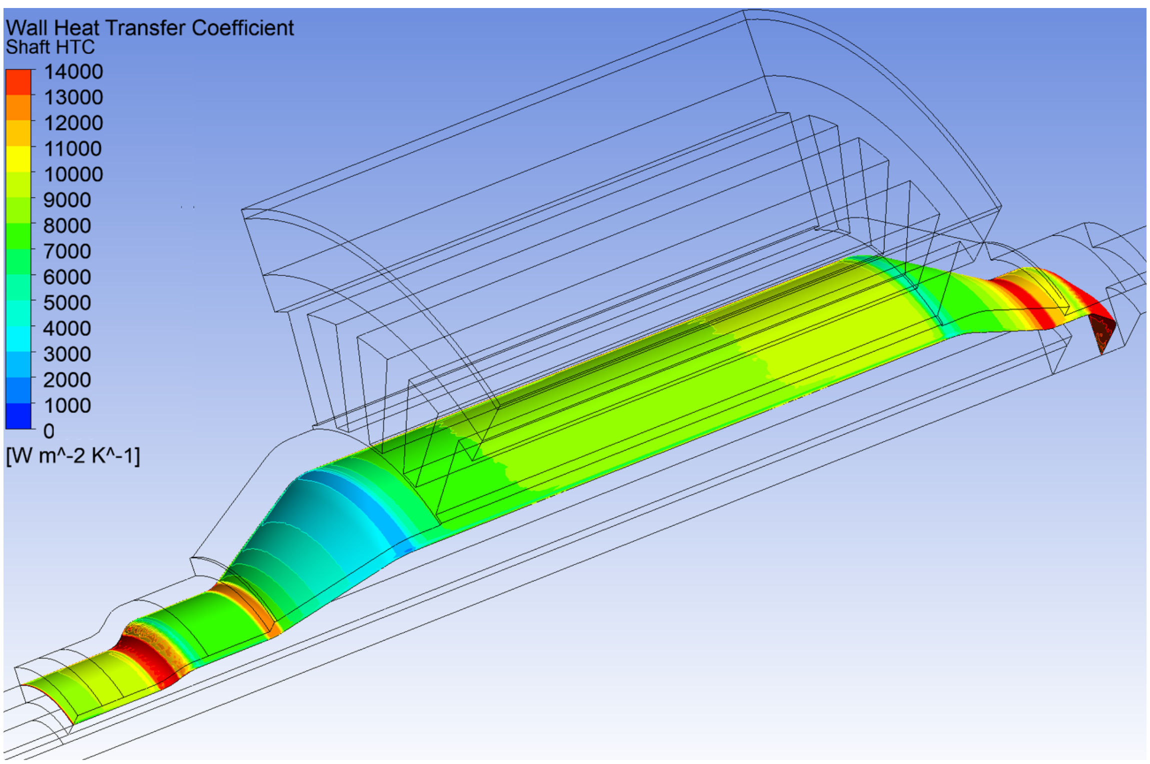


Figure 5.20: Contour plot of the HTC at the shaft walls of the optimized rotor cooling design.

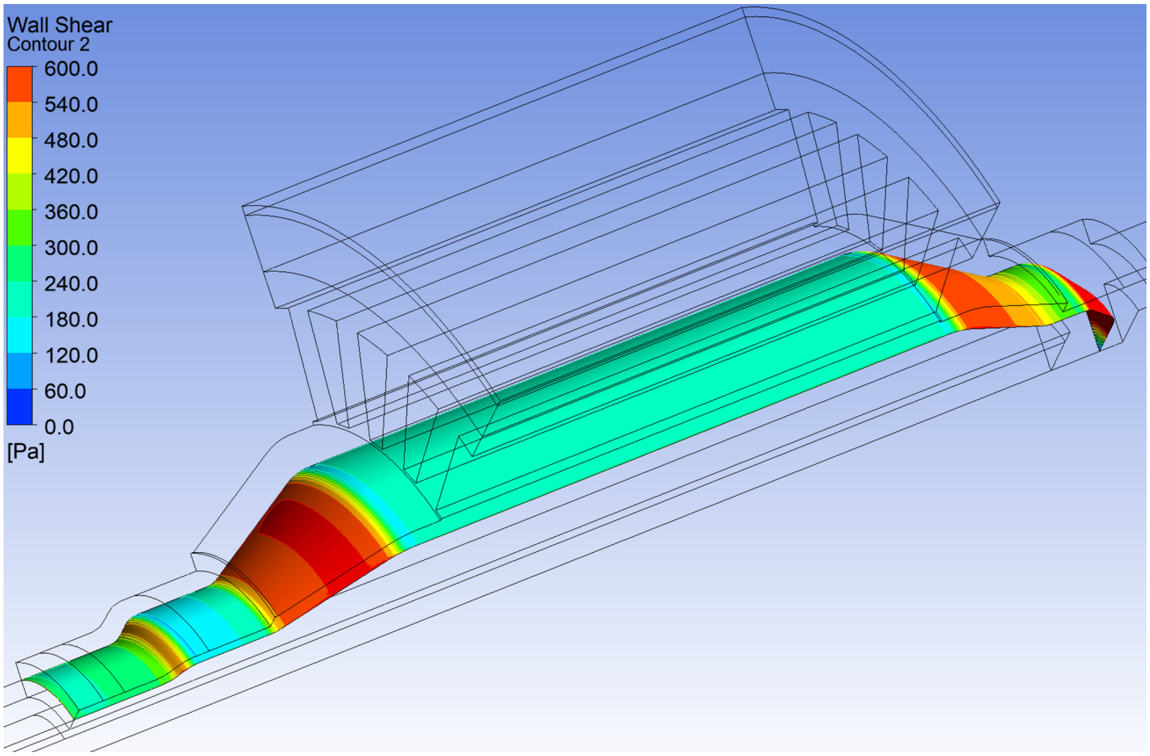


Figure 5.21: Contour plot of the shear stress distribution at the shaft walls of the optimized rotor cooling design.

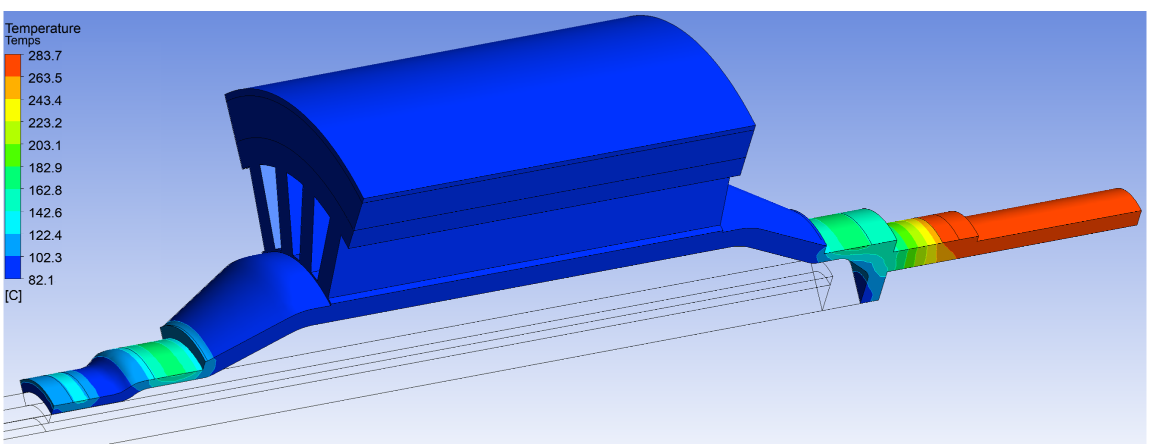


Figure 5.22: Temperature contour plot of the solid domain in the optimized rotor cooling design.

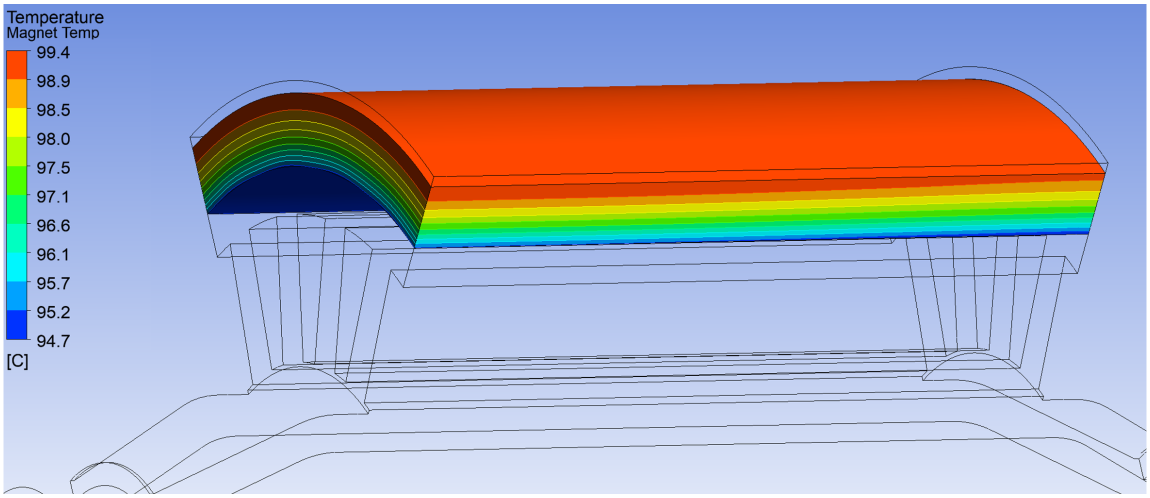


Figure 5.23: Temperature contour plot of the magnet array in the optimized rotor cooling design.

## 5.8 Chapter Summary

This chapter presents the process of utilizing the Taguchi method and thermal CFD analysis for optimizing the design of the rotor cooling system. The theory related to the CFD analysis was first discussed, highlighting the relevant equations and discussing the available turbulence models with justification for the $k - \omega$ SST model chosen for the analysis. The simulation setup was shown, providing motor losses, geometry simplifications to minimize computational load, boundary conditions, and meshing for the final simulations. The mesh independence study presented in this chapter validated the mesh size used for the Taguchi DOE and final design. The Taguchi method for design optimization was then introduced before presenting the DOE for the optimization of the proposed rotor cooling design. Analysis of the results was conducted using the S/N ratio plots with additional in-depth analysis of the CFD results provided to better understand the effects of different levels within each factor on the flow structure and output parameters of the experiments. An optimal design to minimize the magnet temperature was presented, achieving a 1.4°C and 16.6°C drop from the lowest and highest temperatures seen in the DOE respectively, while achieving acceptable pressure drop values and relatively high fluid friction losses. The rotor cooling design was shown to be effective at maintaining magnet temperatures well under the demagnetization temperature of 180°C, showing that there is significant headroom in the electromagnetic design of the motor with the ability to dissipate higher losses than those presented in this chapter.

# Chapter 6

# Conclusions and Future Work

## 6.1 Conclusions

With the recent push towards aerospace propulsion electrification, electric motors need to be designed with higher power densities and robust thermal management to dissipate the losses in inherently smaller packages. This thesis presented the design of a high-speed power dense radial flux PM motor for aerospace applications.

The thesis first introduces the challenges for aerospace propulsion electrification, hybridization architectures to bridge the gap between conventionally powered and fully electric aircraft, and the current landscape of aerospace electrification with particular interest in motors developed for aerospace propulsion and aircraft electrification projects. From the review, it is clear that a large focus is placed on fully electric propulsion for very small turboprop, GA, and business jet aircraft. While it may be viable to achieve full electrification for such aircraft, it is currently difficult to scale the technology for larger single-aisle narrowbody aircraft and larger. This is due, in large part, to inadequate power density and energy density from current electrical propulsion systems and energy storage systems, respectively. That said, there is a push for next generation electric motors for aerospace to take advantage of new design and manufacturing technologies to help increase power density and close the gap to conventional propulsion systems. Companies like H3X, Helix, and Evolito Ltd. are among the leaders in power density for aerospace propulsion motors available today. The motors presented in this thesis serve as a useful comparison to the motor proposed in this thesis.

The discussion of the proposed motor focuses on the author's contributions to the motor design, more specifically the mechanical integration of the stator lamination stack and windings, and the mechanical and thermal design of the rotating assembly. The use of additive manufacturing for the housing and end plate in the stator assembly helped to reduce part count and weight, leading to a higher power density. However, since an equivalent conventionally manufactured design was not made, the weight savings through the use of additive manufacturing cannot be quantified. The stator potting process discussed in this thesis significantly aids in dissipating heat from the slots and end windings to the stator cooling jacket design within the housing. One downside from this process is the additional weight of the epoxy when compared to other impregnation processes.

The literature review exploring the design of rotors in high speed radial flux motors for traction applications provided a number of thermal management solutions and design principles used to design the rotating assembly of the proposed motor. Although various air and liquid cooling designs are discussed, an integrated stator and rotor liquid cooling design was ultimately chosen for the proposed motor. This is because the stator cooling jacket design was predetermined and the choice was made to integrate the stator and rotor cooling into a single loop rather than using additional external components to cool the rotor in a separate cooling loop or accepting the high possibility of high noises from a self ventilated air cooled rotor.

The integrated shaft, which is only possible because of the Halbach array, introduced complications when it comes to manufacturing as a result of the recirculating hollow shaft cooling design. The design shown in this thesis must be split and machined as two separate parts before welding, with the split being placed on the B-side of the shaft to minimize the torque at the weld joint. The critical speed is minimized by reducing the weight in the hub through the use of through-holes and by moving the bearings in as far as possible given the largest hub ID size available in the rotor cooling optimization study. The use of 35 mm bearings also helps to increase the critical speed at the cost of higher generated losses at 20 kRPM. This compromise was accepted for this initial revision of the motor as it is subject to mechanical analysis, which will help determine whether smaller bearings may be used, further improving the design. Oil jet lubrication is chosen to lubricate and cool the bearings due to its reliability and the ability to dissipate heat, adjust flowrate, and number of nozzles for each bearing.

Thermal analysis of the rotor cooling design shows that the design is able to effectively cool the magnets well within the 180°C demagnetization temperature specified for the magnet material. The Taguchi method is used to create a DOE to optimize the rotor cooling design with the main goal of minimizing magnet temperatures. The optimization study successfully minimized the maximum magnet temperature given the factors and levels studied in the DOE, resulting in a maximum magnet temperature of 99.5°C in the optimized rotor design. The analysis also observed the pressure drop, churning loss, and HTC. The trends in these values are presented in this thesis to provide useful data for future revisions of the motor and for a full system design. The resulting magnet temperatures also show that the rotor cooling systems is capable of dissipating higher losses from the magnets which can be generated from increasing the power output of the motor.

## 6.2 Future Work

The motor proposed in this thesis can be further improved with additional analysis and experimentation. Recommendations for future work to revise the motor design and validate the results are as follows:

1. Experiments should be carried out to validate the results from the CFD analysis of the recirculating hollow shaft cooling design.

2. Experiments should be done to determine the optimal oil flowrate and generated losses for the given preload in the bearing assemblies. Measurements of the losses dissipated through the inner raceway, outer raceway, and oil should be

taken to accurately determine the bearing losses to be considered in the rotor simulations.

3. Mechanical FEA analysis should be carried out on the rotating assembly to ensure that the integrated shaft is capable of handling the stresses from centrifugal forces and vibrations. Vibration analysis should also be conducted to ensure that the critical speeds of the machine are well above the operating speed range of the machine. Smaller bearing sizes should also be investigated to reduce the overall losses in the motor, improving the efficiency.

4. The electromagnetic design may be revised to increase the power output of the motor. While the rotor cooling design may be adequate to handle the higher losses from the magnets, the same cannot be assumed about the stator cooling design. The stator cooling may need to be revised to account for the higher stator and winding losses.

5. Additional factors can be investigated in the rotor cooling design. One example is modification of the shape of the shaft wall on which the inlet tube flow impinges. Wang et. al [129] showed that variations in the shape of the shaft wall at the inlet side of the rotating domain had an effect on the flow structures within the rotating shaft.

6. High temperatures within the A-side of the shaft need to be further investigated and the rotor cooling design may need to be modified to dissipate some of the heat within this region. Due to the conservative approach to the boundary

conditions of the simulations, the temperatures at the A-side of the shaft are higher than what experiments would otherwise show. Although the temperatures may be lower in reality, they still may be high enough to approach or exceed the operating temperature limits of the contact seal on the A-side of the shaft.

7. An alternative rotor cooling design where the coolant moves from the hollow shaft into the hub before spraying onto the end windings from each end of the hub (Fig. 3.2e) is of interest. In this design, the coolant is closer to the magnets and provides additional cooling to the end windings, which may lead to better thermal performance. Such a design would require a significant redesign to the rotor and stator assemblies. Active stator cooling solutions may be explored since the coolant is exposed to the motor cavity, leading to an increase in the thermal headroom for the stator cooling design.

# References

[1] P. Alvarez, M. Satrustegui, I. Elosegui, and M. Martinez-Iturralde, "Review of High Power and High Voltage Electric Motors for Single-Aisle Regional Aircraft," *IEEE Access*, vol. 10, no. September, pp. 112 989–113 004, 2022, ISSN: 21693536. DOI: 10.1109/ACCESS.2022.3215692.

[2] J. Z. Bird, "A Review of Electric Aircraft Drivetrain Motor Technology," *IEEE Transactions on Magnetics*, vol. 58, no. 2, pp. 1–8, 2022, ISSN: 19410069. DOI: 10.1109/TMAG.2021.3081719.

[3] International Civil Aviation Orginization (ICAO). "Future of aviation." (), [Online]. Available: https://www.icao.int/Meetings/FutureOfAviation/Pages/default.aspx (visited on Mar. 18, 2024).

[4] E. Öksüztepe, U. Kaya, and H. Kurum, "A review of conventional and new-generation aircraft starter/generators in perspective of electric drive applications," *Aircraft Engineering and Aerospace Technology*, vol. 95, no. 3, pp. 474–487, 2023, ISSN: 17488842. DOI: 10.1108/AEAT-05-2022-0126.

[5] International Energy Agency. "Are aviation biofuels ready for take off?" (Mar. 2019), [Online]. Available: https://www.iea.org/commentaries/are-aviation-biofuels-ready-for-take-off (visited on Mar. 18, 2024).

[6] General Electric. "Ge90 fan blade receives best of show honors at composites competition." (Oct. 2005), [Online]. Available: https://www.ge.com/news/press-releases/ge90-fan-blade-receives-best-show-honors-composites-competition (visited on Mar. 18, 2024).

[7] EOS GmbH. "Eos metal materials for am." (), [Online]. Available: https://www.eos.info/en-us/metal-solutions/metal-materials#aluminium (visited on Mar. 18, 2024).

[8] Y. Liu, D. Mo, D. Nalianda, Y. Li, and I. Roumeliotis, "Review of More Electric Engines for Civil Aircraft," *International Journal of Aeronautical and Space Sciences*, vol. 23, no. 4, pp. 784–793, 2022, ISSN: 20932480. DOI: 10.1007/s42405-022-00469-0.

[9] J. Brelke Benjamin ad Martinna, "Electric, hybrid, and turboelectric fixed-wing aircraft: A review of concepts, models, and design approaches," *Progress in Aerospace Sciences*, vol. 104, pp. 1–19, 2019. DOI: 10.1016/j.paerosci.2018.06.004.

[10] "Pw100 series type certificate data sheet," European Union Aviation Safety Agency, 2009.

[11] "Airbus a350 series type certificate data sheet," European Union Aviation Safety Agency, 2009.

[12] R. C. Bolam, Y. Vagapov, and A. Anuchin, "A Review of Electrical Motor Topologies for Aircraft Propulsion," *UPEC 2020 - 2020 55th International Universities Power Engineering Conference, Proceedings*, pp. 1–6, 2020. DOI: 10.1109/UPEC49904.2020.9209783.

[13] R. C. Bolam, Y. Vagapov, and A. Anuchin, "Review of Electrically Powered Propulsion for Aircraft," in *Proceedings - 2018 53rd International Universities Power Engineering Conference, UPEC 2018*, 2018. DOI: 10.1109/UPEC.2018.8541945.

[14] A. Kuśmierek, C. Galiński, and W. Stalewski, "Review of the hybrid gas - electric aircraft propulsion systems versus alternative systems," *Progress in Aerospace Sciences*, vol. 141, no. May, p. 100 925, 2023, ISSN: 03760421. DOI: 10.1016/j.paerosci.2023.100925.

[15] E. National Academies of Sciences and Medicine, *Commercial Aircraft Propulsion and Energy Systems Research: Reducing Global Carbon Emissions*. Washington, DC: The National Academies Press, 2016. DOI: 10.17226/23490. [Online]. Available: https://nap.nationalacademies.org/catalog/23490/commercial-aircraft-propulsion-and-energy-systems-research-reducing-global-carbon.

[16] Helix UK. "Spc330 platform." (), [Online]. Available: https://www.ehelix.com/products/spc330-electric-motor/ (visited on Jan. 7, 2024).

[17] Helix UK. "Spc, spm242 platforms." (), [Online]. Available: https://www.ehelix.com/products/spm242-electric-motor/ (visited on Jan. 7, 2024).

[18] Helix UK. "Spx417 platform." (), [Online]. Available: https://www.ehelix.com/products/spx417-electric-motor/ (visited on Jan. 7, 2024).

[19] Helix UK. "Spc, spm177 platforms." (), [Online]. Available: https://www.ehelix.com/products/spm177-electric-motor/ (visited on Jan. 7, 2024).

[20] O'Connor, John. "Transitioning aircraft propulsion from carbon to electrons." (Feb. 2020), [Online]. Available: https://blogs.sw.siemens.com/thought-leadership/2020/02/06/transitioning-aircraft-propulsion-from-carbon-to-electrons/ (visited on Jan. 7, 2024).

[21] "EMRAX Aviation," EMRAX d.o.o. [Online]. Available: https://emrax.com/references/aviation-aerospace/ (visited on Jan. 7, 2024).

[22] Rolls-Royce plc. "'spirit of innovation' stakes claim to be the world's fastest all-electric vehicle." (), [Online]. Available: https://www.rolls-royce.com/media/press-releases/2021/19-11-2021-spirit-of-innovation-stakes-claim-to-be-the-worlds-fastest-all-electric-vehicle.aspx (visited on Jan. 7, 2024).

[23] Airbus SE. "Cityairbus nextgen fully-electric and integrated urban air mobility." (), [Online]. Available: https://www.airbus.com/en/innovation/low-carbon-aviation/urban-air-mobility/cityairbus-nextgen#configuration (visited on Jan. 7, 2024).

[24] Airbus SE. "Airbus partners with magicall to develop the electric motors of cityairbus nextgen." (May 2022), [Online]. Available: https://www.airbus.com/en/newsroom/press-releases/2022-05-airbus-partners-with-magicall-to-develop-the-electric-motors-of (visited on Jan. 7, 2024).

[25] MagniX. "Eaircraft: Hybrid-elektrische antriebe für luftfahrzeuge." (), [Online]. Available: https://www.magnix.aero/ (visited on Jan. 7, 2024).

[26] Safran S.A. "The engineus™ xl electrical motor: From 500kw to 1 mw!" (Mar. 2023), [Online]. Available: https://www.safran-group.com/news/engineustm-xl-electrical-motor-500kw-1-mw-2023-03-23 (visited on Jan. 7, 2024).

[27] Safran S.A. "Engineus." (), [Online]. Available: https://www.safran-group.com/products-services/engineustm (visited on Jan. 7, 2024).

[28] "HPDM-250 Datasheet, Version 1.9," H3X Technologies Inc., Jul. 2023. [Online]. Available: https://h3x.docsend.com/view/d5p3tsrutpxka9pg (visited on Jan. 7, 2024).

[29] "HPDM-1500 Datasheet, Version 1.2," H3X Technologies Inc., Aug. 2023. [Online]. Available: https://h3x.docsend.com/view/d72pvp8q8gnetjm8 (visited on Jan. 7, 2024).

[30] "HPDM-3000 Datasheet, Version 1.0," H3X Technologies Inc., May 2022. [Online]. Available: https://h3x.docsend.com/view/qhmtvj7msq8adrnu (visited on Jan. 7, 2024).

[31] Bauhaus Luftfahrt e. V. "Ce-liner." (), [Online]. Available: https://www.bauhaus-luftfahrt.net/en/research-areas/hybrid-electric-aviation/ce-liner (visited on Jan. 7, 2024).

[32] Safran S.A. "Geneus smart generator." (), [Online]. Available: https://www.safran-group.com/products-services/geneustm-smart-generator (visited on Jan. 7, 2024).

[33] Anton, Frank. "Eaircraft: Hybrid-elektrische antriebe für luftfahrzeuge." (Sep. 2019), [Online]. Available: https://press.siemens.com/global/en/pressrelease/electric-motor-sets-two-speed-records (visited on Jan. 7, 2024).

[34] Siemens Press. "Electric motor sets two speed records." (Apr. 2017), [Online]. Available: https://press.siemens.com/global/en/pressrelease/electric-motor-sets-two-speed-records (visited on Jan. 7, 2024).

[35] "EMRAX 208 Datasheet," EMRAX d.o.o. [Online]. Available: https://emrax.com/wp-content/uploads/2022/11/EMRAX_208_datasheet_A00.pdf (visited on Jan. 7, 2024).

[36] "EMRAX 348 Datasheet," EMRAX d.o.o. [Online]. Available: https://emrax.com/wp-content/uploads/2022/11/EMRAX_348_datasheet_A00.pdf (visited on Jan. 7, 2024).

[37] "YASA 750R Datasheet Rev 11," YASA Ltd., Jun. 2019. [Online]. Available: https://yasa.com/media/2021/05/yasa-750rdatasheet-rev-11.pdf (visited on Jan. 7, 2024).

[38] "YASA P400 R Datasheet Rev 13," YASA Ltd., Jun. 2019. [Online]. Available: https://yasa.com/media/2021/05/yasa-p400rdatasheet-rev-14.pdf (visited on Jan. 7, 2024).

[39] Rotex Electric. "Rotex reb series." (), [Online]. Available: https://www.rotexelectric.eu/products/bldc-motors/reb-series/ (visited on Jan. 7, 2024).

[40] "KM-120 Datasheet V1.4," Kite Magnetics, Sep. 2023. [Online]. Available: https://docs.google.com/presentation/d/1cGHWT8NeaJKBshjU72rAg9CGgS8RmPP6/edit#slide=id.g2477828dc3e_0_60 (visited on Jan. 7, 2024).

[41] "D1500 Datasheet V3," Evolito Ltd. [Online]. Available: https://evolito.aero/media/2022/05/Evolito-D1500-1x3-Datasheet-V3.pdf (visited on Jan. 7, 2024).

[42] "D500 Datasheet V4," Evolito Ltd. [Online]. Available: https://evolito.aero/media/2022/05/Evolito-D500-1Kt-Datasheet-V4.pdf (visited on Jan. 7, 2024).

[43] "MAGiDRIVE Integrated Motor," MAGicALL. [Online]. Available: https://www.magicall.biz/downloads/magidrive-datasheet.pdf (visited on Jan. 7, 2024).

[44] Airbus SE. "Daher, airbus and safran team up to develop ecopulsetm, a distributed hybrid propulsion aircraft demonstrator." (Jun. 2019), [Online]. Available: https://www.airbus.com/en/newsroom/press-releases/2019-06-daher-airbus-and-safran-team-up-to-develop-ecopulsetm-a-distributed (visited on Jan. 7, 2024).

[45] Airbus SE. "Ecopulse demonstrator takes shape ahead of paris airshow." (Jun. 2023), [Online]. Available: https://www.airbus.com/en/newsroom/stories/2023-06-ecopulse-demonstrator-takes-shape-ahead-of-paris-airshow (visited on Jan. 7, 2024).

[46] Airbus SE. "The ecopulse aircraft demonstrator makes first hybrid-electric flight." (Dec. 2023), [Online]. Available: https://www.airbus.com/en/

newsroom/press-releases/2023-12-the-ecopulse-aircraft-demonstrator-makes-first-hybrid-electric (visited on Jan. 7, 2024).

[47] Ampaire Inc. "Eco caravan." (), [Online]. Available: https://www.ampaire.com/vehicles/eco-caravan (visited on Jan. 7, 2024).

[48] Ampaire Inc. "Eco otter." (), [Online]. Available: https://www.ampaire.com/vehicles/eco-otter-aircraft (visited on Jan. 7, 2024).

[49] "APUS i-2 The Zero Emission GA Aircraft," APUS Zero Emission GmbH. [Online]. Available: https://group.apus-aero.com/wp-content/uploads/2023/10/APUS_i-2_Broschuere_20231027_Web.pdf (visited on Jan. 7, 2024).

[50] "APUS i-5 Carrier The Most Eco Friendly Air Cargo Solution," APUS Zero Emission GmbH. [Online]. Available: https://group.apus-aero.com/wp-content/uploads/2023/10/APUS_i-5_Broschuere_20231027_Web.pdf (visited on Jan. 7, 2024).

[51] Diamond Aircraft. "Eda40 information page." (), [Online]. Available: https://www.diamondaircraft.com/en/flight-school-solution/aircraft/eda40/overview/ (visited on Jan. 7, 2024).

[52] University of Stuttgart. "E-genius." (2022), [Online]. Available: https://www.ifb.uni-stuttgart.de/en/research/mannedaircraft/e-genius/ (visited on Jan. 7, 2024).

[53] Eviation. "Eviation alice specifications." (), [Online]. Available: https://www.eviation.com/aircraft/ (visited on Jan. 7, 2024).

[54] Faradair Aerospace. “Faradair beha-m1h product page.” (), [Online]. Available: https://www.faradair.com/ (visited on Jan. 7, 2024).

[55] “UK aerospace boost as Faradair® Aerospace signs new partner consortium,” Faradair Aerospace, Dec. 2020. [Online]. Available: https://www.faradair.com/_files/ugd/3934a0_81be27134c284da0a452c16cd7f42793.pdf (visited on Jan. 7, 2024).

[56] Maeve Aerospace B.V. “Maeve m80 overview.” (), [Online]. Available: https://maeve.aero/ (visited on Jan. 7, 2024).

[57] The National Aeronautics and Space Administration (NASA). “X-57 maxwell.” (), [Online]. Available: https://www.nasa.gov/aeronautics/x-57-maxwell/ (visited on Jan. 7, 2024).

[58] Rolls-Royce plc. “Rolls-royce’s all-electric ‘spirit of innovation’ takes to the skies for the first time.” (), [Online]. Available: https://www.rolls-royce.com/media/press-releases/2021/15-09-2021-rr-all-electric-spirit-of-innovation-takes-to-the-skies-for-the-first-time.aspx (visited on Jan. 7, 2024).

[59] Universal Hydrogen. “Universal hydrogen, magnix, plug power, and aerotec announce hydrogen aviation center at moses lake, washington.” (Aug. 2021), [Online]. Available: https://hydrogen.aero/press-releases/universal-hydrogen-magnix-plug-power-and-aerotec-announce-hydrogen-aviation-center-at-moses-lake-washington/ (visited on Jan. 7, 2024).

[60] VoltAero. "Cassio hybrid power module." (), [Online]. Available: https://www.voltaero.aero/en/propulsion/hybrid-power-module/ (visited on Jan. 7, 2024).

[61] VoltAero. "Cassio propulsion." (), [Online]. Available: https://www.voltaero.aero/en/propulsion/ (visited on Jan. 7, 2024).

[62] W. Tong, *Mechanical Design and Manufacturing of Electric Motors*, Second Edi. Taylor and Francis Ltd., ISBN: 9780367564285. DOI: 10.1201/9781003097716.

[63] Y. Gai, M. Kimiabeigi, Y. Chuan Chong, *et al.*, "Cooling of automotive traction motors: Schemes, examples, and computation methods," *IEEE Transactions on Industrial Electronics*, vol. 66, no. 3, pp. 1681–1692, Mar. 2019, ISSN: 02780046. DOI: 10.1109/TIE.2018.2835397.

[64] Y. Gai, Y. C. Chong, H. Adam, X. Deng, M. Popescu, and J. Goss, "Thermal Analysis of an Oil-Cooled Shaft for a 30 000 r/min Automotive Traction Motor," *IEEE Transactions on Industry Applications*, vol. 56, no. 6, pp. 6053–6061, Nov. 2020, ISSN: 19399367. DOI: 10.1109/TIA.2020.3025745.

[65] T. Harris and M. Kotzalas, *Rolling Bearing Analysis Essential Concepts of Bearing Technology*. Taylor and Francis Ltd., 2006, ISBN: 9780849371837.

[66] T. Harris and M. Kotzalas, *Advanced Concepts of Bearing Technology*. Taylor and Francis Ltd., 2006, ISBN: 9780849371820.

[67] Y. Wang, J. Cao, Q. Tong, *et al.*, "Study on the Thermal Performance and Temperature Distribution of Ball Bearings in the Traction Motor of a High-Speed EMU," *Applied Sciences (Switzerland)*, vol. 10, 2020. DOI: 10.3390/app10124373.

[68] R. Wang, X. Fan, D. Li, and R. Qu, "Comparison of Two Hollow-Shaft Liquid Cooling Methods for High Speed Permanent Magnet Synchronous Machines," in *ECCE 2020 - IEEE Energy Conversion Congress and Exposition*, Institute of Electrical and Electronics Engineers Inc., Aug. 2020, pp. 3511–3517, ISBN: 9781728158266. DOI: 10.1109/ECCE44975.2020.9235871.

[69] "The SKF Model for Calculating the Frictional Moment," SKF, Tech. Rep.

[70] SKF Group, "Super Precision Contact Ball Bearings: High-Speed, B Design, Sealed as Standard," Tech. Rep., 2012.

[71] K. Yan, Y. Wang, Y. Zhu, J. Hong, and Q. Zhai, "Investigation on heat dissipation characteristic of ball bearing cage and inside cavity at ultra high rotation speed," *Tribology International*, vol. 93, pp. 470–481, Sep. 2015, ISSN: 0301679X. DOI: 10.1016/j.triboint.2015.09.030.

[72] A. La Rocca, Z. Xu, P. Arumugam, *et al.*, "Thermal management of a high speed permanent magnet machine for an aeroengine," in *Proceedings - 2016 22nd International Conference on Electrical Machines, ICEM 2016*, 2016, pp. 2732–2737, ISBN: 9781509025381. DOI: 10.1109/ICELMACH.2016.7732908.

[73] P. H. Connor, A. La Rocca, Z. Xu, *et al.*, "Air-cooling of a hollow high-speed permanent magnet rotor," in *2019 IEEE International Electric Machines and Drives Conference, IEMDC 2019*, 2019, pp. 1216–1221, ISBN: 9781538693490. DOI: 10.1109/IEMDC.2019.8785089.

[74] V. Josefsson, A. Carlsson, S. Nategh, and D. Ekholm, "An Experimental Investigation of Hybrid Cooling Solution for High Performance Traction Motor," in

*IECON Proceedings (Industrial Electronics Conference)*, IEEE, 2022, pp. 1–6, ISBN: 9781665480253. DOI: 10.1109/IECON49645.2022.9968946.

[75] X. Yi, R. Sanchez, K. Haran, J. Veres, A. T. Perry, and P. J. Ansell, "Self-Pumped Air-Cooling Design for a High-Speed High-Specific-Power Motor," in *2018 IEEE Transportation and Electrification Conference and Expo, ITEC 2018*, Institute of Electrical and Electronics Engineers Inc., Aug. 2018, pp. 1135–1140, ISBN: 9781538630488. DOI: 10.1109/ITEC.2018.8450114.

[76] J. Dong, Y. Huang, L. Jin, and H. Yang, "Thermal optimization of a high-speed permanent magnet motor," *IEEE Transactions on Magnetics*, vol. 50, no. 2, pp. 749–752, Feb. 2014. DOI: 10.1109/TMAG.2013.2285017.

[77] C. Kim, K. S. Lee, and S. J. Yook, "Effect of air-gap fans on cooling of windings in a large-capacity, high-speed induction motor," *Applied Thermal Engineering*, vol. 100, pp. 658–667, 2016, ISSN: 13594311. DOI: 10.1016/j.applthermaleng.2016.02.077. [Online]. Available: http://dx.doi.org/10.1016/j.applthermaleng.2016.02.077.

[78] F. Boxberg, J. Saari, and P. Maki-Ontto, "Forced Air Cooling of a High-Speed Permanent Magnet Motor," *Proceedings - 2018 23rd International Conference on Electrical Machines, ICEM 2018*, pp. 1207–1212, 2018. DOI: 10.1109/ICELMACH.2018.8506723.

[79] G. Zhu, X. Liu, L. Li, H. Chen, W. Tong, and J. Zhu, "Cooling System Design of a High-Speed PMSM Based on a Coupled Fluidic-Thermal Model," *IEEE Transactions on Applied Superconductivity*, vol. 29, no. 2, pp. 1–5, 2019, ISSN: 15582515. DOI: 10.1109/TASC.2019.2892305.

[80] Z. Huang, J. Fang, X. Liu, and B. Han, "Loss Calculation and Thermal Analysis of Rotors Supported by Active Magnetic Bearings for High-Speed Permanent-Magnet Electrical Machines," *IEEE Transactions on Industrial Electronics*, vol. 63, no. 4, pp. 2027–2035, Apr. 2016, ISSN: 02780046. DOI: 10.1109/TIE.2015.2500188.

[81] K. R. Anderson, J. Lin, and A. Wong, "Experimental and numerical study of windage losses in the narrow gap region of a high-speed electric motor," *Fluids*, vol. 3, no. 1, Mar. 2018, ISSN: 23115521. DOI: 10.3390/fluids3010022.

[82] F. McCluskey, Y. Saadon, Z. Yao, and A. Camacho, "Cooling for electric aircraft motors," in *2019 18th IEEE Intersociety Conference on Thermal and Thermomechanical Phenomena in Electronic Systems (ITherm)*, 2019. DOI: 10.1109/ecce44975.2020.9235871.

[83] D. C. Ludois and I. Brown, "Brushless and permanent magnet free wound field synchronous motors for EV traction," Tech. Rep., 2017.

[84] J. Doerr, T. Attensperger, L. Wittmann, and T. Enzinger, "The New Electric Axle Drives from Audi," *MTZ Worldwide*, vol. 79, no. 6, pp. 18–25, 2018. DOI: 10.1007/s38313-018-0042-4.

[85] K. H. Lee, H. R. Cha, and Y. B. Kim, "Development of an interior permanent magnet motor through rotor cooling for electric vehicles," *Applied Thermal Engineering*, vol. 95, pp. 348–356, Feb. 2016, ISSN: 13594311. DOI: 10.1016/j.applthermaleng.2015.11.022.

[86] Y. Gai, M. Kimiabeigi, Y. C. Chong, *et al.*, "Pressure Loss Modelling in a Water-Cooled Hollow-Shaft Rotor for an Automotive Traction Motor," in

*Proceedings - 2018 23rd International Conference on Electrical Machines, ICEM 2018*, Institute of Electrical and Electronics Engineers Inc., Aug. 2018, pp. 1297–1302, ISBN: 9781538624777. DOI: 10.1109/ICELMACH.2018.8506852.

[87] Y. Gai, J. D. Widmer, A. Steven, *et al.*, "Numerical and Experimental Calculation of CHTC in an Oil-Based Shaft Cooling System for a High-Speed High-Power PMSM," *IEEE Transactions on Industrial Electronics*, vol. 67, no. 6, pp. 4371–4380, Jun. 2020, ISSN: 15579948. DOI: 10.1109/TIE.2019.2922938.

[88] G. Wang, Q. Qin, P. Wang, and X. Wang, "Analysis of the Rotor Loss in a High Speed Permanent Magnet Motor for Flywheel Energy Storage System," in *2015 18th International Conference on Electrical Machines and Systems, ICEMS 2015*, Institute of Electrical and Electronics Engineers Inc., Jan. 2016, pp. 2040–2044, ISBN: 9781479988044. DOI: 10.1109/ICEMS.2015.7385376.

[89] G. Bourhis, R. Sindjui, A. Gilson, and G. Zito, "Experimental Separation of No-Load Losses of an Electric Motor with Direct Oil Cooling," in *2022 International Conference on Electrical Machines, ICEM 2022*, Institute of Electrical and Electronics Engineers Inc., 2022, pp. 1341–1347, ISBN: 9781665414326. DOI: 10.1109/ICEM51905.2022.9910757.

[90] A. M. El-Refaie, J. P. Alexander, S. Galioto, *et al.*, "Advanced high-power-density interior permanent magnet motor for traction applications," *IEEE Transactions on Industry Applications*, vol. 50, no. 5, pp. 3235–3248, 2014, ISSN: 00939994. DOI: 10.1109/TIA.2014.2305804.

[91] B. Assaad, K. Mikati, T. V. Tran, and E. Negre, "Experimental Study of Oil Cooled Induction Motor for Hybrid and Electric Vehicles," in *Proceedings*

- *2018 23rd International Conference on Electrical Machines, ICEM 2018*, Institute of Electrical and Electronics Engineers Inc., Aug. 2018, pp. 1195–1200, ISBN: 9781538624777. DOI: 10.1109/ICELMACH.2018.8507058.

[92] M. H. Park and S. C. Kim, "Thermal characteristics and effects of oil spray cooling on in-wheel motors in electric vehicles," *Applied Thermal Engineering*, vol. 152, pp. 582–593, Apr. 2019, ISSN: 13594311. DOI: 10.1016/j.applthermaleng.2019.02.119.

[93] D. H. Lim and S. C. Kim, "Thermal performance of oil spray cooling system for in-wheel motor in electric vehicles," *Applied Thermal Engineering*, vol. 63, no. 2, pp. 577–587, Feb. 2014, ISSN: 13594311. DOI: 10.1016/j.applthermaleng.2013.11.057.

[94] A. Saleem, M. Hyeon Park, T. Ambreen, and S. Chul Kim, "Optimization of oil flow distribution inside the in-wheel motor assembly of electric vehicles for improved thermal performance," *Applied Thermal Engineering*, vol. 201, Jan. 2022, ISSN: 13594311. DOI: 10.1016/j.applthermaleng.2021.117753.

[95] K. Sim, Y. B. Lee, S. M. Jang, and T. H. Kim, "Thermal analysis of high-speed permanent magnet motor with cooling flows supported on gas foil bearings: part I - coupled thermal and loss modeling," *Journal of Mechanical Science and Technology*, vol. 29, no. 12, pp. 5469–5476, Dec. 2015, ISSN: 1738494X. DOI: 10.1007/s12206-015-1148-0.

[96] M. Jaeger, A. Ruf, K. Hameyer, and T. G. V. Tongeln, "Thermal Analysis of an Electrical Traction Motor with an Air Cooled Rotor," in *2018 IEEE Transportation and Electrification Conference and Expo, ITEC 2018*, Institute

of Electrical and Electronics Engineers Inc., Aug. 2018, pp. 194–200, ISBN: 9781538630488. DOI: 10.1109/ITEC.2018.8450239.

[97] S. Mizuno, S. Noda, M. Matsushita, T. Koyama, and S. Shiraishi, "Development of a totally enclosed fan-cooled traction motor," *IEEE Transactions on Industry Applications*, vol. 49, no. 4, pp. 1508–1514, 2013, ISSN: 00939994. DOI: 10.1109/TIA.2013.2256872.

[98] P. O. Gronwald and T. A. Kern, "Traction Motor Cooling Systems: A Literature Review and Comparative Study," *IEEE Transactions on Transportation Electrification*, vol. 7, no. 4, pp. 2892–2913, Dec. 2021, ISSN: 23327782. DOI: 10.1109/TTE.2021.3075844.

[99] Gai, Yaohui and Chong, Yew Chuan and Adam, Husain and Goss, James and Popescu, Mircea, "Cooling for Electric Aircraft Motors," in *22nd International Conference on Electrical Machines and Systems (ICEMS)*, 2019, pp. 1134–1138.

[100] Y. Gai, M. Kimiabeigi, Y. C. Chong, *et al.*, "On the Measurement and Modeling of the Heat Transfer Coefficient of a Hollow-Shaft Rotary Cooling System for a Traction Motor," *IEEE Transactions on Industry Applications*, vol. 54, no. 6, pp. 5978–5987, Nov. 2018, ISSN: 00939994. DOI: 10.1109/TIA.2018.2860558.

[101] P. S. Ghahfarokhi, A. Podgornovs, A. Kallaste, *et al.*, "Opportunities and Challenges of Utilizing Additive Manufacturing Approaches in Thermal Management of Electrical Machines," *IEEE Access*, vol. 9, pp. 36 368–36 381, 2021, ISSN: 21693536. DOI: 10.1109/ACCESS.2021.3062618.

[102] H. Wang, X. Liu, M. Kang, L. Guo, and X. Li, "Oil Injection Cooling Design for the IPMSM Applied in Electric Vehicles," *IEEE Transactions on*

*Transportation Electrification*, vol. 8, no. 3, pp. 3427–3440, Sep. 2022, ISSN: 23327782. DOI: 10.1109/TTE.2022.3161064.

[103] M. Popescu, D. A. Staton, A. Boglietti, A. Cavagnino, D. Hawkins, and J. Goss, "Modern Heat Extraction Systems for Power Traction Machines - A Review," *IEEE Transactions on Industry Applications*, vol. 52, no. 3, pp. 2167–2175, May 2016, ISSN: 00939994. DOI: 10.1109/TIA.2016.2518132.

[104] S. I. P. Pinel, H. R. Signer, and E. V. Zaretsky, "Comparison Between Oil-Mist and Oil-Jet Lubrication of High-Speed, Small-Bore, Angular-Contact Ball Bearings," NASA, Tech. Rep., 2001. [Online]. Available: http://www.sti.nasa.gov.

[105] "Lubrication of Rolling Bearings Principles Lubrication methods Lubricant Selection and Testing Storage and Handling," Schaeffler Technologies, Tech. Rep.

[106] K.-Y. Li, W.-J. Luo, and S.-J. Wei, "Machining accuracy enhancement of a machine tool by a cooling channel design for a built-in spindle," *Applied Sciences*, vol. 10, no. 11, 2020. DOI: 10.3390/app10113991.

[107] P. Gloeckner, K. Dullenkopf, and M. Flouros, "Direct outer ring cooling of a high speed jet engine mainshaft ball bearing: Experimental investigation results," vol. 133, 2011. DOI: 10.1115/gt2010-23312.

[108] M. Flouros, M. Hirschmann, F. Cottier, P. Gloeckner, and K. Dullenkopf, "Active outer ring cooling of high-loaded and high-speed ball bearings," vol. 135, no. 8, 2013. DOI: 10.1115/1.4024257.

[109] W. Wu, C. Hu, J. Hu, S. Yuan, and R. Zhang, "Jet cooling characteristics for ball bearings using the VOF multiphase model," *International Journal of Thermal Sciences*, vol. 116, pp. 150–158, Jun. 2017, ISSN: 12900729. DOI: 10.1016/j.ijthermalsci.2017.02.014.

[110] J. Liu, H. Ni, Z. Xu, and G. Pan, "A simulation analysis for lubricating characteristics of an oil-jet lubricated ball bearing," *Simulation Modelling Practice and Theory*, vol. 113, Dec. 2021, ISSN: 1569190X. DOI: 10.1016/j.simpat.2021.102371.

[111] J. Hu, W. Wu, M. Wu, and S. Yuan, "Numerical investigation of the air-oil two-phase flow inside an oil-jet lubricated ball bearing," *International Journal of Heat and Mass Transfer*, vol. 68, pp. 85–93, 2014, ISSN: 00179310. DOI: 10.1016/j.ijheatmasstransfer.2013.09.013.

[112] W. Wu, C. Hu, J. Hu, and S. Yuan, "Jet cooling for rolling bearings: Flow visualization and temperature distribution," *Applied Thermal Engineering*, vol. 105, pp. 217–224, Jul. 2016, ISSN: 13594311. DOI: 10.1016/j.applthermaleng.2016.05.147.

[113] B. Yan, L. Dong, K. Yan, F. Chen, Y. Zhu, and D. Wang, "Effects of oil-air lubrication methods on the internal fluid flow and heat dissipation of high-speed ball bearings," *Mechanical Systems and Signal Processing*, vol. 151, Apr. 2021, ISSN: 10961216. DOI: 10.1016/j.ymssp.2020.107409.

[114] L. Jiang, Y. Lyu, P. Zhu, and Z. Liu, "Numerical investigation of the oil–air distribution inside ball bearings with under-race lubrication," in *Proceedings*

*of the Institution of Mechanical Engineers, Part J: Journal of Engineering Tribology*, vol. 236, 2021, pp. 499–513. DOI: 10.1177/13506501211010556.

[115] H. Bao, X. Hou, X. Tang, and F. Lu, "Analysis of temperature field and convection heat transfer of oil-air two-phase flow for ball bearing with under-race lubrication," vol. 73, no. 5, pp. 817–821, 2021. DOI: 10.1108/ILT-03-2021-0067.

[116] A. Manikandan, M. Abdalmagid, G. Pietrini, M. Goykhman, and A. Emadi, "Structural Design Evaluation of Integrated Rotor Hub and Shaft for a High-Speed Surface Mounted Radial Flux Permanent Magnet Synchronous Motor," *2023 IEEE Transportation Electrification Conference and Expo, ITEC 2023*, pp. 1–6, 2023. DOI: 10.1109/ITEC55900.2023.10186954.

[117] S. Li, Y. Li, W. Choi, and B. Sarlioglu, "High-Speed Electric Machines: Challenges and Design Considerations," *IEEE Transactions on Transportation Electrification*, vol. 2, no. 1, pp. 2–13, Mar. 2016, ISSN: 23327782. DOI: 10.1109/TTE.2016.2523879.

[118] A. Borisavljevic, H. Polinder, and J. A. Ferreira, "On the speed limits of permanent-magnet machines," *IEEE Transactions on Industrial Electronics*, vol. 57, no. 1, pp. 220–227, Jan. 2010, ISSN: 02780046. DOI: 10.1109/TIE.2009.2030762.

[119] G. Genta, *Dynamics of Rotating Systems*, ISBN: 0-387-20936-0.

[120] A. Borisavljevic, H. Polinder, and J. A. Ferreira, "On the speed limits of permanent-magnet machines," *IEEE Transactions on Industrial Electronics*,

vol. 57, no. 1, pp. 220–227, Jan. 2010, ISSN: 02780046. DOI: 10.1109/TIE.2009.2030762.

[121] J. D. Ede, Z. Q. Zhu, and D. Howe, "Rotor resonances of high-speed permanent-magnet brushless machines," *IEEE Transactions on Industry Applications*, vol. 38, no. 6, pp. 1542–1548, Nov. 2002, ISSN: 00939994. DOI: 10.1109/TIA.2002.804765.

[122] A. Tenconi, S. Vaschetto, and A. Vigliani, "Electrical machines for high-speed applications: Design considerations and tradeoffs," *IEEE Transactions on Industrial Electronics*, vol. 61, no. 6, pp. 3022–3029, 2014, ISSN: 02780046. DOI: 10.1109/TIE.2013.2276769.

[123] L. Dahnoun, T. Marcand, R. Rahouadj, *et al.*, "Comparison of Methods for Evaluating Mechanical Stress in the Rotor of High-Speed Machines," in *2022 International Conference on Electrical Machines, ICEM 2022*, Institute of Electrical and Electronics Engineers Inc., 2022, pp. 752–759, ISBN: 9781665414326. DOI: 10.1109/ICEM51905.2022.9910837.

[124] Y. Lin, Y. Huang, and T. Zhang, "Comprehensive Design and Analysis of Rotor Stress for HSPMM Considering Cooling Method," *Machines*, vol. 10, no. 6, Jun. 2022, ISSN: 20751702. DOI: 10.3390/machines10060475.

[125] W. Li, H. Qiu, X. Zhang, J. Cao, and R. Yi, "Comprehensive Design and Analysis of Rotor Stress for HSPMM Considering Cooling Method," *IEEE Transactions on Industrial Electronics*, vol. 61, no. 6, 2014. DOI: 10.1109/tie.2013.2251740.

[126] EOS GmbH, *EOS Aluminium AlSi10Mg Material Data Sheet EOS*, 2022.

[127] "XE 663 + DK 50/11 Potting Epoxy Technical Datasheet," Demak l.o.o., Apr. 2022.

[128] D. S.r.l, *Process for over-moulding an outer stator*, Worldwide Patent WO2017199075A1, Nov. 2017. [Online]. Available: https://patents.google.com/patent/WO2017199075A1/en?oq=wo+2017%2f199075+a1.

[129] R. Wang, X. Fan, D. Li, R. Qu, Z. Liu, and L. Li, "Comparison of Heat Transfer Characteristics of the Hollow-Shaft Oil Cooling System for High-Speed Permanent Magnet Synchronous Machines," *IEEE Transactions on Industry Applications*, vol. 58, no. 5, pp. 6081–6092, 2022. DOI: 10.1109/TIA.2022.3182312.

[130] "Turcon Varilip PDR Catalog," Trelleborg Group. [Online]. Available: https://www.trelleborg.com/-/media/tss-media-repository/tss_website/pdf-and-other-literature/catalogs/turcon_varilip_pdr_gb_en.pdf (visited on Jan. 18, 2024).

[131] T. Akiyama, T. Honda, and Y. Nakanishi, "Friction welding of lightweight motor shafts for electric vehicles," in *2016 IEEE International Conference on Renewable Energy Research and Applications, ICRERA 2016*, IEEE, 2016, pp. 259–264. DOI: 10.1109/ICRERA.2016.7884548.

[132] SKF Group. "Tolerances for bearing seats and abutments." (), [Online]. Available: https://www.skf.com/ca/en/products/rolling-bearings/principles-of-rolling-bearing-selection/bearing-selection-process/bearing-interfaces/tolerances-for-bearing-seats-and-abutments (visited on Jan. 16, 2024).

[133] J. Smith and J. Doe, *Example user guide*, 3rd, Available at https://example.com/manual.pdf, Example Corporation, Example City, CA, Jun. 2023.

[134] A. Inc., *Ansys cfx-solver theory guide*, 2023R1, ANSYS Inc., Canonsburg, PA, Jan. 2023.

[135] P. Shams Ghahfarokhi, A. Podgornovs, A. Kallaste, A. J. Marques Cardoso, A. Belahcen, and T. Vaimann, "The Oil Spray Cooling System of Automotive Traction Motors: The State of the Art," *IEEE Transactions on Transportation Electrification*, vol. 9, no. 1, pp. 428–451, Mar. 2023, ISSN: 23327782. DOI: 10.1109/TTE.2022.3189596.